

UNIVERSITÀ DEGLI STUDI DI PADOVA

DEPARTMENT OF CHEMICAL SCIENCES

JUSTUS-LIEBIG UNIVERSITÄT GIESSEN

CENTER FOR MATERIALS RESEARCH

MASTER OF SCIENCE IN MATERIALS SCIENCE

**IMPACT OF GE-DOPING ON THE PHOTOELECTROCHEMICAL
RESPONSE OF CUBIC (GA,IN)N PHOTOELECTRODES**

MASTER THESIS

Supervisors:

Prof. Dr. Sangam Chatterjee

Justus-Liebig Universität Giessen

Prof. Dr. Matthias T. Elm

Justus-Liebig Universität Giessen

Student:

Sundas Hamid

Prof. Chiara Maurizio

Università degli Studi di Padova

ACADEMIC YEAR 2025-2026

Contents

Chapter 0: Abstract	4
Abbreviations	5
CHAPTER 1: Introduction	6
1.1 Background and Motivation	6
Global Warming and Climate Change	6
Renewable and clean energy sources	7
Hydrogen as Green alternative fuel	8
Photocatalysis for clean hydrogen production	9
1.2 Principles of Photoelectrochemical (PEC) Water Splitting	10
Concept of PEC cells	10
1.3 Roles of Semiconductors	10
Cubic III- nitrides	12
Limitations of cubic III-nitrides	13
1.4 Thesis Project	14
Chapter:2 Material and Characterization Techniques	15
2.2 The Electrochemical Cell	15
2.3 Zahner Thales setup	16
The counter electrode (CE)	16
The placement of working electrode (WE)	17
The reference electrode (RE)	17
2.4 Physicochemical Characterization:	19
Material synthesis	19
Molecular Beam Epitaxy:	19
Sample Structure	20
2.5 Secondary Mass Ion Spectrometry (SIMS)	21
2.6 Scanning electron Microscopy (SEM) and Energy Dispersive X-ray Spectroscopy (EDX)	23
Electrochemical Characterization	25
2.7 Open circuit potential (OCP):	25
2.8 Chopped Light Voltammetry (CLV)	26
2.9 Cyclic voltammetry in PEC	26
2.10 Electrochemical Impedance Spectroscopy:	27
The Impedance of electric circuit	30
Semiconductor electrolyte Interface	34
Chapter 3: Results and Discussion	37

3.1 Electrolyte and reaction mechanism	37
3.2 Chopped Light Voltammetry.....	39
3.3 SIMS comparison of samples after analysis in different electrolytes.....	41
Ge-doped InGaN grown at 850 °C.....	41
(In,Ga)N	42
3.4 SIMS Investigation of Ge incorporation into the different InGaN thin films InGaN	42
3.5 Electrochemical Characterization	46
3.5.1 Open Circuit Potential (OCP).....	46
3.5.2 Cyclic Voltammetry (CV)	48
3.5.3 Electrochemical Impedance Spectroscopy (EIS)	54
(In,Ga)N film.....	54
Ge doped (In,Ga)N film grown at 850 °C	61
Ge doped (In,Ga)N film grown at 950 °C	66
Ge doped (In,Ga)N film grown at 1000 °C	73
3.5.4 Comparative EIS and Mott-Schottky Analysis of Undoped and Ge-doped InGaN.....	78
Mott-Schottky Analysis comparison:	79
Mechanistic Interpretation	80
Conclusion.....	82
Future Perspective	84
References	85

Chapter 0: Abstract

This thesis project, conducted at Justus Liebig University Giessen (JLU) in Germany, focuses on photoelectrochemical (PEC) water splitting using (Ga,In)N electrode materials. The primary objective of this study is to investigate the influence of germanium (Ge) doping on the photoelectrochemical response of cubic (Ga,In)N photoanodes synthesized via molecular beam epitaxy (MBE).

The interfacial processes occurring at the electrode-electrolyte interface during PEC water splitting in an alkaline environment are systematically evaluated using a three-electrode configuration for electrochemical characterization. The experimental methodology uses several electrochemical techniques, including open circuit potential (OCP), cyclic voltammetry (CV), and electrochemical impedance spectroscopy (EIS) to study charge carrier transport and the interface of semiconductor/electrolyte across a range of frequencies.

We use complementary physicochemical characterization techniques to examine surface morphology and compositional changes before and after PEC analysis. Overall, the methods used allowed for the full assessment of electrochemical performance and structural stability of the photoanodes. The goal was to understand the relationship between dopant activation, donor density, and how charge is transferred at the interface.

Depending on the growth temperature, the dopant activation and donor density has been investigated. The findings show that optimal electrochemical efficiency is achieved by equally activating dopants and controlling defects rather than maximizing donor density.

The experimental results presented provide useful information towards the possible development of this material for photoelectrochemical water splitting applications.

Abbreviations

PEC	Photoelectrochemical cells
VB	Valence band
CB	Conduction Band
MBE	Molecular Beam Epitaxy
OCP	Open Circuit Potential
CV	Cyclic Voltammetry
EIS	Electrochemical Impedance Spectroscopy
SIMS	Secondary Ion Mass Spectroscopy
SEM	Scanning Electron Microscopy
EDX	Energy Dispersive X-ray Spectroscopy
WE	Working electrode
CE	Counter electrode
RE	Reference electrode
CDC	Circuit Description code
CPE	Constant phase element
3EC	3 electrode configuration
PGSTAT	potentiostat/galvanostat

CHAPTER 1: Introduction

1.1 Background and Motivation

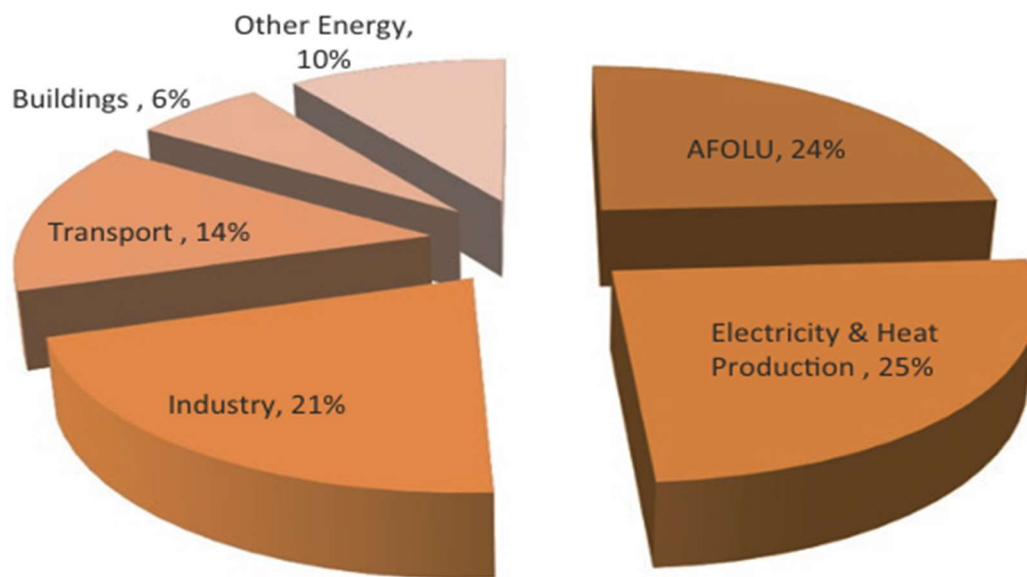
Global Warming and Climate Change

We are living in an era where energy consumption is increasing drastically day by day. Statistically, from 1800 to 2024, the global energy demand rises from 5000 TWh to 200,000 TWh¹. Still most of the energy supply comes from fossil fuels. The high energy demand is accompanied by the release of greenhouse gases resulting in the global warming. Global warming is alarming and the temperature of the globe is increasing. Fossil fuels are not only affecting the environment, but also limited and geographic (48% of proven reserves in Middle east BP statistical Review 2021). Now the world has turned their utmost attention towards sustainable fuels and energy because we can't limit our technologies.

Although climate change and global warming are two different phenomena, they are closely connected. Global warming is associated with the increase in the Earth's mean temperature. Climate change, in contrast, is a more extensive term encompassing variations in weather and wind patterns, precipitation, temperature shifts, and seasonal changes, but not including those of a natural origin. The biosphere is undergoing drastic changes due to global warming, affecting all levels of life, from complex organisms to microbodies.² Greenhouse gases are important in maintaining global temperature and the wellbeing of life on Earth. However, since the Industrial Revolution in 1750, humans have drastically increased the presence of greenhouse gases, particularly CO₂, in the environment. The activities involved include burning fossil fuels, cutting down trees, and soil degradation. From 1750 to 2019, we observed a 48% increase in carbon dioxide levels. In the same period, chlorofluorocarbons (CFCs), nitrous oxide (N₂O), and methane (CH₄) increased by 262%, 20%, and 157%, respectively. The rise in gas levels and the resulting rise in temperature have led to weather extremes, including the shrinkage of the Arctic Sea, the melting of glaciers, and the rise in sea level.

To stabilize the climate, we need to reduce the emission of the greenhouse gases and to find alternatives to fully shift to renewable energies, which seems not an easy task and unlikely in near future.³ Research has been going on to move towards sustainability, but at the moment it is still not very economical. The damage caused by human activities has reached such a scale

that stays a difficult task reaching sustainability and steadily increasing demand for energy day by day also impedes to use alternatives to fossil fuels. Thus, it is essential to conduct



further research and find ways to reconcile both life and energy consumption.

Fig 1: Anthropogenic emission of greenhouse gases by different sectors (AFOLU stands for Agriculture, Forestry, and other land use³).

Renewable and clean energy sources

Most of the energy needed for economic development is from fossil fuels such as coal, oil and natural gas. Coal, as the most important fuel drives the production of electricity while, oil and natural gas although not exclusively make up a large part of today's energy supply and cause damage to the environment in a similar pace. Despite their drastic effects on the environment, we must keep in mind that fossil fuels are rapidly turning out. Renewable energies are naturally replenishing, inexhaustible in duration but have some limitations in amount available per unit time. These energies are termed as an alternative energy with respect to fossil fuels. They are clean, sustainable and inexhaustible. It includes solar energy, geothermal, wind energy, tide waves etc.⁴ The advantage of renewable energy is that they produce no greenhouse gases, reduces air pollution and most important we will not run out of it. The main challenges to tackle are the high upfront costs, its storage capabilities, geographical limitations. The focus of my research is photoelectrochemical process where solar energy is used to split water to produce hydrogen. **Fig 2** shows the excitation of electrons from valence to conduction band using sunlight and thus the flow of charge to load the appliances.

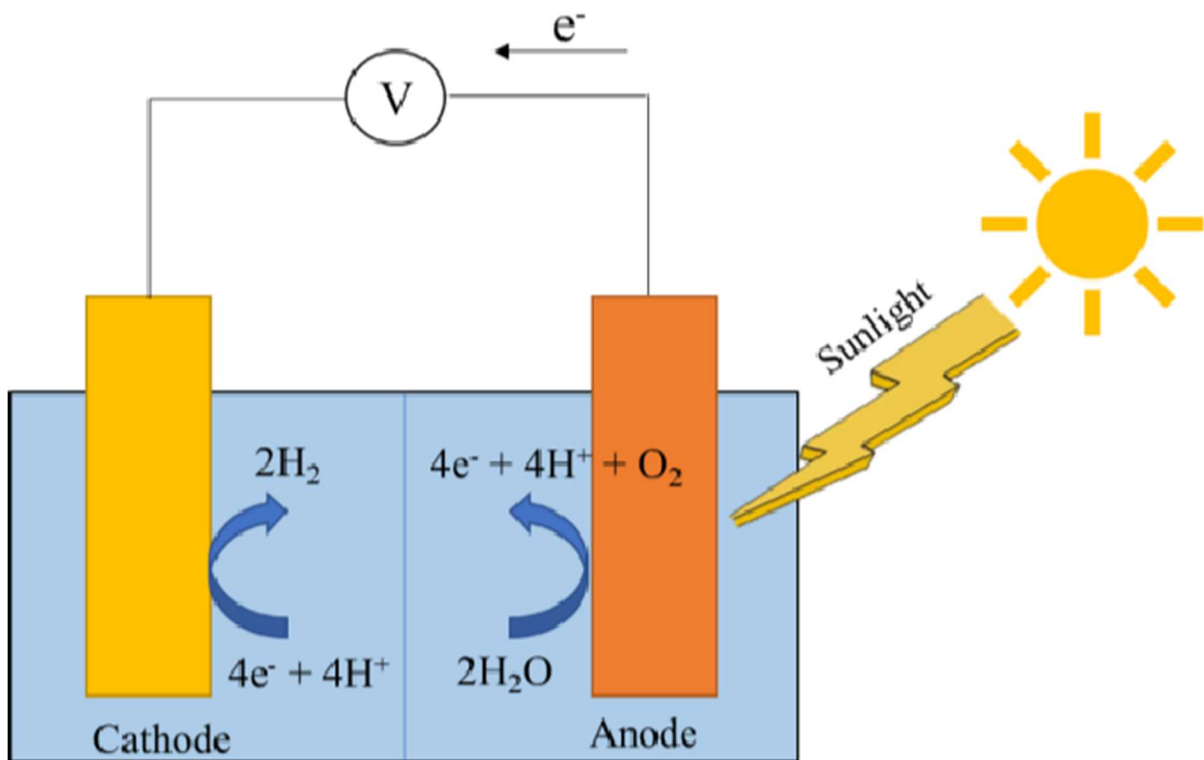


Fig 2: Schematic diagram of photoelectrochemical water splitting.⁵

Hydrogen as Green alternative fuel

Hydrogen is a very promising fuel for powering automobiles, as heating source for offices and homes or for fuelling jets⁶. It is used for running city buses and powering mining equipment, demonstrating its mobile applications. At the same time home generators and large energy generation systems show its stationary uses. It is a potential fuel with great advantages, but its practical applications require great measures in terms of distribution from suppliers to end users. Production, storage and transportation pose major challenges and require new concepts and technologies. Although, hydrogen is a sustainable and environment friendly fuel, it is often produced from fossil fuels.² The common method known as steam methane reforming of methane gas, is approximately 72% efficient but it produces byproducts including carbon monoxide and carbon dioxide. Thus, this method is not an effective option for sustainability and environment friendly hydrogen production. It has similar impacts as burning the natural gas directly⁷. Comparable processes include autothermal reforming of oil, the gasification of coal and other hydrocarbons, which also threatens the climate and, thus, are not sustainable.

Photoelectrochemical water splitting has the potential to be an efficient and environment friendly method for producing hydrogen with zero emissions. It uses free sunlight to split

water molecules into hydrogen and oxygen. However, large scale hydrogen production using this process is still under development and not commercially viable.⁶ In summary, 48% of world's hydrogen production is due to natural gas, 30% followed by coal, 4% is produced by electrolysis, an energy intensive procedure which requires ways to improve efficiency of electrolyzers. PEC isn't commercial yet because its system needs to achieve a 10% efficiency rate, a \$2–\$4 cost per kilogram of hydrogen, and a 10-year lifetime. Currently, PEC systems have a higher cost than competing technologies⁸.

Photocatalysis for clean hydrogen production

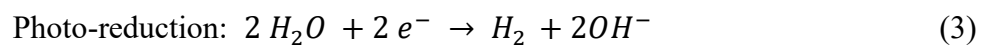
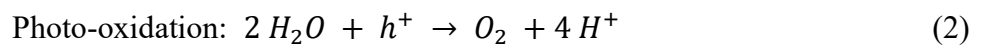
Photocatalysis is the process of converting solar energy, usually UV light or light at the upper end of the visible range into chemical energy. The energy of photons is related to the frequency, ν of radiation

$$E=h\nu \quad (1)$$

Where h is the Plank's constant

When a photon is struck by the photocatalyst (a semiconductor like TiO_2), an electron is excited from the valence band (VB) to the conduction band (CB), and an electron-hole pair is created. This paves the way for oxidation and reduction reactions⁷. The reaction of the holes with water molecules produces oxygen. Meanwhile, electrons react with water molecules to form hydroxyl ions and hydrogen molecules. Two processes are said to occur at the same time: the oxygen evolution reaction near the VB edge and the hydrogen evolution reaction near the CB edge.

Following are the reaction paths



Usually, semiconductors with a smaller bandgap than TiO_2 are used as photoelectrodes (photoanodes (n-type InGaN) and photocathodes (p-type InGaN)) to harvest more of the visible light. We investigate the electrochemical properties of n-type InGaN semiconductor for photocatalytic water splitting because its bandgap energy is comparable to the energy of UV light and light in the visible range.⁹ Our solar spectrum consists of only 4% of UV light while 48% of the visible spectrum reaching earth's surface. Thus, semiconductors with bandgap energy corresponding to visible light and InGaN show a good behaviour.⁹ Here, we

used UV light because we doped our sample with Ge and dopants increases the bandgap. The energy of the photons needs to be high enough to generate a voltage of at least 1.23eV in the electrochemical cell¹⁰.

1.2 Principles of Photoelectrochemical (PEC) Water Splitting

Concept of PEC cells

PEC cells are used to generate electron-hole pairs using photons.¹¹ The charge carriers take part in a chemical reaction to split water. PEC electrodes made of inorganic materials are more durable and more versatile compared to organic ones. However, there are challenges which needs to be countered like the lack of efficiency, and the fabrication of material is not trivial and cost efficient. Although the basic principle of photoelectrochemical water splitting seems to be simple, several aspects like type of electrolyte, photoelectrode but also their interaction with each other affect the efficiency at device scale¹².

1.3 Roles of Semiconductors

When a semiconductor with a certain band gap energy absorbs photons with higher energy, it will excite electrons from the valence bands to the conduction bands, which in a result generates electron-hole pair. These carriers will lead to the oxidation and reduction reactions if the reaction is thermodynamically favorable.¹³ To achieve self-driven photocatalytic water splitting, the semiconductor must align with the reduction and oxidation potential of water that is +0 and +1.23 V vs reversible hydrogen electrode at pH = 0. For other pH values, the potential is given by:

$$E_{\text{meas}} = E_{\text{ref}} + 0.0591 \times \text{pH} \quad (4)$$

where E is the potential and E_{ref} is the reference potential.

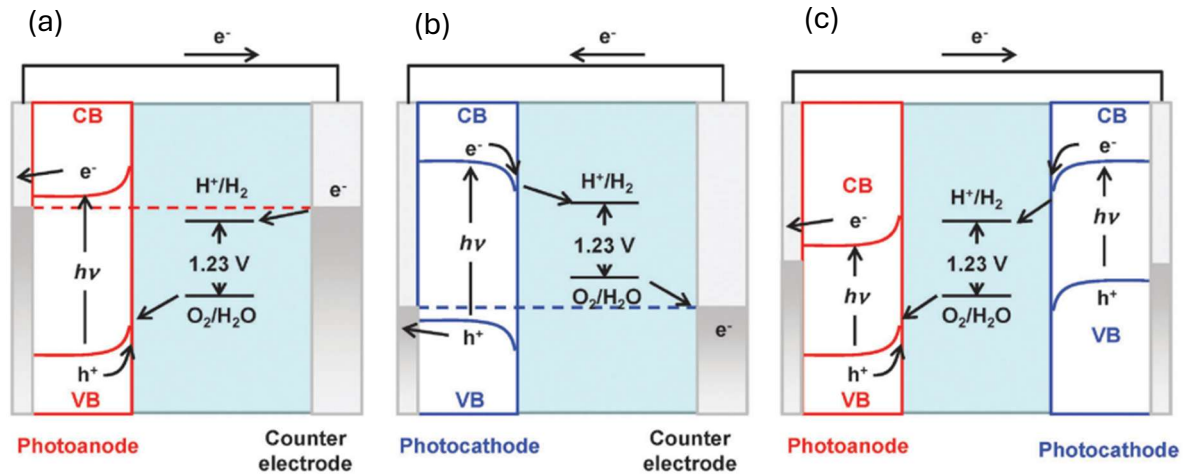


Fig 3: Schematic representation of PEC water splitting configurations: (a) photoanode, (b) photocathode, and (c) tandem cell. ¹⁴

Fig 3 (a) depicts a photoanode-based PEC system, where a semiconductor photoanode absorbs photons, generating electron-hole pairs. The holes migrate to the electrolyte interface to drive the oxygen evolution reaction, while electrons flow to the counter electrode where hydrogen evolution occurs.

Fig 3 (b) shows a PEC system using a p-type semiconductor for hydrogen and oxygen evolution.

Fig 3 (c) shows a tandem PEC cell that has a dual-photoelectrode configuration. Each photoelectrode independently absorbs photons, generating charge carriers that drive their respective half-reactions. The photoanode oxidizes water at its interface and the photocathode reduces protons. This configuration enables bias-free or reduced-bias water splitting by utilizing complementary material with maximal solar spectrum absorption and minimal external energy input requirements ¹³.

Nitrides of group III and their alloys show great applications in UV-light emitting diodes (LED), ultrafast transistors, and micro-LED's^{15,16}. The cubic $In_x Ga_{1-x}N$ alloy gains immense attention as its bandgap can be tuned throughout the whole solar spectrum. GaN crystallizes in the thermodynamically stable wurtzite phase and exhibits large polarization fields at interfaces¹⁷.

In contrast, the zincblende metastable phase of $In_x Ga_{1-x}N$ shows no such fields due to its cubic symmetry. The use of $In_x Ga_{1-x}N$ may bridge the green and amber gap.¹⁸ However, the heteroepitaxial growth of c-III nitrides faces different challenges, it has a very narrow

window of growth parameters. Suitable substrates with matching lattice parameters and with high crystal quality are needed to avoid structural defects in $c\text{-In}_x\text{Ga}_{1-x}\text{N}$.

Cubic III- nitrides

Group III- nitrides such as GaN, InN, AlN and their alloys are pivotal semiconductor materials for photochemical and opto-electronic applications. We will discuss the crystal structures of both, hexagonal wurtzite and cubic zincblende with their advantages and limitations for device applications¹⁹. The hexagonal wurtzite is thermodynamically stable and can be grown with a high crystal quality²⁰. For example h-(Al)GaN show better performance in high break-down fields, higher efficiency and higher switching frequency compared to conventional Si-based devices, and are thus be used for high power applications like batteries, charging in automobiles and mobile devices. Table 1 gives detailed information regarding bandgap, lattice parameters and spontaneous polarization of III-nitrides.

III-N	h-AlN	c- AlN	h- GaN	c- GaN	h-InN	c-InN
E_{gap} [eV]	6.25	5.4	3.51	3.299 3.295	0.78	0.61 0.62
a [Å°]	3.112	4.373	3.189	4.51 4.505	3.545	5.01
c [Å°]	4.982	-	5.185	-	5.703	-
Spontaneous polarization [C/m ²]	-0.090	-	-0.034	-	-0.042	-

Table 1: Properties of hexagonal and cubic III-nitrides²¹.

As shown in Table 1, the bandgap energies of h-GaN and h-InN range from the near-UV to the near-IR. Thus, varying the composition of (In,Ga)N alloys enable the development of LEDs across the entire visible spectrum. However, the radiant recombination rate of these devices experiences a rapid decline with increasing In content, leading to a reduction in efficiency for high current densities. This phenomenon is referred to as "efficiency droop". A droop begins due to the internal polarization fields of hexagonal wurtzite structures, which separate electrons from holes. This decreases the wave function overlap, leading to a decrease in radiative recombination¹⁶.

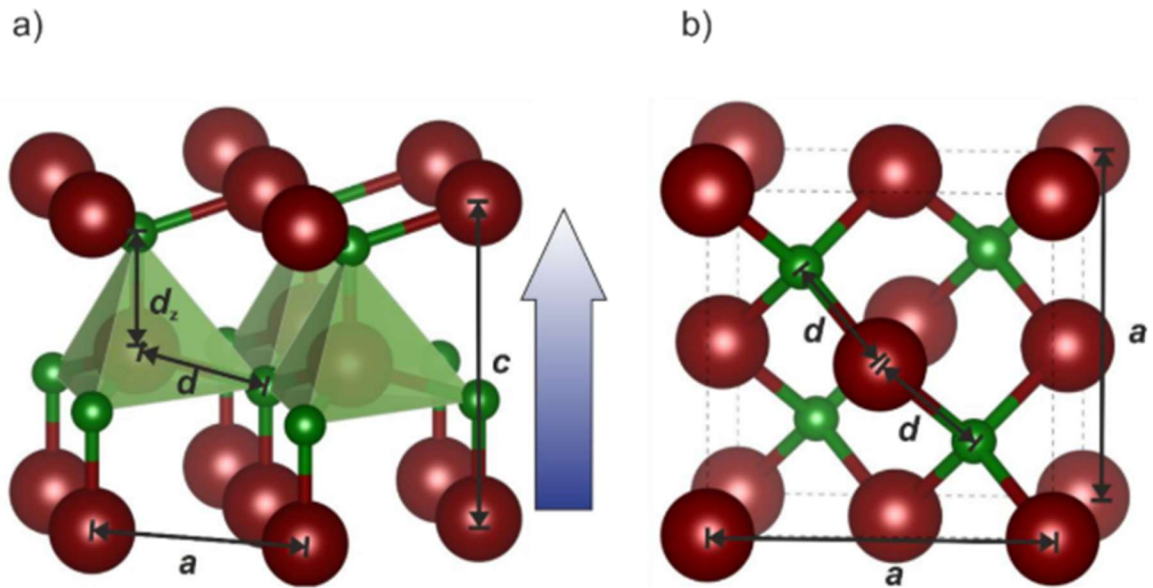


Fig 4: Crystal structures of group III-nitrides, a) ball and stick model of a III nitrides wurtzite structure where small green (group III) and red balls shows (nitrogen) showing internal polarization fields. b) Ball-stick model of zincblende III-nitrides shows no internal fields due to its cubic structure.²²

Fig 4 (a) shows the thermodynamically stable hexagonal structure of III nitrides, while Fig 4 (b) shows the cubic structure with a higher level of symmetry. Here all bonds are symmetric, and their length d are equal. Thus, no internal polarization arises at interfaces and no separation of electrons and holes occur. Therefore, cubic III-nitrides are of high interest for optoelectronic technologies²².

Limitations of cubic III-nitrides

The structural benefits of cubic III-nitrides make them a promising material system for various applications. However, the epitaxial growth of cubic nitrides is challenging. Major drawbacks are its narrow window of growth parameters and limited substrates options. The research on cubic nitrides started in the nineties but slowed down after the successful growth of hexagonal nitrides²³.

1.4 Thesis Project

This thesis project, conducted at Justus Liebig University Giessen (JLU) in Germany, focuses on photoelectrochemical (PEC) water splitting using (Ga,In)N electrode materials. The primary objective of this study is to investigate the influence of germanium (Ge) doping on the photoelectrochemical response of cubic (Ga,In)N photoanodes synthesized via molecular beam epitaxy (MBE).

The interfacial processes occurring at the electrode-electrolyte interface during PEC water splitting in an alkaline environment are systematically evaluated using a three-electrode configuration (3EC) for electrochemical characterization.

The experimental methodology uses several electrochemical techniques, including open circuit potential (OCP), cyclic voltammetry (CV), and electrochemical impedance spectroscopy (EIS) to study charge carrier transport and the interface of semiconductor/electrolyte across a range of frequencies.

We use complementary physicochemical characterization techniques to examine surface morphology and compositional changes before and after PEC analysis. These include Secondary Ion Mass Spectrometry (SIMS) for depth-resolved elemental profiling, Energy-dispersive X-ray Spectroscopy (EDX) for compositional analysis, and Scanning Electron Microscopy (SEM) for surface morphological characterization. The methods allow for the full assessment of electrochemical performance and structural stability of the photoanodes.

Chapter:2 Material and Characterization Techniques

2.2 The Electrochemical Cell

The widely used electrochemical setup is a three-electrode configuration consisting of a working electrode (WE), a reference electrode (RE), and a counter electrode (CE), all connected to a potentiostat. The working electrode has the catalytically active surface that facilitates the desired redox reactions. These reactions occur under a specific voltage or potential difference relative to the stable reference electrode²⁴. The potential of the reference electrode is stable if no current flows through it. The potentiostat measures the difference between the working and reference electrodes and corrects any deviation from the set value by circulating a current between the working and counter electrodes. The counter electrode's surface is typically larger than the working electrode's surface. The appropriate current-carrying (WE, CE) or voltage-measuring (RE) leads (terminals) are used to connect each of these electrodes to the potentiostat. In a three-electrode configuration (see Figure 11A), the voltage is applied between the working and reference electrodes. In this configuration, beneath a slight voltage fluctuation, the impedance due to the flow of current is attributable to (i) the ohmic resistance of the electrolyte between the reference and the working electrode, which is denoted as uncompensated resistance (R_u).

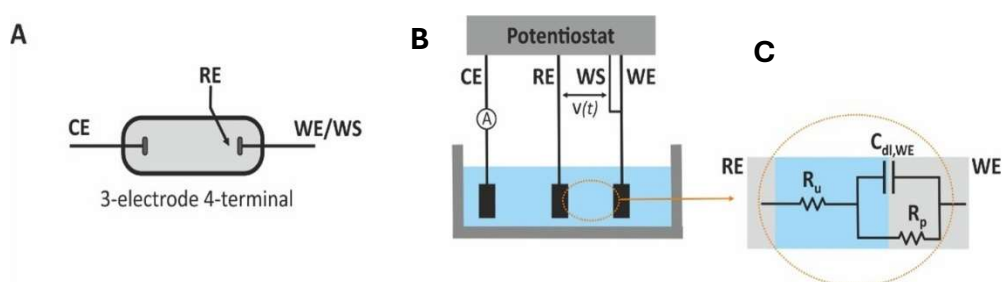


Fig 5: (A) Electrochemical system with 3-electrode 4-terminal, (B) connection modes with the working electrode (WE), working sense (WS), counter electrode (CE), and reference electrode (RE) and (C) equivalent circuit²⁵.

For a specified electrolyte, the resistance of the solution (R_u) is determined by the separation between the reference and the working electrodes²⁶. The ohmic resistance also includes the connection cables resistances and the working electrode, but in most of the cases these contributions can be neglected. Due to electric double layer at the electrode/electrolyte interface behaves as a capacitor denoted as C_{dl} . Figure 5 (c) shows the equivalent electrical

circuit of the cell at an enlarged scale. If the WE is an ideally polarizable electrode, the charge transfer between the electrode and the electrolyte is impossible or very slow. Therefore, the polarization resistance is infinite. So, in this case, all the current goes through R_u and C_{dl} , and we can simulate the cell's impedance in an electrical circuit where R_u and C_{dl} are connected in series²⁷.

A Zahner workstation was used to measure the electrochemical impedance in a three-electrode system configuration. It is an excellent tool for characterizing the dynamic processes that take place in a PEC cell. PEC water splitting consists of a series of electrochemical and physical processes, such as light absorption, the generation and separation of charges, charge transport, surface reaction kinetics, and charge recombination.²⁸ All of these components play a key role in the overall efficiency of photoelectrochemical redox reactions. Electrochemical impedance spectroscopy (EIS) allows us to understand the complex reactions of a photoelectrode with and without illumination through the frequency-dependent electrical response. Compared to conventional CV and other measurements, it provides deeper knowledge of photoelectrochemical reactions²⁹.

2.3 Zahner Thales setup

The counter electrode (CE)

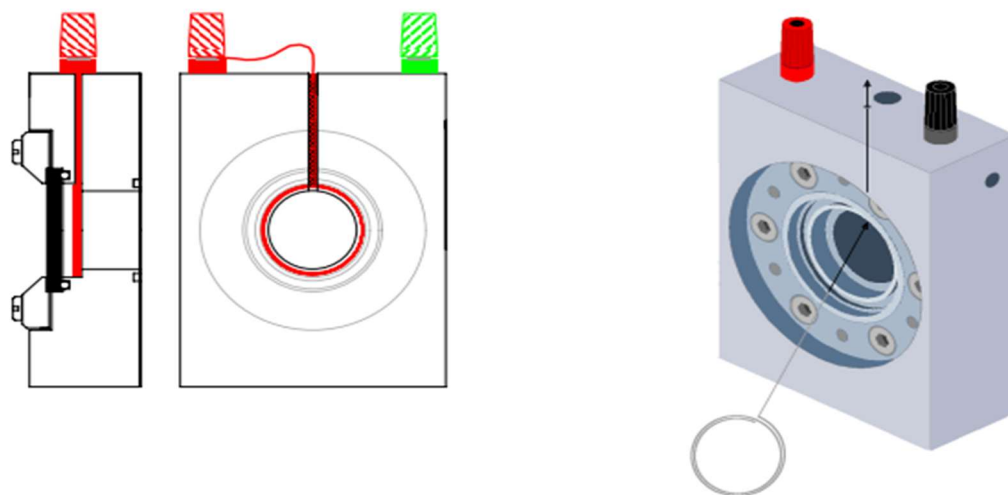


Fig 6: Schematic depiction of the counter electrode (red Part) in the electrochemical cell (Zahner Manual).

The counter electrode (CE) located behind an optical window. A 2 mm hole is a platinum wire drilled through the top of the cell, which is connected to the setup through the red connector.

The placement of working electrode (WE)

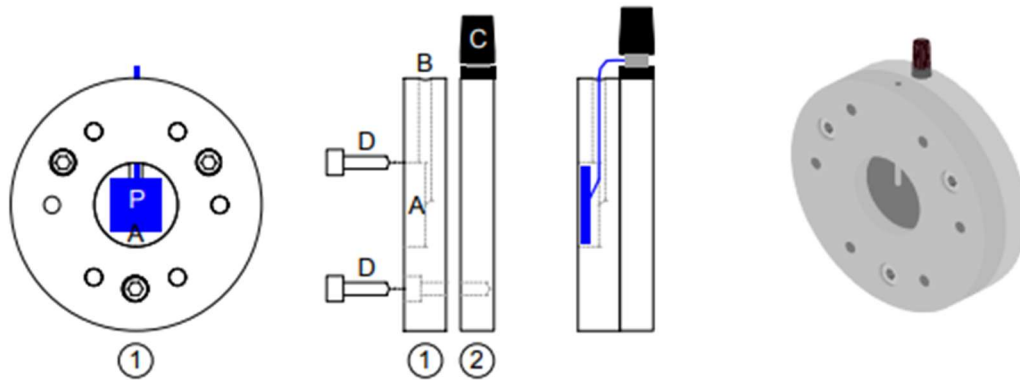


Fig 7: The blue area shows the placement of the specimen/substrate which acts as working electrode (Zahner Manual).

Figure 7 shows an insulating specimen holder and a conducting plate for working electrode. The specimen is placed in the middle of the holder, which is connected to the potentiostat via black binding wires. The working electrode is mounted on the back of the cell using an O-ring of 6mm and six screws.

The reference electrode (RE)

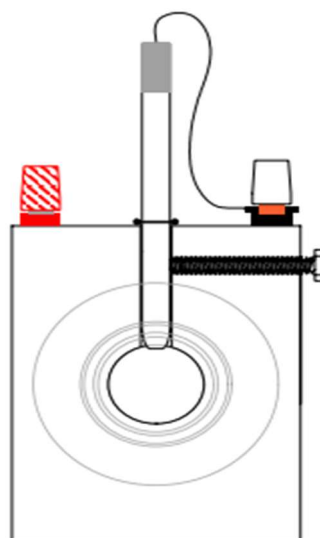


Fig 8: Ag/AgCl reference electrode mounted in the centre of the cell body (Zahner Manual)

The cell body is centered with a 6-mm-diameter Ag/AgCl reference electrode. The RE can be connected to the potentiostat with the help of black binding.

This setup is equipped with the UV light code number LS365-3, with a wavelength of 365nm and an intensity of 350 W/m², has been used to illuminate the sample.

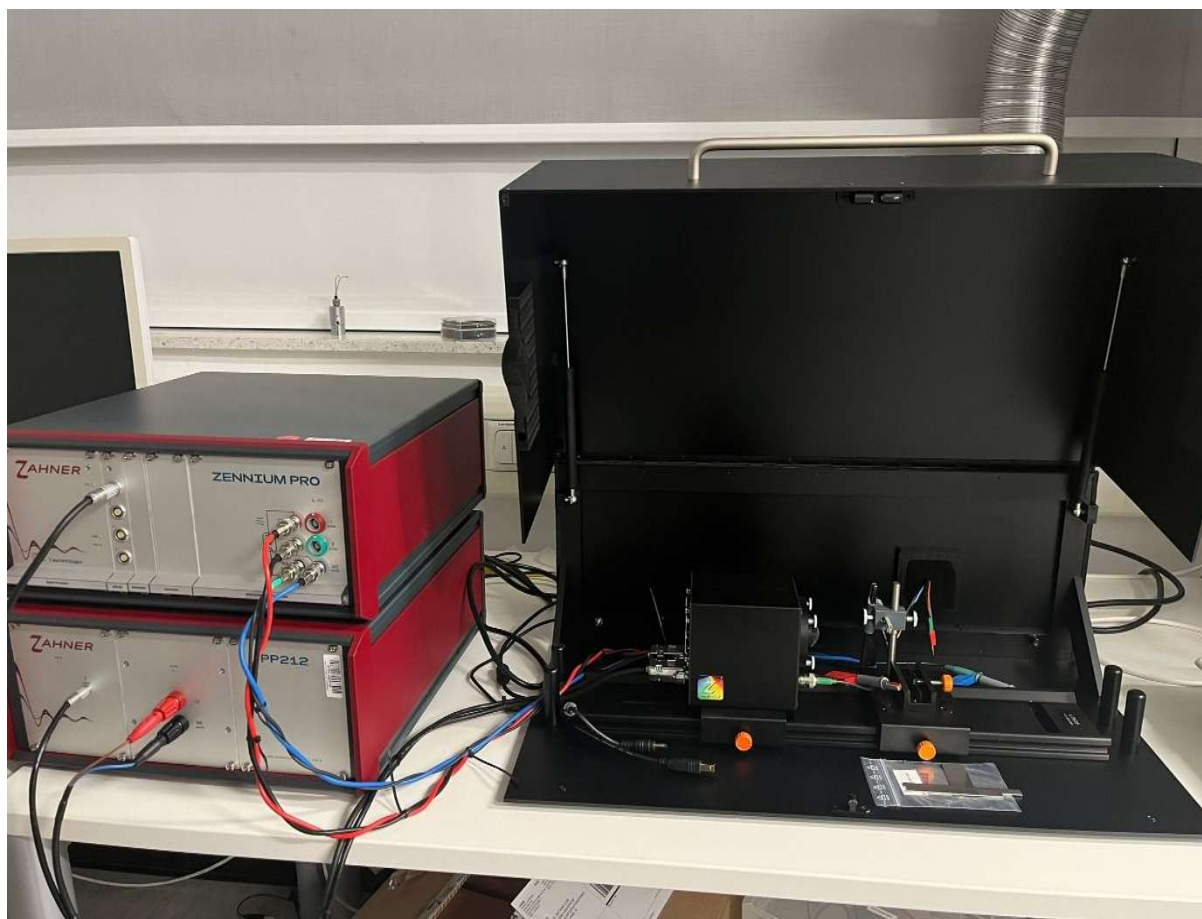


Fig 9: The Zahner Thales setup consists of a potentiostat, a galvanostat, and a black box for the sample and light source at I. Physikalisches Intsitut at Justus Liebig University Giessen used for samples characterization.

The potentiostat/galvanostat (PGSTAT) precisely controls the voltage between the reference electrode (RE) and the working electrode (WE) to define the potential difference between them.

2.4 Physicochemical Characterization:

Material synthesis

Molecular Beam Epitaxy:

Molecular beam epitaxy (MBE) is an advanced physical vapor deposition technique used to grow thin films with very high crystallinity, precise layer sequences, and controlled doping profiles. MBE operates under ultra-high vacuum (UHV) conditions and uses materials in their most basic, high-purity form to minimize contamination within the thin films. The elements are arranged so that they only react with each other on the heated substrate. The constant flow of elements from the educt enables to grow the desired crystal phases, rather than allowing for the thermodynamically stable growth of the material³⁰.

The element reaching the substrate is subject to physical processes such as desorption, adsorption, and diffusion. These reactions are manipulated by the MBE setup through adjustments made to the substrate temperature (T_{sub}), substrate properties, and the flux of the educt beam. Figure 10 shows the schematic diagram of the MBE chamber used to produce our c-III nitride samples. Effusion cells supply Group III elements (Al, Ga, and In) to facilitate the growth of III-nitrides on the sample. The beam of element fluxes has a dependence on the temperature of the cells. The movable pressure gauge enables precise calibration of pressure near the sample. The ultimate pressure value is referred to as BEP (beam equilibrium pressure).³¹ Ultra-high vacuum (UHV) conditions are created within the reaction chamber by a turbomolecular pump and a liquid nitrogen cryo shield. In this configuration, a radio-frequency plasma generator (Oxford Applied Research HD25) supplies the reactive nitrogen species³⁰. The reduction in background pressure leads to a reduction in contamination and the ability to use reflection high-energy electron diffraction (RHEED) for in situ observation of the sample surface.

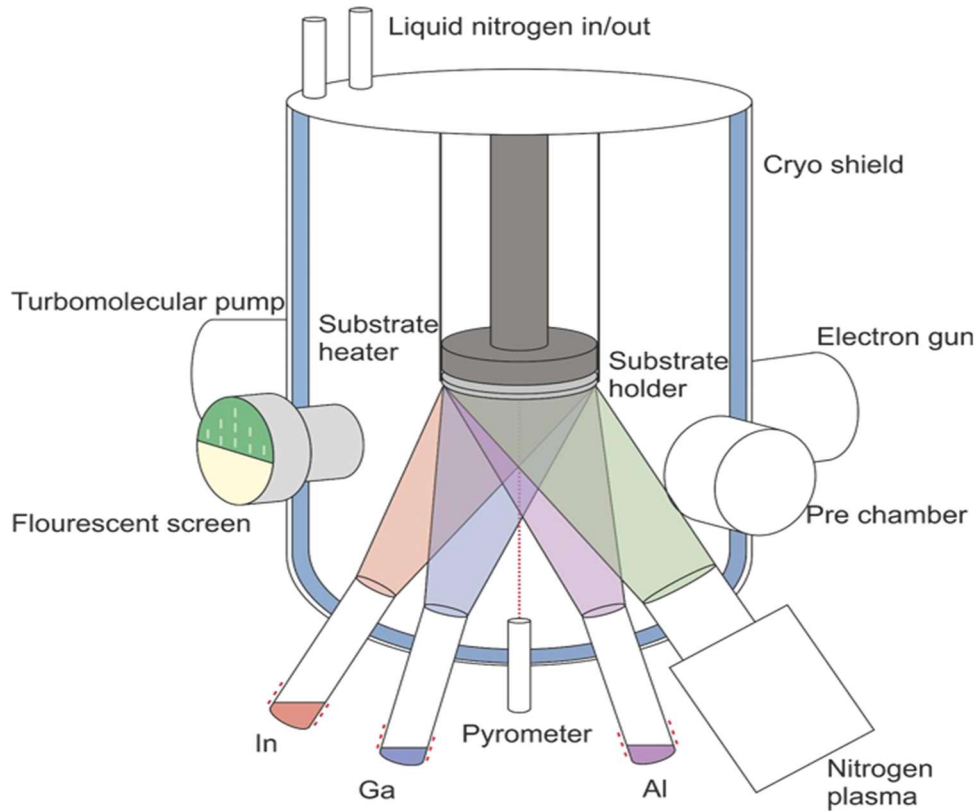


Fig 10: Schematics of an MBE main chamber. Orange (In), blue (Ga), purple (Al) and green (N) shading represent the impinging material fluxes.³⁰

Sample Structure

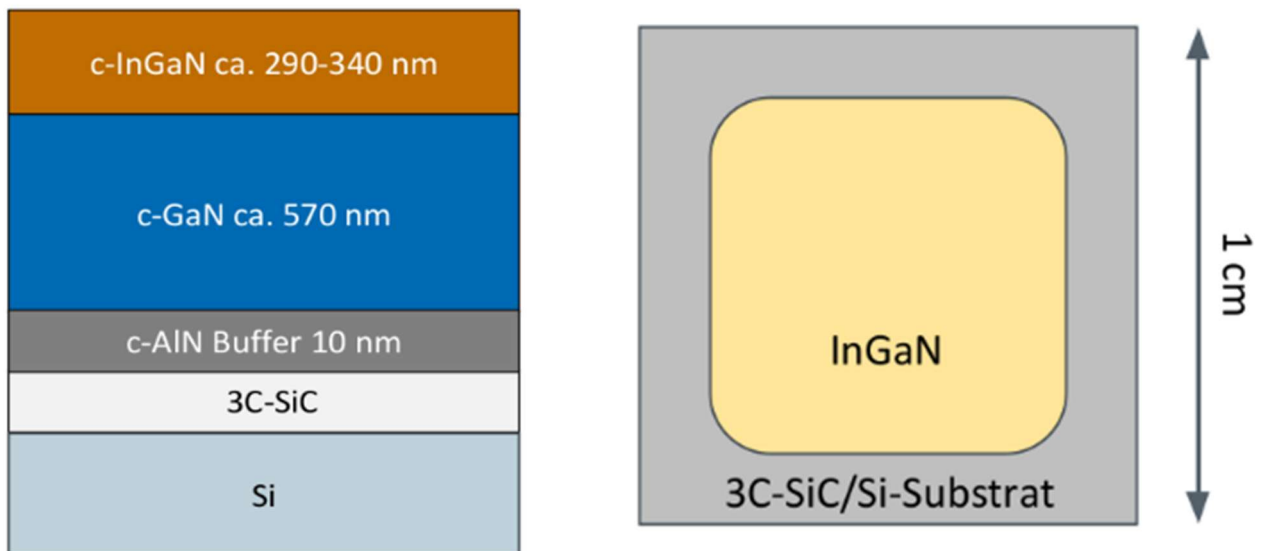


Fig 11: Schematic sample grown by MBE layer structure of the samples.

Molecular beam epitaxy was used to grow c-InGaN on a Si/SiC substrate. To match the lattice parameters, the sample was buffered by growing additional layers of c-AlN and c-GaN on the Si substrate.

The detailed information on the samples investigated in this thesis are listed in table 2.

Parameters	(In,Ga)N	Ge doped (In,Ga)N	Ge doped (In,Ga)N	Ge doped (In,Ga)N
Temperature Ge	--	850°C	950°C	1000°C
Photoluminescence (299K) eV	2.08	2.15	2.41	3.11
Ge-concentration (expected)	--	$\sim 10^{19} \text{ cm}^{-3}$	$\sim 10^{20} \text{ cm}^{-3}$	$\sim 5 \cdot 10^{20} \text{ cm}^{-3}$
In concentration	0.18	0.17	0.18	0.11

Table 2: Properties of the Ge doped n-type cubic InGaN layers investigated

Table 2 shows c-InGaN samples with different concentrations of Ge doping. The Ge concentration was estimated from photoluminescence measurements confirming an increase in doping. At the same time, however, a difference in the concentration of indium has been observed. This raises the question of whether the increase in the bandgap is due to an increase in Ge or a decrease in indium. However, this is not the focus of this thesis. The effect of doping on stability, photocurrent, and impedance spectroscopy is investigated to characterize the processes can be observed to see the processes taking place between the electrode and the electrolyte. The Mott-Schottky analysis is used to determine the donor concentration and flat band potential.

2.5 Secondary Mass Ion Spectrometry (SIMS)

The SIMS technique is based on a sputtering phenomenon that can be described as a cascade of collisions of particles within the analyzed sample. Secondary ions of the sample are ejected after the sample surface is struck by ions from a primary ion source. The secondary ions are collected and analyzed given information on the sample composition. It also happens when sample atoms that are already moving collide indirectly with each other (knock-on effects). The energies of the primary ions are often in the keV range. Therefore, in the event of a direct collision between primary ions and atoms in the sample, the energy is considerably higher than the energy of bonds between atoms. Such collisions result in substantial

disruption and bond breaking in the close vicinity of the impact site, causing the emission of atomic particles and secondary ions³².

The energy of the collisions decreases as the collision cascade moves away from the site where the collisions occurred. This causes less fragments and bond breaks, resulting in the dispersion of molecular fragments. The energy of particles produced in the top 2–3 monolayers (ML) of the sample is sufficient to overcome the surface binding energy and cause them to leave the sample. The mass-to-charge ratio (m/z) of the secondary ions is analyzed to obtain positive and negative secondary ion mass spectra consisting of the ion m/z versus the number of ions detected at each m/z . The primary ion dose during an experiment must be in the "static SIMS regime" to maintain sensitivity to the uppermost monolayers and minimize sample damage³³. These requirements can only be met if the total number of primary ions in the analysis area is low enough to guarantee that a particular region is unlikely to be hit by a primary ion more than once.

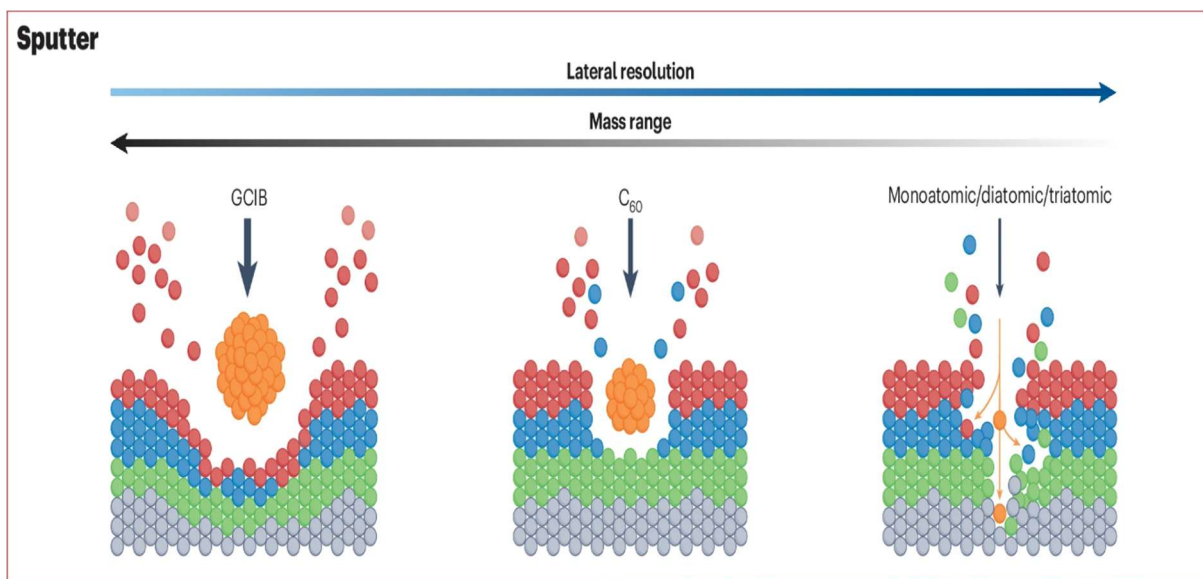


Figure 12: The secondary ion emission process initiated by the impact of a primary ion is shown here. Collisions produce atomic particles and secondary ions near the site of impact. Away from the point of impact, collisions emit molecular fragments^{32,34}.

The sample growing team at JLU Gießen carries out the SIMS measurements of the samples.

2.6 Scanning electron Microscopy (SEM) and Energy Dispersive X-ray Spectroscopy (EDX)

SEM is used to study the morphology of surfaces, micro/nano-structures, and topography of semiconductor working electrodes. The working principle involves focusing a high-energy electron beam on the surface of the sample and detecting the backscattered electrons, which provide information about grain size, surface roughness, cracks, defects, and layer homogeneity. These factors directly affect carrier transport and cell performance.³⁵

The contrast in scanning electron microscopy occurs when a beam of incident electrons hits the substrate and produces secondary electrons (SE), which are then backscattered. These high-resolution images provide crucial information about the surface. Backscattered electron images are sensitive to the atomic number of materials and reveal variations in composition or phase segregation³⁶.

EDX (energy dispersive X-ray spectroscopy) can be incorporated with SEM to provide elemental analysis. The working principle is that the electron beam interacts with the substrate, which, in our case, is a semiconductor. The electrons excite atoms in the sample and eject electrons from the inner shells bound to the nucleus. An electron from an outer shell fills the hole releasing X-rays. The emitted X-rays are relevant to the specific energy level ($K\alpha$, $K\beta$). EDX analyzes these X-ray energies to provide qualitative and quantitative information about the elements in sample³⁷. For nitride materials such as indium gallium nitride (InGaN), this technique can provide compositional information about indium and gallium, as well as detect unwanted impurities, such as oxide species.

Topographical mapping in EDX helps analyze element distribution on the surface or cross-section of a substrate. A homogeneous distribution of elements indicates uniform film growth, while enriched localizations display state defects, inhomogeneous doping, and clustering. For instance, in PEC analysis, the topographical map can reveal whether the catalyst (e.g., Co, Ni, or Pt) is deposited uniformly or forms clusters that alter the kinetics of surface charge.

EDX analysis helps to compare the integrity of the sample before and after photoelectrochemical analysis. During the activity, there is a possibility of forming an oxide layer on the surface due to surface corrosion. The dissolution of the surface within an electrolyte and surface corrosion can be measured by comparing the pre- and post-analysis compositional profiles of the sample. As in the case of InGaN analysis, there is a high likelihood of forming oxides or defects under conditions such as high voltages. Therefore,

SEM-EDX can provide a map showing shifts in the morphology of the material, and regions rich in oxygen can be detected in the EDX spectra.³⁸The efficiency of water splitting is affected by material composition and morphology. Likewise, surface area increases with roughness and carrier transport improves with uniform composition. This technique provides information on the structure and chemical properties, which helps us compare with PEC performance. Thus, combining SEM and EDX provides a better understanding of the quality of the material and the stability of the electrode/electrolyte in PEC systems.³⁹



Figure 13: SEM\EDX at Physikalisches Intsitut at Justus Liebig University Giessen used for samples characterization.

Electrochemical Characterization

2.7 Open circuit potential (OCP):

The open circuit potential gives the equilibrium voltage of an electrode in an electrolyte in the absence of an external current. It represents the balance between charge recombination, separation, and oxidation-reduction reactions at the electrode/electrolyte interface. In the dark, the open circuit potential (OCP) is given by the difference in the Fermi level of a material and the oxidation-reduction couple inside the electrolyte. The Fermi level is present near the conduction band for an n-type semiconductor, resulting in a negative open circuit potential. For a p-type semiconductor, the Fermi level is present near the valence band.⁴⁰ The negative potential of an n-type semiconductor in contact with an electrolyte arises as electrons tend to flow from the electrode to the electrolyte, creating upward band bending. As the electron concentration increases, the Fermi level shifts upward toward the conduction band in order to maintain equilibrium. Parameters such as adsorbed species, surface states, and oxide layers changing the open circuit potential (OCP) by alter or pin the Fermi level at the surface.

In the presence of light, the excitation of electrons from the valence band to the conduction band changes the open-circuit potential as the absorption of light changes carriers' occupation in the bands described by the quasi-Fermi level. Typically, the illumination to more positive values result in an increase in the number of holes accumulated at the interface, which is an indication of the OCP values shifting in a positive direction.

Consequently, the band bends, thereby augmenting the oxygen evolution reaction (OER). Investigating the time-dependent open circuit potential change due to illumination yields information about charge recombination processes. The open circuit potential (OCP) can be used to gather important information about surface traps or slow charge transfer at the interface. This is done by monitoring its slow and steady elevation or gradual decay. Conversely, a rapid increase or decrease in the OCP suggests efficient charge separation and reduced recombination.⁴¹

OCP values differ due to differences in doping levels and alloy composition. This makes it important to characterize materials and design their properties accordingly. For example, doping Ge in InGaN increases the donor density, moving the Fermi level upward. The flat band potential is negative in the dark for photoanodes⁴². These measurements provide direct information about the electronic structure of the bulk.⁴³

OCP can also be used to determine the stability of a sample. A prolonged alteration in OCP indicates photocorrosion, oxidation of the surface, or degradation of the material. For a nitride-based semiconductor like InGaN, drifting first towards a positive OCP and then towards a negative OCP provides information about defects that alter the band alignment at the interface or oxide formation on the surface.

2.8 Chopped Light Voltammetry (CLV)

Chopped light voltammetry is an electroanalytical technique combining conventional voltammetry with periodic electrode surface illumination. This approach is especially advantageous for the study of photoelectrochemical processes and the analysis of photosensitive materials. The working electrode is subjected to light that is intermittently switched on and off (chopped) in chopped light voltammetry, while a voltage is applied. The resulting current comprises light and dark signal components, which allows researchers to distinguish photocurrent from dark current. This separation provides insight into photoelectrochemical reactions that occur at the electrode-solution interface⁴⁴.

2.9 Cyclic voltammetry in PEC

Cyclic voltammetry is one of the most important techniques for understanding redox behavior, charge transfer kinetics, and processes that occur at electrode interfaces. In cyclic voltammetry analysis, the current is measured as the WE (working electrode) potential sweeps between two limits linearly. This provides insight into the redox reaction for water splitting, as well as the onset of oxygen evolution reaction (OER) and hydrogen evolution reaction (HER). Fig 14 shows the oxidative scan for Hydrogen evolution reaction and reductive scan for oxygen evolution reaction.

CV helps to understand the processes with and without illumination in photoelectrochemical analysis. The dark spectra give information about the intrinsic electrochemical behaviour of the material. However, when the sample is exposed to light, an increase in current is seen. This is because the electrons are excited by the photons. Additionally, shifts in the onset potential can be seen allowing the analysis of the charge carriers generated by photons that participate in oxygen and hydrogen evolution reactions. Through this analysis, we can relate the quality of materials to modifications in doping concentration.

The CV graph helps to distinguish between capacitance and faradaic behaviour. The current response is symmetric and rectangular for capacitive behavior, while a peak-shaped response has been observed in diffusion reactions, as shown in Fig. 14. The transition from capacitive

to faradaic behavior occurs when charge carriers begin to participate in oxygen and hydrogen evolution reactions.⁴⁵

In conclusion, the CV provides a quick, explanatory approach for dealing with carrier transfer behavior and catalytic responses. It also helps determine the onset potentials of photoanodes and photocathodes in terms of n-type and p-type semiconductors.⁴⁶ The combination of Mott-Schottky analysis and CV provides a better understanding of the absorption of photons by the material, as well as charge separation and the water-splitting half-reactions.

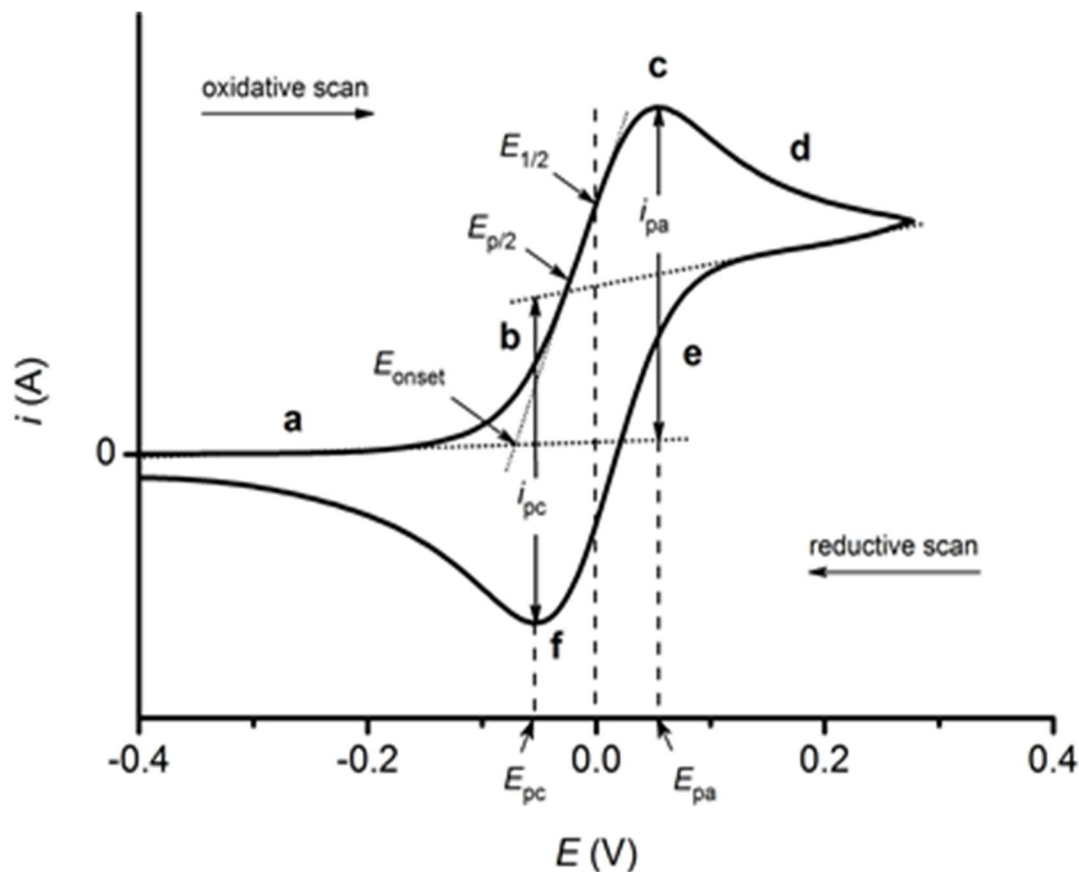


Fig 14: schematic diagram of cyclic voltammogram showing oxidation and reduction behavior reprinted from Ossila⁴⁷

2.10 Electrochemical Impedance Spectroscopy:

The EIS technique uses a small sinusoidal signal (voltage or current) that is added to a DC signal (voltage or current) in an electrochemical system. The resulting response (current or voltage, respectively) is measured over a wide range of frequencies. To ensure a linear

relationship between the applied signal and the system's response, it is essential that measurements are conducted by applying a small-amplitude perturbation⁴⁸.

The instantaneous value of a sinusoidal signal, $x(t)$, is given by the projection of a rotating vector of length X_o rotating anticlockwise at the cosine axis (perpendicular component) of a trigonometric circle with constant angular frequency ω , as shown in Figure 5. At $t = 0$, a 360° revolution ($\omega t = 2\pi$) produces a sinusoidal waveform from 0 to 360° . At 90° ($\pi/2$) and 270° ($3\pi/2$), the cosine component has its highest values ($+X_o$) and lowest values ($-X_o$), respectively. The instantaneous values of the sinusoidal signal x are given by the equation

$$x(t) = X_o \sin(\omega t) \quad (5)$$

where ω is the angular frequency in rad/s and X_o is the amplitude of signal. X_o is also known as the peak signal (X_p), while X_{pp} is the peak-to-peak signal, which is equal to $2X_p$.

The root-mean-square (rms) value or effective signal of a sinusoidal signal with respect to the X_o is defined as

$$X_{rms} = \frac{X_o}{\sqrt{2}} = 0.707X_o \quad (6)$$

The spatial properties of the sinusoidal signal can be shown by the frequency f (cycles per second) in Hertz (Hz) and the period T (the duration required for one complete cycle) in seconds (s), which are interrelated along with the angular frequency by the equation.

$$\omega = 2\pi f = \frac{2\pi}{T} \quad (7)$$

For instance, if the sinusoidal signal in Figure 5 has a period $T = 0.5$ s, the frequency $f = 2$ Hz.

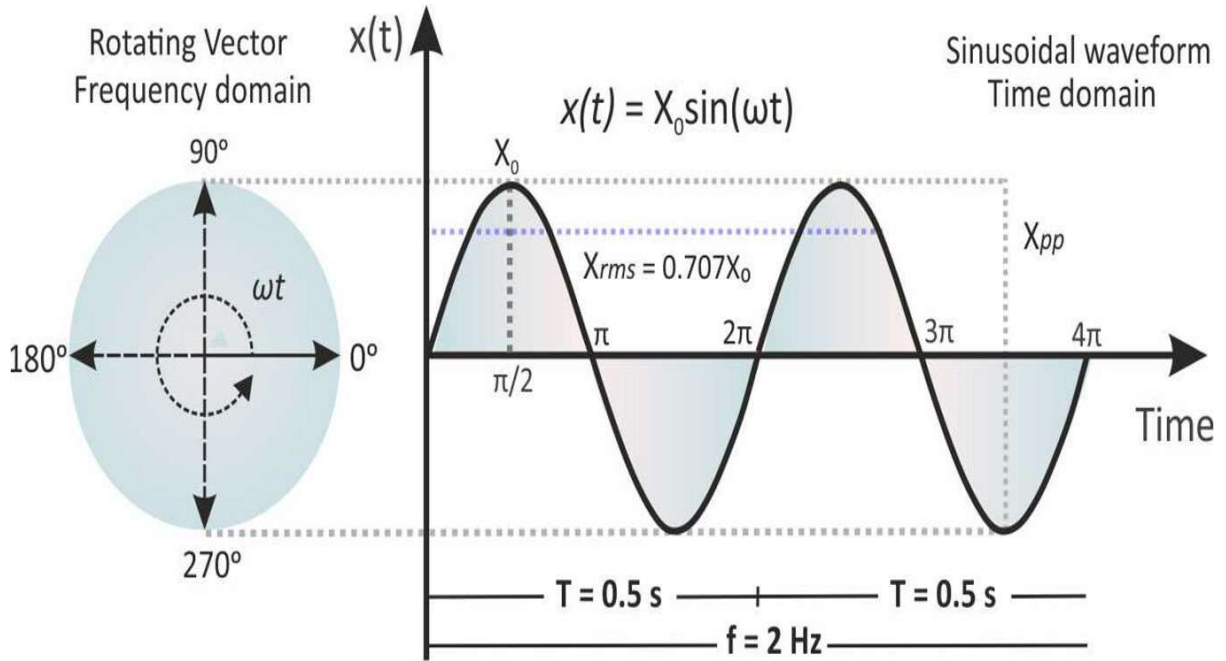


Fig 15: Representation of the sinusoidal signal, $x(t) = X_0 \sin(\omega t)$, and a vector revolving at a constant angular frequency ω .²⁵

The periodic signal can be described as complex number (z)

$$z = a + jb \quad (8)$$

where a is the real part, b is the imaginary part and j shows the imaginary unit, $j^2 = -1$. Both a and b are real numbers but the real number of y-axes is multiplied with imaginary unit j . We use the symbol z' or $Re\{z\}$ and z'' or $Im\{z\}$ respectively.

$$z = |z|(\cos(\varphi) + j\sin(\varphi)) \quad (9)$$

where,

$$a = |z| \cos \varphi \quad (10)$$

$$b = |z| \sin(\varphi) \quad (11)$$

$$|z| = \sqrt{a^2 + b^2} \quad (12)$$

$$\tan \varphi = \left(\frac{b}{a}\right) \text{ and } \varphi = \tan^{-1}\left(\frac{b}{a}\right) \quad (13)$$

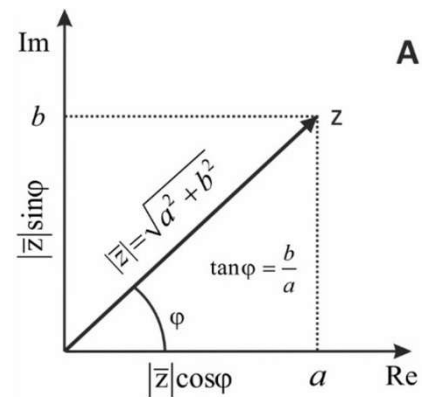


Fig 16: Representation of complex number z .

The Impedance of electric circuit

Impedance measures the total resistance to the current flow in an electrical circuit made up of resistors (R), capacitors (C), and inductors (L). The impedance of the electrical circuit under test will differ depending on the different passive elements (R, C, L) included in the circuit and the manner in which they are connected to each other. Assuming a low-amplitude alternating voltage at a particular frequency

$$V(\omega) = V_0 \sin \omega t \quad (14)$$

is applied to the electrical circuit and alternating current in response at same frequency is observed

$$I(\omega) = I_0 \sin \omega t + \varphi \quad (15)$$

The impedance of the circuit at same frequency is given as

$$Z(\omega) = \frac{V(\omega)}{I(\omega)} \quad (16)$$

$$Z = |Z|(\cos(\varphi) + j\sin(\varphi)) = z' + jz'' \quad (17)$$

Where z' representing real part on the x-axis and z'' is the imaginary part at y-axis of nyquist plot, $|z|$ is the module of impedance, and $\varphi = \omega t$ is the phase. In comparison to equation (10), (11) and (12), we can write;

$$z' = |z| \cos \varphi \quad (18)$$

$$z'' = |z| \sin(\varphi) \quad (19)$$

$$|z| = \sqrt{(z')^2 + (z'')^2} \quad (20)$$

$$\tan(\varphi) = \frac{z''}{z'} \text{ and } \varphi = \tan^{-1} \left(\frac{z''}{z'} \right) \quad (21)$$

Despite of its complex nature, the total impedance of circuit elements connected in series will follow Kirchhoff's law and is⁴⁹,

$$z_{eq} = z_1 + z_2 + z_3 + \dots \quad (22)$$

While the impedance of equivalent circuits connected in parallel is given by

$$\frac{1}{z_{eq}} = \frac{1}{z_1} + \frac{1}{z_2} + \frac{1}{z_3} + \dots \quad (23)$$

The measured spectrum is described by an equivalent circuit and to collect the numerical data of the components included in the circuit. So, one can use several software that comes with the response of frequency such as Zview, Zplot, RelaxIS and others. It is to keep in mind there is not a single equivalent circuit for a given impedance spectrum⁵⁰. The description of a measured impedance simulation of spectrum is possible with one or more circuits as shown in figure 17.

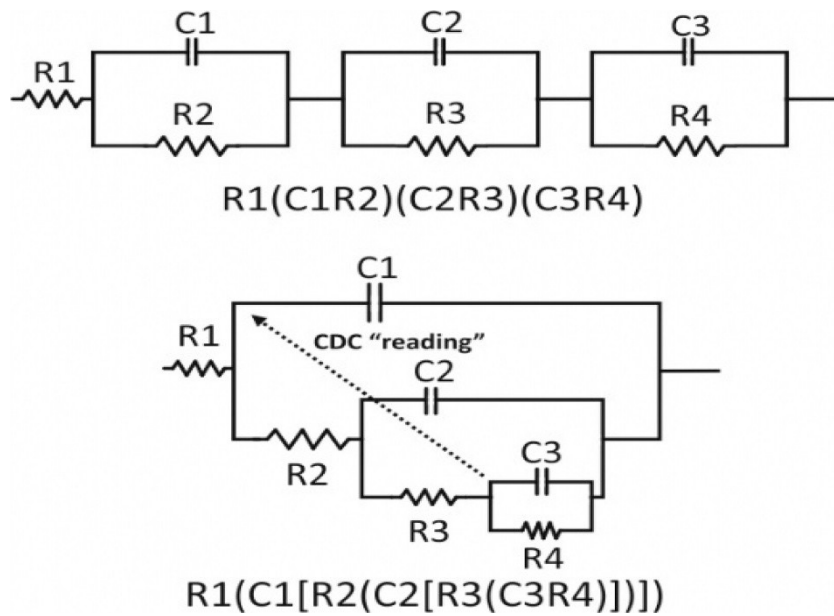


Figure 17: Different equivalent circuit describing the same impedance spectrum.

Electrical circuits can be written as circuit description codes (CDC) given by Boukap⁵¹. Equivalent circuits can often be described as series combination of RC elements i.e. resistance R connected in parallel to capacitor C . If this complex circuit is connected with one more resistor so we can write it as $R(RC)$ and so on.

Nyquist plot shows the negative impedance plot versus the real part, while in the Bode plot, the magnitude of the impedance and the phase are plotted versus the logarithm of the frequency. The Nyquist and Bode plots for a single resistor and single capacitor are shown in figure 18. Figure 18 shows that we have only a resistor R_1 , the impedance is given to be $z = R$. The real part shows the resistance while the imaginary part is zero. So, the Nyquist plot shows a single point on the x-axis.

$$|z| = \sqrt{(z')^2 + (z'')^2} = \sqrt{(R_1)^2 + (0)^2} = R_1 \quad (24)$$

Whereas the bode magnitude is the Bode phase plot shows a straight line that crosses the right axis at $\varphi = 0$. Figure 9B shows a single circuit containing only a capacitor. The impedance is then given by

$$Z = X_C = 0 + \frac{1}{j\omega C} = 0 - j\left(\frac{1}{\omega C}\right) \quad (25)$$

Eq (24) tells us that real part (resistance) is zero while the imaginary part is inversely proportional to the frequency and the capacitance. The Nyquist plot shows a straight line on the y-axis (the real part of the impedance is zero). Values near zero corresponds to high frequencies while at a high impedance, the frequency tends to go to zero.

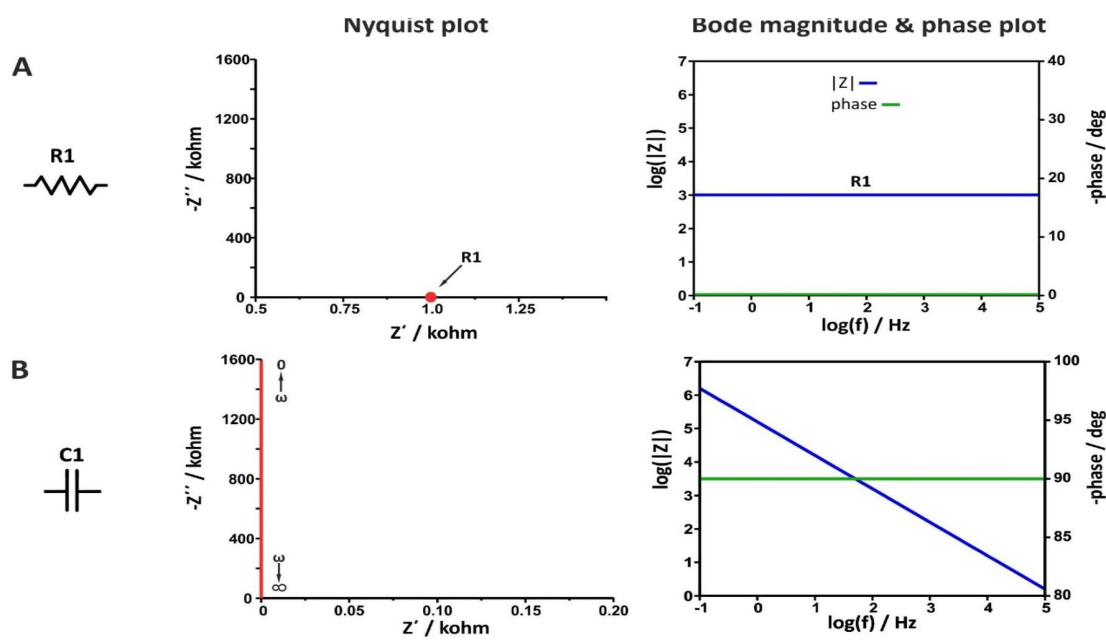


Figure 18: Representation of Nyquist plot and Bode plots for (a) a single resistance $R1 = 1\text{k} \Omega$ and a capacitance $C1 = \frac{1}{\omega|Z|}$.⁵²

The Bode phase angle shows a straight line that crosses the axis $\varphi = -90$, capacitor means the waveform of voltage and current is out of phase with $\pi/2$. However, in real electrochemical cells the phase between current and voltage due to capacitive element is typically lower than $\pi/2$. Due to non-ideality effects modelled using the impedance as constant phase element (CPE) instead of an ideal capacitor (C)⁵².

Let's assume a simple case where resistor is connected with a capacitor in parallel, shown in figure 19 the impedance is given by.

$$z(\omega) = \frac{1}{\frac{1}{R1} + j\omega C1} = \frac{R1}{1 + j\omega R1C1} = \frac{R1}{1 + (\omega R1C1)^2} - j \frac{\omega(R1)^2 C1}{1 + (\omega R1C1)^2} \quad (26)$$

The Nyquist plot corresponds to a semi-circle. At very high frequencies, the circuit behaves like a short circuit and all the current passes through the capacitor ($\omega \rightarrow \infty, X_C \rightarrow 0$), while at very low frequencies all the current passes through the resistor ($\omega \rightarrow 0, X_C \rightarrow \infty$). At intermediate frequencies, the current flows through both the circuit components at the same time, the ratio tells us the opposition current flow at each branch⁵³. While going from high to medium frequencies the capacitive reactance becomes higher ($X_C < R1$) which leads to more alternating current to pass through the capacitor compared to the current going through the resistor. However, there is a characteristic frequency in which the resistance and capacitive reactance become equal. At this frequency the imaginary part of impedance is maximum⁵⁴.

$$\omega_{z''_{max}} = \frac{1}{\tau} = \frac{1}{R1C1} \quad (27)$$

with $\tau = R1C1$ and by arranging eq (26) $R1 = \frac{1}{\omega_{z''_{max}} C}$, eq (25) becomes

$$z(\omega) = \frac{R1}{2} - j \frac{R1}{2} \quad (28)$$

So, at this frequency, we can find τ . Bode phase angle plot in figure 19 shows at very low frequencies $|z| = R1$, while at high frequencies $|z| = \frac{1}{\omega C}$. The slope curve in the Bode magnitude plot changes and the breaking point is highlighted with a circle corresponds to time constant (τ) of the system.

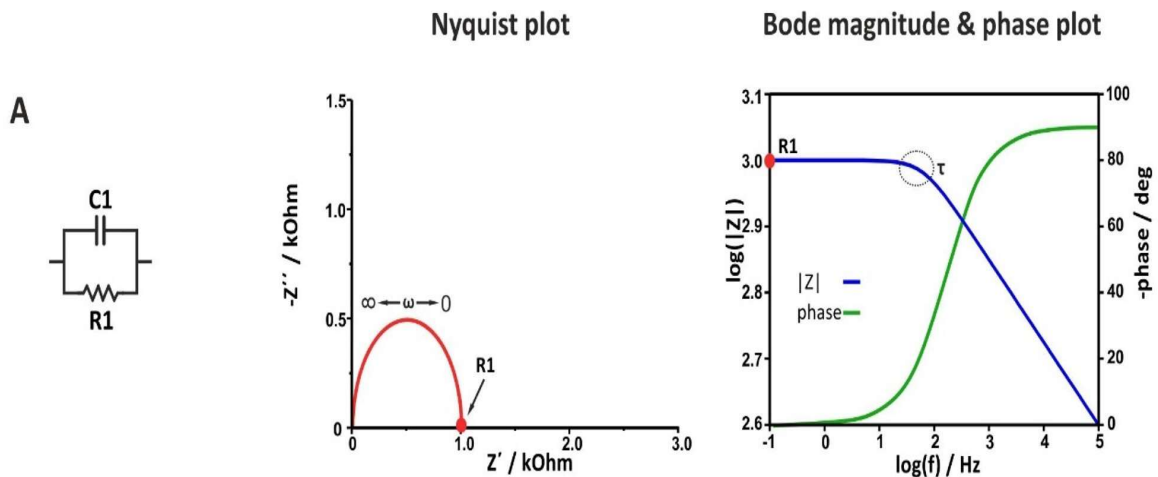


Figure 19: Nyquist and Bode plot of an RC element where a capacitor is connected in parallel to the resistor²⁵.

Semiconductor electrolyte Interface

When a semiconductor substrate is immersed in an electrolyte, charge transfer occurs until the system reaches equilibrium. The alignment of the Fermi level of the semiconductor with the redox potential of the electrolyte causes band bending in the semiconductor by proximity to the interface. The process of band bending gives rise to a space charge region, also referred to as a depletion layer or space charge layer. Within this region, the presence of mobile charge carriers is reduced⁵⁵.

Mott-Schottky Analysis

It is crucial to emphasize that semiconductors demonstrate wholly distinct electrochemical response in contrast to standard, highly conductive electrode materials (e.g., glassy carbon or platinum). The formation of a space charge region that extends from the surface into the material complicates the electrochemistry of semiconductors. A Mott-Schottky measurement investigates the capacitance of the space charge region. Mott-Schottky analysis is a potent electrochemistry method employed to describe semiconductor electrolyte interfaces⁵⁶. When a semiconductor gets in contact with an electrolyte charge redistribution at the surface occurs, creating a space charge region. The width and capacitance of this region depend on the applied potential. The relationship between the potential, the region's width and capacitance is given by the basic Mott-Schottky equation

$$\frac{1}{C_{sc}^2} = \frac{2}{\epsilon\epsilon_0 N_D A^2} \left(E - E_{FB} - \frac{kT}{e} \right) \quad (29)$$

Where:

- C_{sc} is the space charge capacitance (F/cm²)
- ϵ is the dielectric constant of the semiconductor
- ϵ_0 is the permittivity of the free space (8.854×10^{-14} F/cm)
- e is the elementary charge (1.602×10^{-14} C)
- N_D is the donor density for n-type
- A is the electrode area (cm²)
- E is the applied potential (V)
- E_{FB} is the flat band potential (V)
- k is Boltzmann constant (1.381×10^{-23} J/K)
- T is the absolute temperature (K)

This relationship can be used to extract fundamental semiconductor properties. In Mott-Schottky analysis, the capacitance is measured as a function of the applied potential, and the inverse square of the capacitance ($1/C^2$) is plotted versus the potential (V). This technique has been used extensively in many areas, such as photocatalysis, corrosion studies, photovoltaic devices, and the characterization of electronic materials. The ability to analyze carrier concentration, doping density, and flat-band potential is indispensable. This analysis is crucial for comprehending semiconductor behavior. It is also essential for the optimization of material properties.

At room temperature (298K) the $kT/e \sim 0.026V$, which is very small compared to the applied potential, so can be omitted in most of the cases.

Data analysis and Interpretations

The capacitance can be calculated from the imaginary part of the impedance.

$$C = \frac{-1}{(2\pi f Z'')} \quad (30)$$

Where f is the frequency and Z'' is the imaginary part of impedance. The measured capacitance comprises of the contribution from the space charge layer, Helmholtz layer, and any surface states. In ideal scenario, the capacitance of space charge layer dominates.

By plotting $1/C^2$ versus applied voltage (V), a linear dependency is obtained as shown in figure 11. This region corresponds to the depletion area where Mott-Shotky equation is valid. The linear regression allows to determine carrier concentration and flat band potential from the slope m and the intercept u_o .

For carrier concentration

$$N_D = \frac{2}{\epsilon\epsilon_0 mA^2} \quad (31)$$

For flat band potential

$$E_{FB} = u_o - \frac{kT}{e} \quad (32)$$

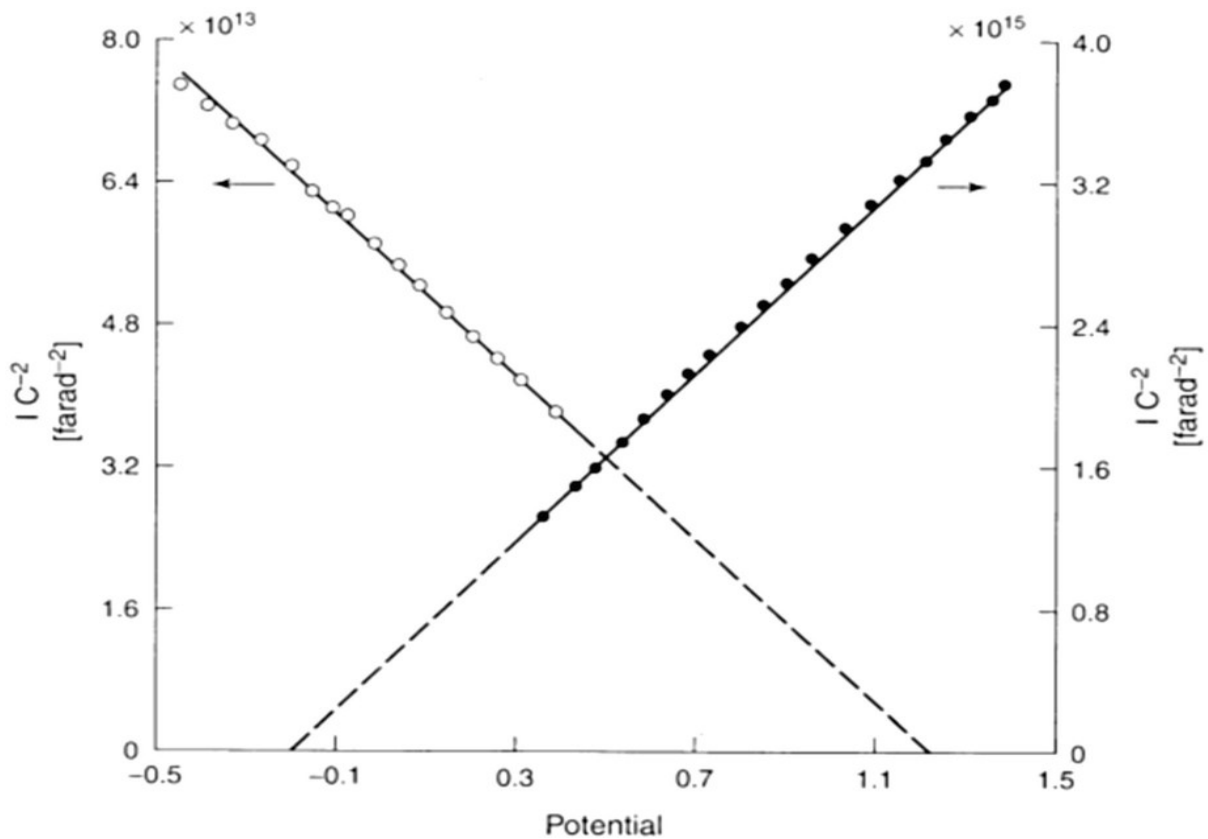


Fig 20: Schematic representation of Mott-shottky plot. The filled circle shows the n-type semiconductor and open circles shows the p-type semiconductor⁵⁷.

Deviations from the Ideal behaviour

There are several factors that can cause deviations from ideal Mott-Schottky behavior.

Surface states: The presence of trap states at the semiconductor surface can introduce capacitance due to additional charge, thereby altering the linear relationship.

Deep depletion: Equilibrium may be difficult to maintain due to the sluggish generation of minority carriers at very negative potentials.

Faradaic currents: Impedance measurements can be affected by electrochemical reactions.

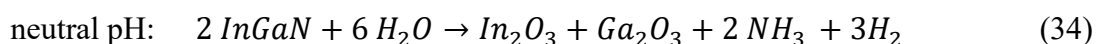
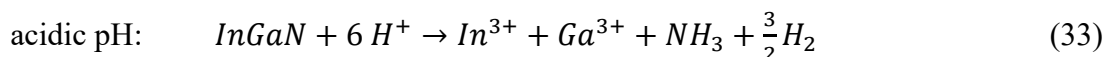
Non-uniform doping: The model assumes constant doping concentrations, so spatially varying concentrations violate this assumption⁵⁸.

Chapter 3: Results and Discussion

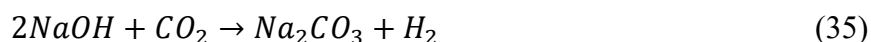
3.1 Electrolyte and reaction mechanism

The selection of electrolytes in photoelectrochemical cells is crucial, and it is challenging to achieve optimal activity in terms of solution resistance, carrier recombination, water polarization, and the rate of charge transfer between the electrode and the electrolyte interface¹⁴. In this work, sodium carbonate and bicarbonate to make a 0.05 M combined buffer solution with a pH of 11. This electrolyte was selected because it improves the activity of photoanodes and facilitates the oxygen evolution reaction. A higher pH is always a good option. Different electrolytes with different pH values (acidic, neutral and basic) have been assessed, and it has been observed that a higher photocurrent arises at acidic pH as in the case of 0.1 M H₂SO₄. However, the analysis revealed that the photoelectrodes highly unstable. The samples have been checked from negative to positive voltages, and it has been seen that the samples were highly corroded after the measurements. Thus, a phosphate buffered saline solution with a pH of approximately 7 was utilized reducing the observed photocurrent. This is attributed to a passivation of the InGa_{0.5}N sample. Possible reactions of InGa_{0.5}N at acidic and neutral pH are the following.

Reaction:



The acidic pH showed corrosion while at neutral pH, the Ga₂O₃ layer is insulating, which reduces the photocurrent. However, it protects the sample from corrosion. Both acidic and neutral pH electrolytes didn't work, so it was decided to increase pH. NaOH solution of pH 11 was the first option, but NaOH is unstable and hygroscopic, making it hard to balance with the substrate. After trying for hours to get stable OCP, it was found that NaOH changes pH over time. As a strong base, it reacts with the carbon dioxide in the atmosphere, lowering its pH which was checked after activity showed closed to neutral pH.



So, it is not a safe choice to use NaOH electrolyte, if it changes pH inside the cell and PEC cells used are not airtight. So, it can be an option if there is a control pH of NaOH.

Following that, to sustain pH, a buffer solution of 0.05 M $\text{Na}_2\text{CO}_3 + \text{NaHCO}_3$ (pH ~ 11) was utilized, with a voltage range of 0 V to 0.8 V. In this voltage range, no observable corrosion or passivation has been detected, along with a satisfactory photocurrent and stability of the substrate.

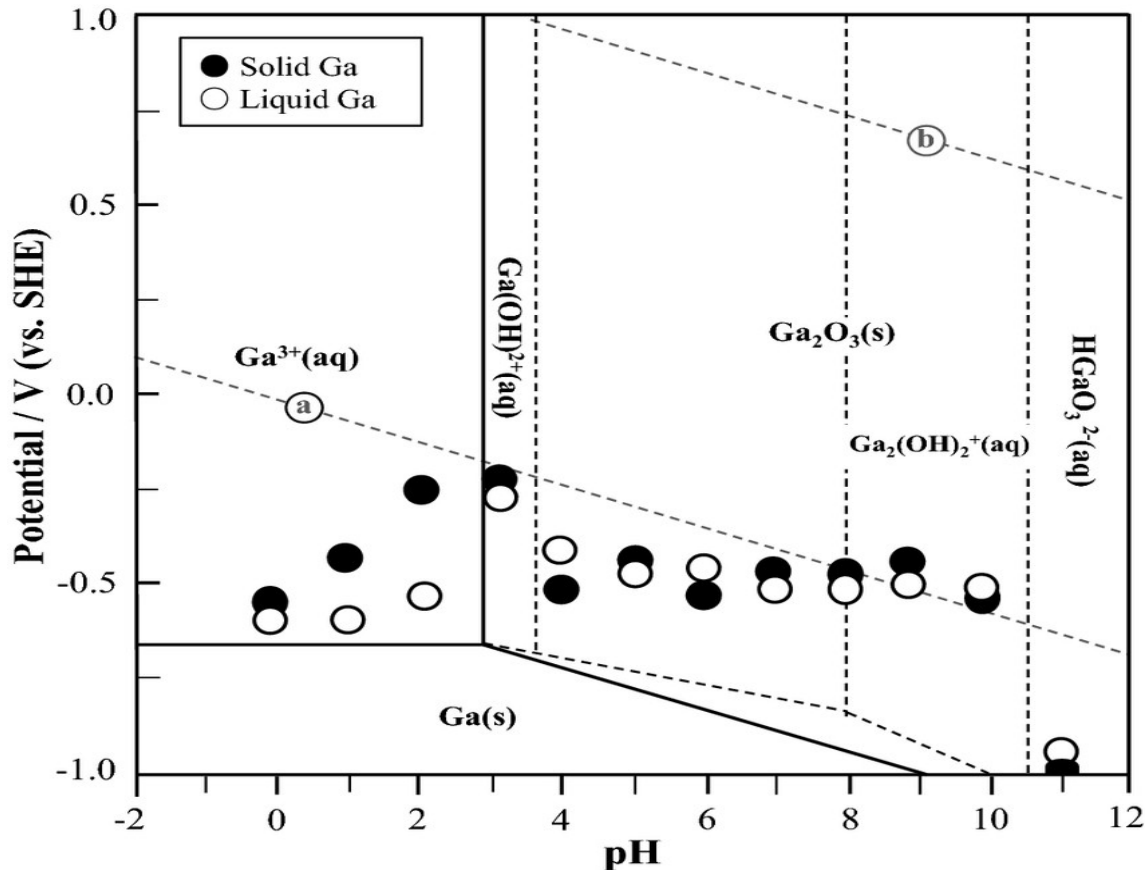


Fig 21: This schematic graph shows the voltage versus pH for gallium, including solid and liquid gallium, and how they respond to different voltages and pH levels.⁴⁸

Fig 21 shows the diagram of Ga to discuss the possible thermodynamically stable phases of an electrochemical system at acidic pH and negative voltages, metal Ga will remain in their state. Conversely, an increase in voltage and pH can form a passivating layer of gallium oxides. Therefore, the voltage and pH must be within a specific range so that the InGaN sample does not change into an oxide or gets corroded. The operating range for the sample is thus a pH of 11 and a voltage range of 0 to 800mV.

3.2 Chopped Light Voltammetry

N250926 and N250925:

These two samples are Ge-doped n-type c-InGa_{0.5}N doped at different temperatures, i.e., 850°C and 900°C. A 0.1 M H₂SO₄ solution was used as an electrolyte because, as shown in Fig. 22, GaN can be characterized at low pH (acidic) and negative voltages Vs RHE, but at voltages above 0 V, it changes to Ga³⁺ and corrodes the sample. However, this was not the best choice as explained in the electrolyte and reaction mechanism because the voltage window at low pH is very small, and there is also an In content. With a little illumination of the sample with UV light, corrosion was observed even at small voltages. After performing chopped light voltammetry, the samples could not be characterized further.

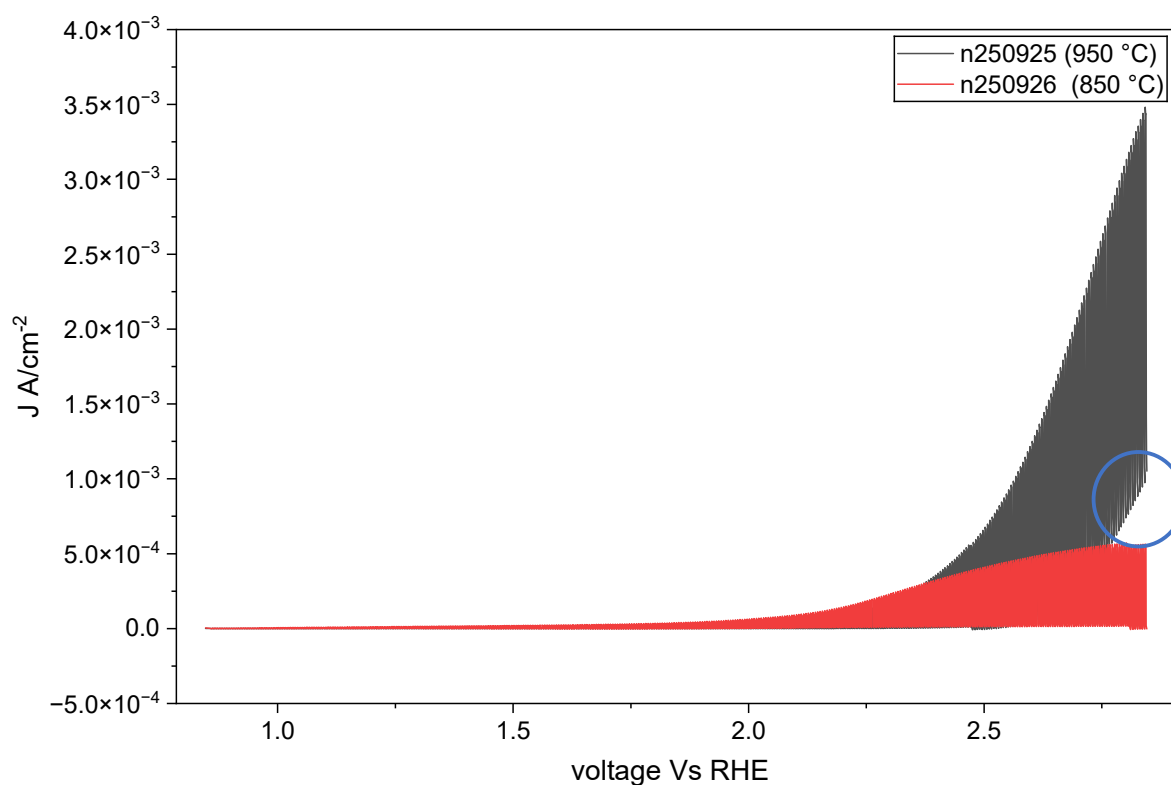


Fig 22: CLV graph of Ge-doped sample with acidic electrolyte showing degradation.

Figure 22 shows the chopped-light voltammetry of N250925 (Ge-doped InGa_{0.5}N grown at 850°C) and N250926 (Ge-doped InGa_{0.5}N grown at 950°C), which were analyzed with 0.1 M H₂SO₄ under UV illumination. A high photocurrent of around 1 mA/cm² has been observed compared to the buffer electrolyte, a topic discussed later in this chapter. SEM-EDX and SIMS data clearly indicates degradation and corrosion.

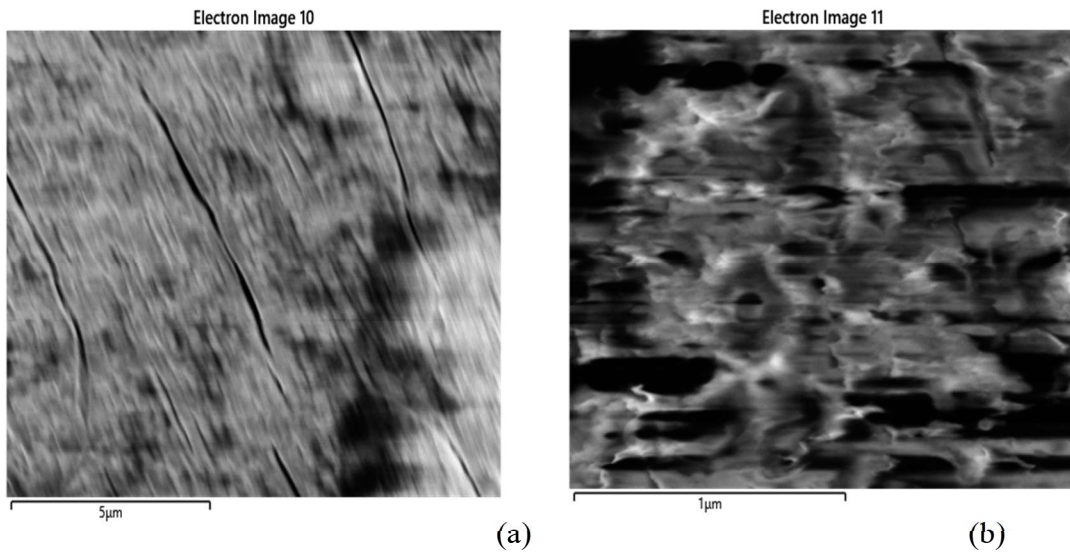


Fig 23: SEM images (a) n250925 and (b) n250926 showing corrosion after PEC analysis

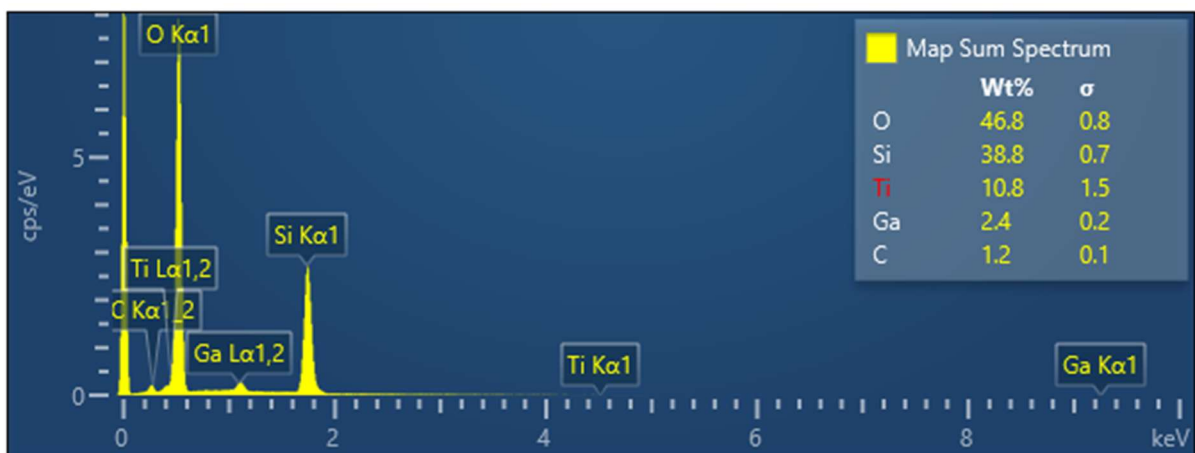


Fig 24: EDX analysis of the n250925 surface

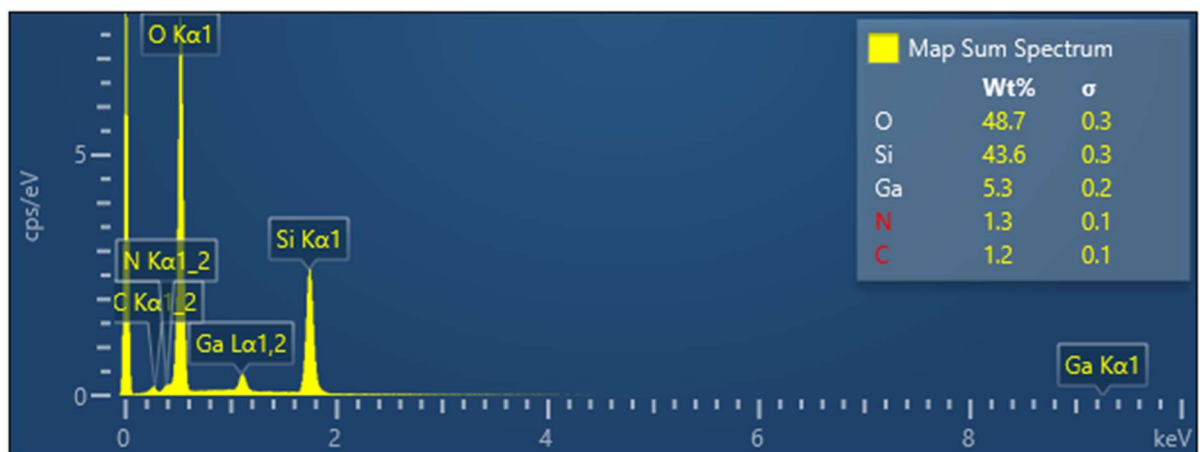


Fig 25: EDX analysis of the n250926 surface.

The SEM EDX measurements were performed after the CLV to confirm the degradation. The images in fig 23 shows the surface topography and Fig 24 and 25 shows the corresponding EDX analysis revealing that indium and gallium concentrations are negligible to observe. It clearly indicates the corrosion and damages of the sample.

3.3 SIMS comparison of samples after analysis in different electrolytes

Ge-doped InGaN grown at 850 °C

The SIMS data also showed the corrosion of a Ge-doped InGaN sample that was analyzed under acidic conditions (i.e., 0.1 M HCl), as shown in Figure 26.

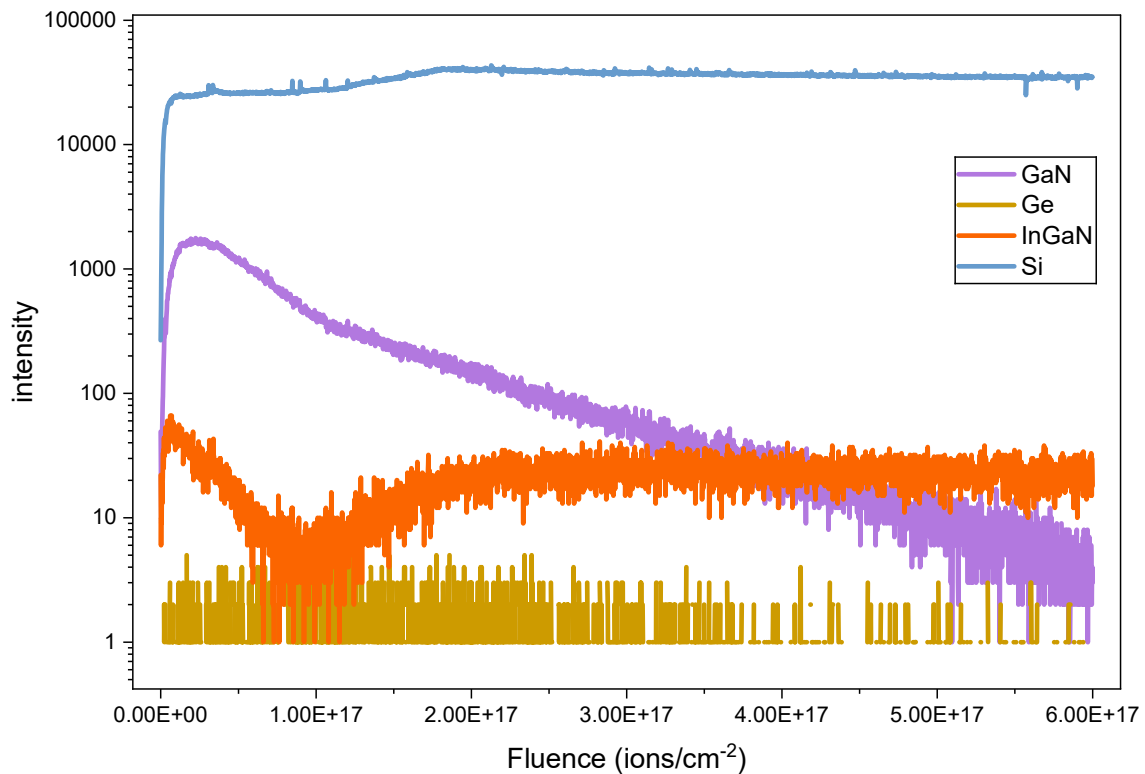


Figure 26: SIMS depth profiles of Si, Ge, GaN and InGaN under acidic pH.

The graph clearly shows the rapid drop in InGaN and GaN concentrations, revealing only noise. The clear Si data shows only the substrate, as all other deposition has corroded away.

(In,Ga)N

The SIMS data of the undoped InGaN substrate analyzed under basic conditions showed a constant concentration of InGaN and GaN after analysis in a buffer solution, as shown in Fig. 27.

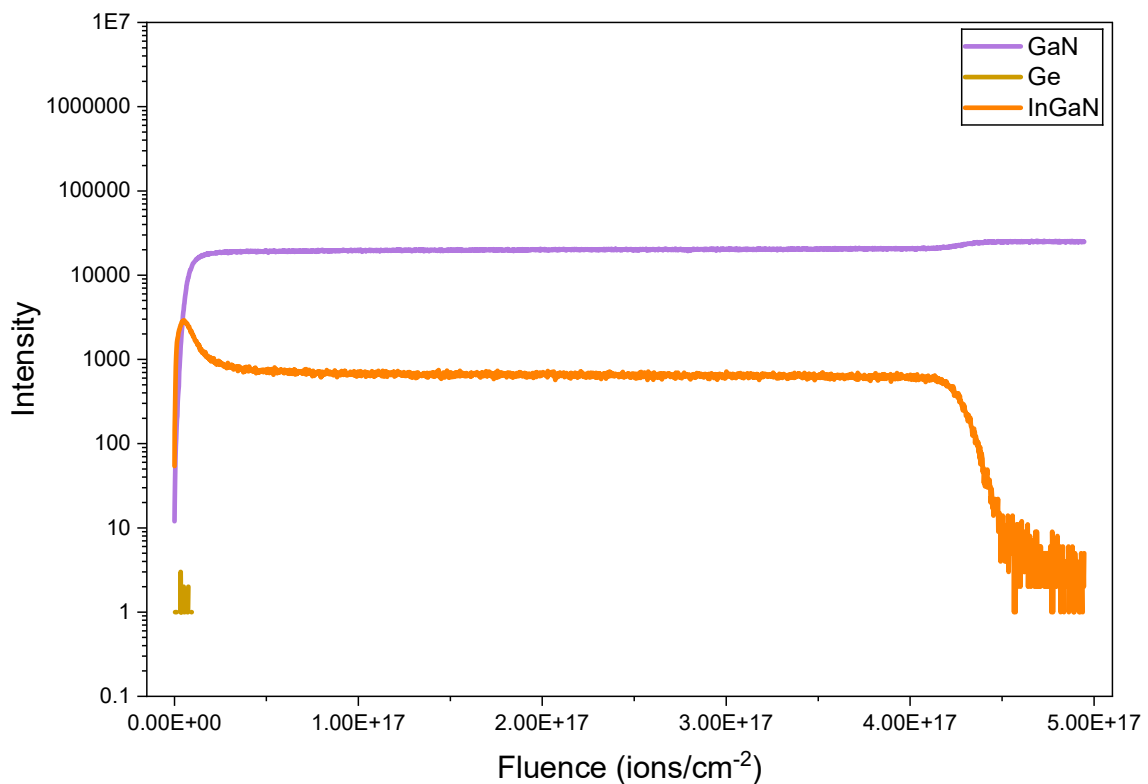


Figure 27: SIMS depth profiles of Ge, GaN and InGaN under basic pH.

The graph clearly shows a constant concentration, confirming that the analysis is purely from the InGaN layer, without interference from other layers.

3.4 SIMS Investigation of Ge incorporation into the different InGaN thin films InGaN

Secondary Ion Mass Spectrometry (SIMS) was performed to investigate the incorporation of germanium (Ge) into the InGaN layers that were grown at varying temperatures. SIMS measurements were performed for undoped reference sample and

Ge-doped InGaN layers grown at 850 °C, 950 °C, and 1000 °C and the intensity profiles of all samples are shown in the following intensity is plotted versus the fluence that is the total number of ions that have bombarded the sample per unit area.

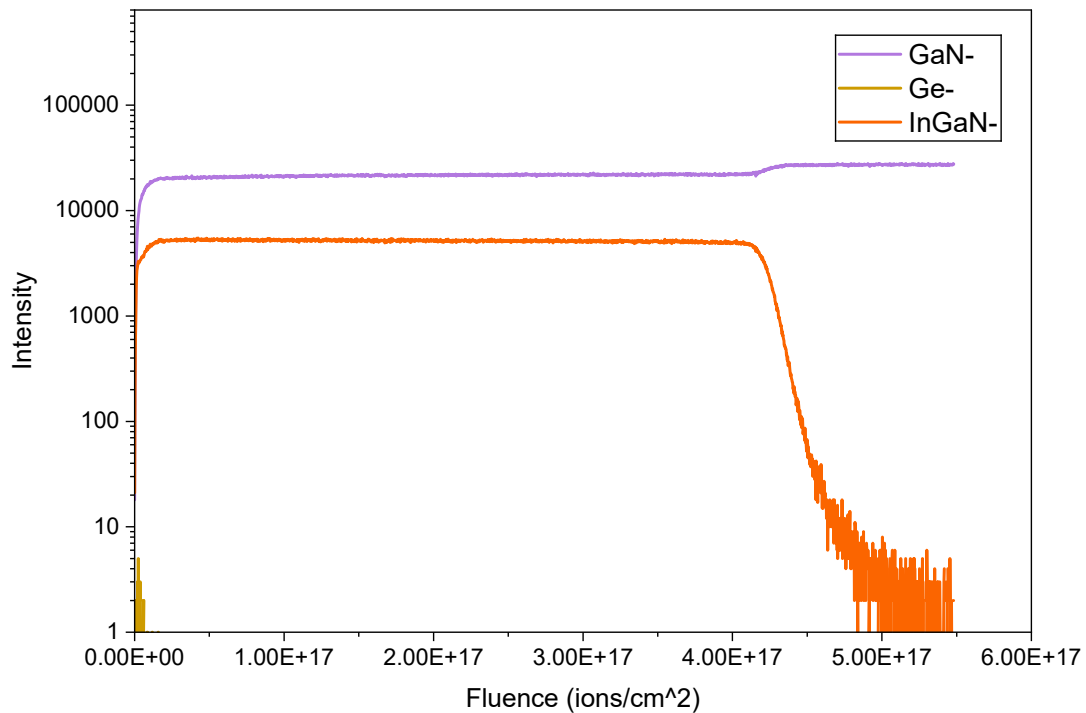


Figure 28: SIMS depth profiles of Ge, GaN and InGaN of undoped sample.

Figure 28 shows the SIMS profile of the reference sample, only a Ge signal at a background level is observed throughout the whole structure. This confirms that there is no unintentional Ge incorporation. The In-related signal maintains its uniformity within the InGaN region, but experiences a significant drop at the heterointerface to the GaN layer. This observation indicates the presence of good compositional homogeneity and a sudden layer transition. This sample serves as the baseline for evaluating intentional Ge incorporation.

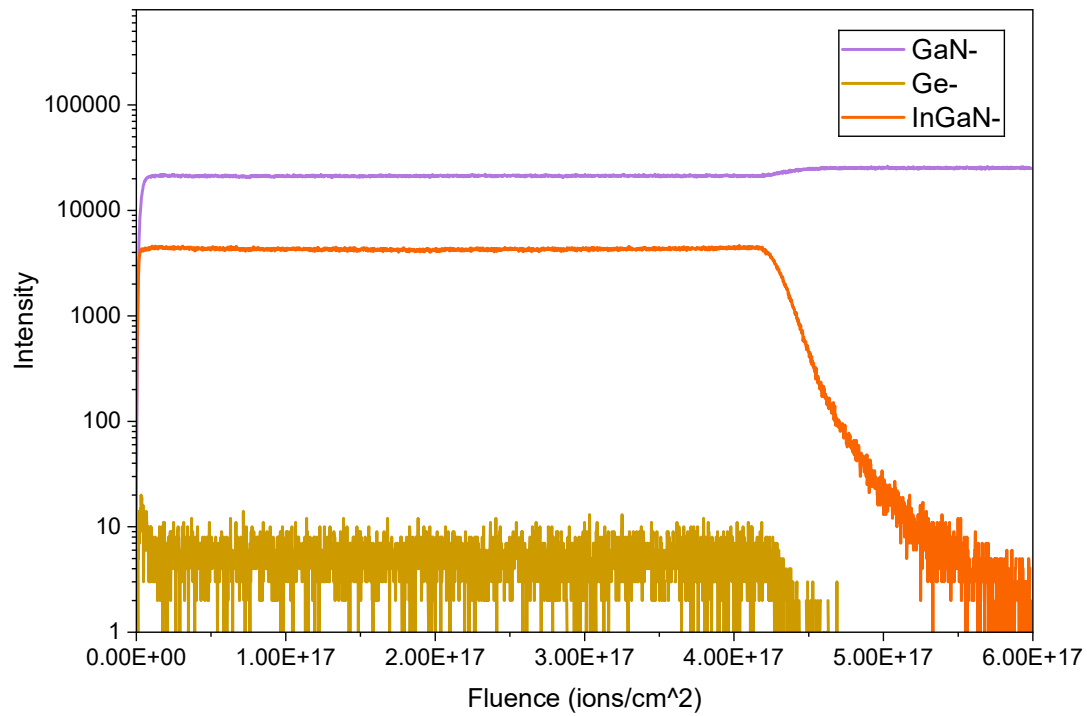


Figure 29: SIMS depth profiles of Ge, GaN and Ge-doped InGaN sample grown at 850 °C.

The SIMS profile of the Ge-doped sample grown at 850 °C indicates a clear Ge incorporation throughout the InGaN layer. The Ge intensity shows a uniform distribution across the active region, suggesting consistent dopant incorporation during growth. The interface between the InGaN and GaN layers retains an abrupt transition, with minimal tailing of the Ge signal into the underneath layer. The dopant appears to be firmly contained within the intended area, indicating effective and consistent incorporation at this growth temperature.

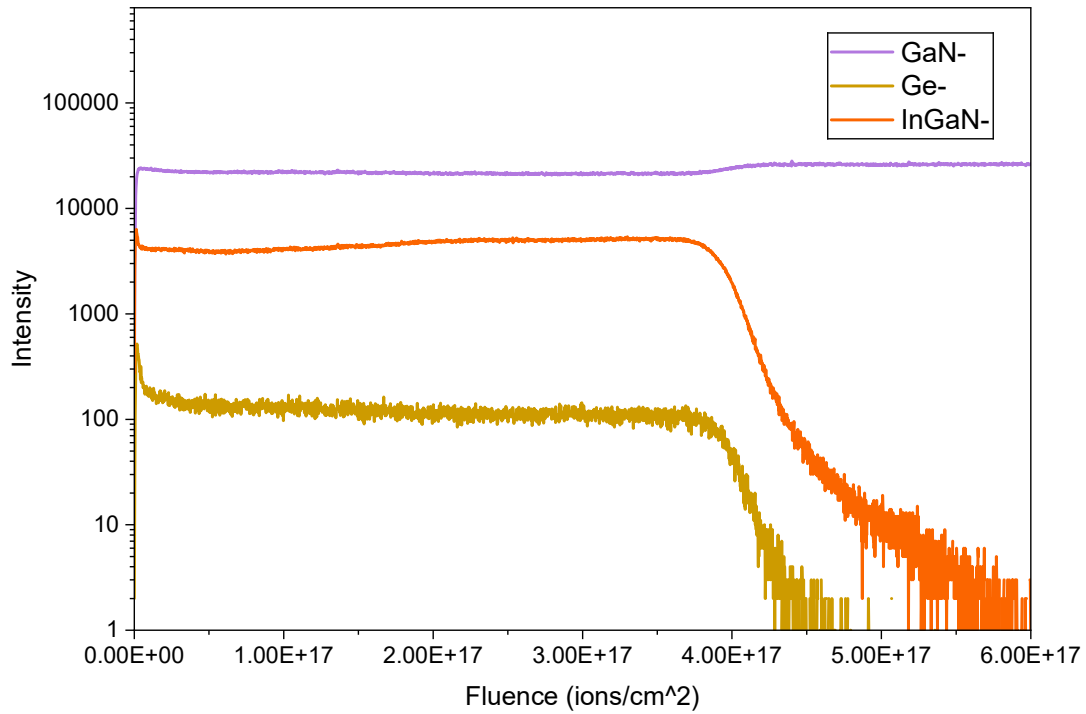


Figure 30: SIMS depth profiles of Ge, GaN and InGaN of 950 °C Ge-doped InGaN sample.

As shown in figure 30, a distinct behavior is exhibited by the corrected 950 °C sample relative to the 850 °C case. The Ge signal is by a factor of 10 higher in the InGaN region compared to the reference sample grown at 850 °C, which confirms that the dopant was successfully incorporated. The Ge intensity stays about the same across the InGaN layer, showing that the incorporation is uniform. However, small changes in the matrix signals are seen near the interface. A sharp transition is shown by the In-related signal at a fluence of approximately 4×10^{17} ions/cm², the Ga signal increases correspondingly in the GaN region, confirming a well-defined heterointerface. Slight interface broadening is observed in comparison to the 850 °C sample, indicating enhanced dopant mobility and interface diffusion at elevated growth temperatures.

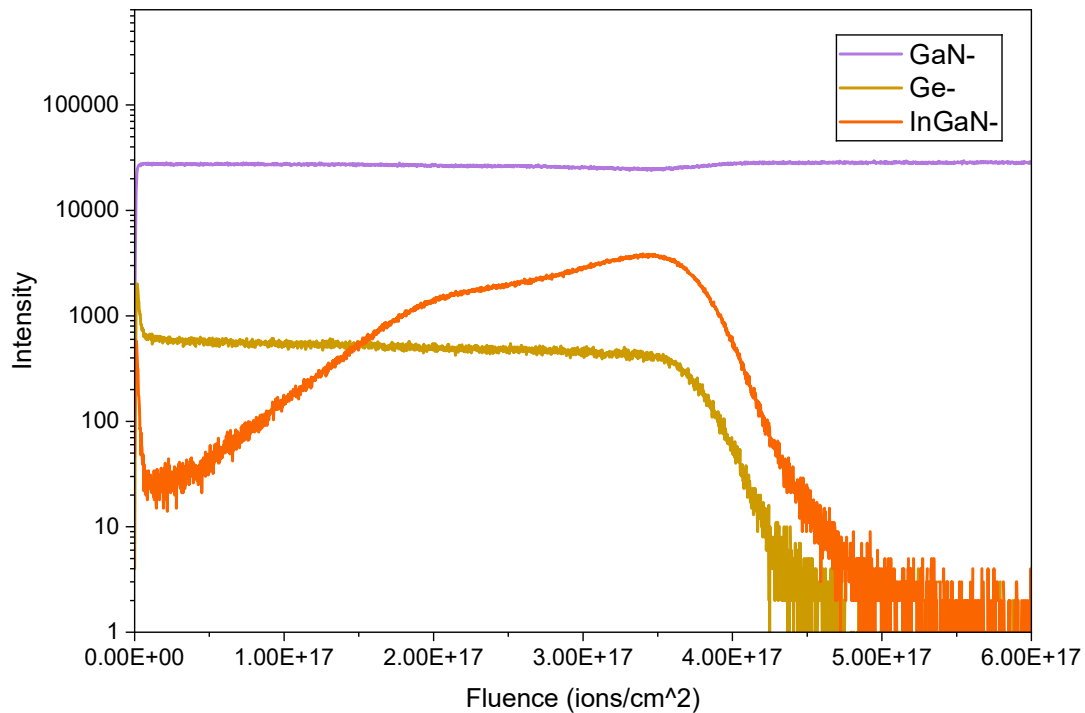


Figure 31: SIMS depth profiles of Ge, GaN and InGaN of 1000 °C grown Ge-doped InGaN sample.

Finally, the sample grown at 1000 °C displays considerably modified incorporation properties. The *In*-content shows inhomogeneities as shown in Figure 31. The transition in the interface is more extensive, and the tailing of the Ge signal beyond the desired doping region is more noticeable. These characteristics suggest *In* diffusion and potential surface segregation during the growth process. At this high growth temperature, enhanced atom diffusivity and thermally triggered diffusion processes probably facilitate *In* redistribution. In addition, the absence of abruptness at the InGaN/GaN junction indicates that 1000 °C surpasses the ideal thermal window for regulated Ge incorporation to the (In,Ga)N material system.

3.5 Electrochemical Characterization

3.5.1 Open Circuit Potential (OCP)

Initially, the undoped c-InGaN sample as shown in fig 32 (a) sample shows an unstable open circuit potential (OCP) with small oscillations during the early stages of the measurement. This indicates surface equilibration with the electrolyte and the formation of the electrical double layer. Before stabilizing at a value of approximately -0.25 to -0.27 V, a substantial negative shift in OCP is observed. This behavior is

indicative of undoped semiconductors, where the small number of free carriers leads to notable band bending and sensitivity to surface states. The negative steady-state OCP indicates the intrinsic semiconducting behavior of the undoped c-InGaN and suggests limited charge screening at the semiconductor-electrolyte interface.

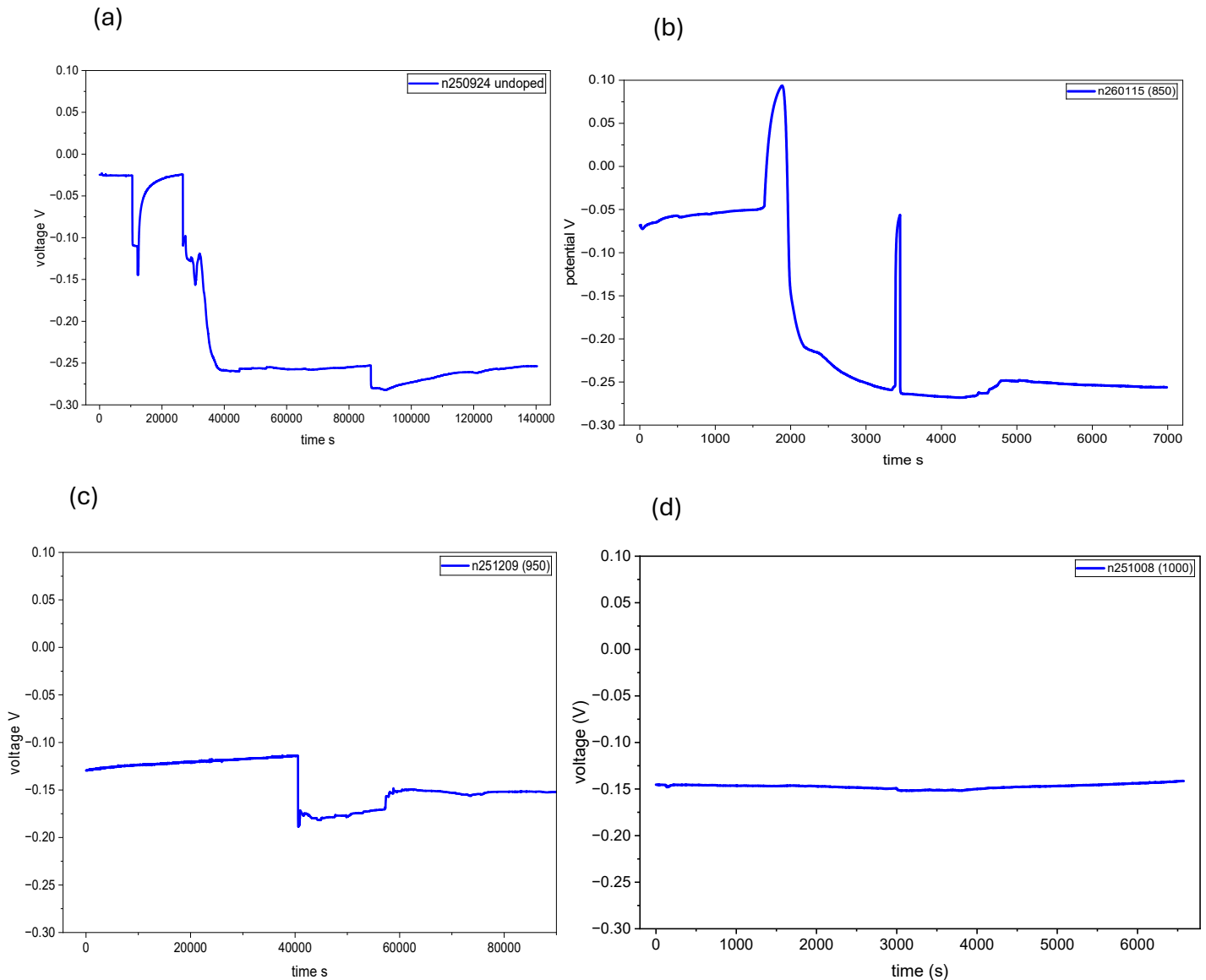


Fig 32: Open circuit evolution of (a) undoped and Ge-doped samples measured as a function of time. The Ge-doped samples were grown at (b) 850°C, (c) 950°C and (d) 1000°C.

On the other hand, the Ge-doped c-InGaN sample that was grown at 850 °C displays a distinctly disparate OCP profile as shown in figure 32 (b). The preliminary OCP of Ge-doped InGaN sample grown at 850 °C is more favorable in comparison to the undoped specimen, reaching a steady state around -0.25 V but reaches equilibrium in less time compared to undoped sample. Higher carrier density shifts the fermi level and change

the band bending at the interface, lowering the equilibrium potential. The small changes seen during stabilization may be due to some activation of the Ge and the presence of defects on the surface.

The 950°C-grown Ge-doped sample exhibited stable and reproducible OCP behavior. The transient region is followed by a rapid stabilization of the OCP, and a steady-state value close to -0.15 V is reached. This value is more positive to and Figure 32 (c) is slightly more stable than, the 850 °C-doped sample. Higher growth temperatures may result in a better Ge incorporation affecting OCP evolution. Making dopant activation better increases the number of free carriers, which leads to a decrease in surface band bending and better electronic equilibration at the semiconductor–electrolyte interface. The lack of significant variations suggests decreased surface trapping effects and a more consistent electronic configuration.

The Ge-doped sample grown at higher temperature of 1000°C exhibits the most stable OCP behaviour among all samples. It stabilizes rapidly after transient region and reaches a stable and equilibrium state at more positive OCP compared to other samples that is -0.140 V, revealing a further reduction of the surface band bending and more uniform electronic surface structure.

A clear trend among samples has been observed in terms of OCP positivity and stability. The progressive shift toward more positive value with Ge doping and increase growth temperature directly reflects the increase electron concentration and improved dopant activation. The results indicate the tuning of the electronic properties of c-InGaN by altering the carrier density due to doping.

3.5.2 Cyclic Voltammetry (CV)

The CV measurements of the investigated (Ga,In)N thin films with and without illumination as shown in Figure 33. The undoped sample (a) and (b) Ge-doped samples grown at 850 °C (Figure 33A) show a relatively elevated anodic current density with and without illumination. However, under illumination their cyclic voltammograms demonstrate instability. This is evidenced by considerable variation from scan to scan and the wide disparity of the photocurrent. The elevated photocurrent detected for these thin films is, thus, improbable to stem exclusively from effective photogenerated charge carrier extraction. Instead, the first CV is attributed to surface activation, double-layer charging, and trap charging. Oxygen evolution begins with illumination,

and bubbles adhere to the surface. These effects can artificially inflate the measured current and compromise electrochemical stability and reproducibility.

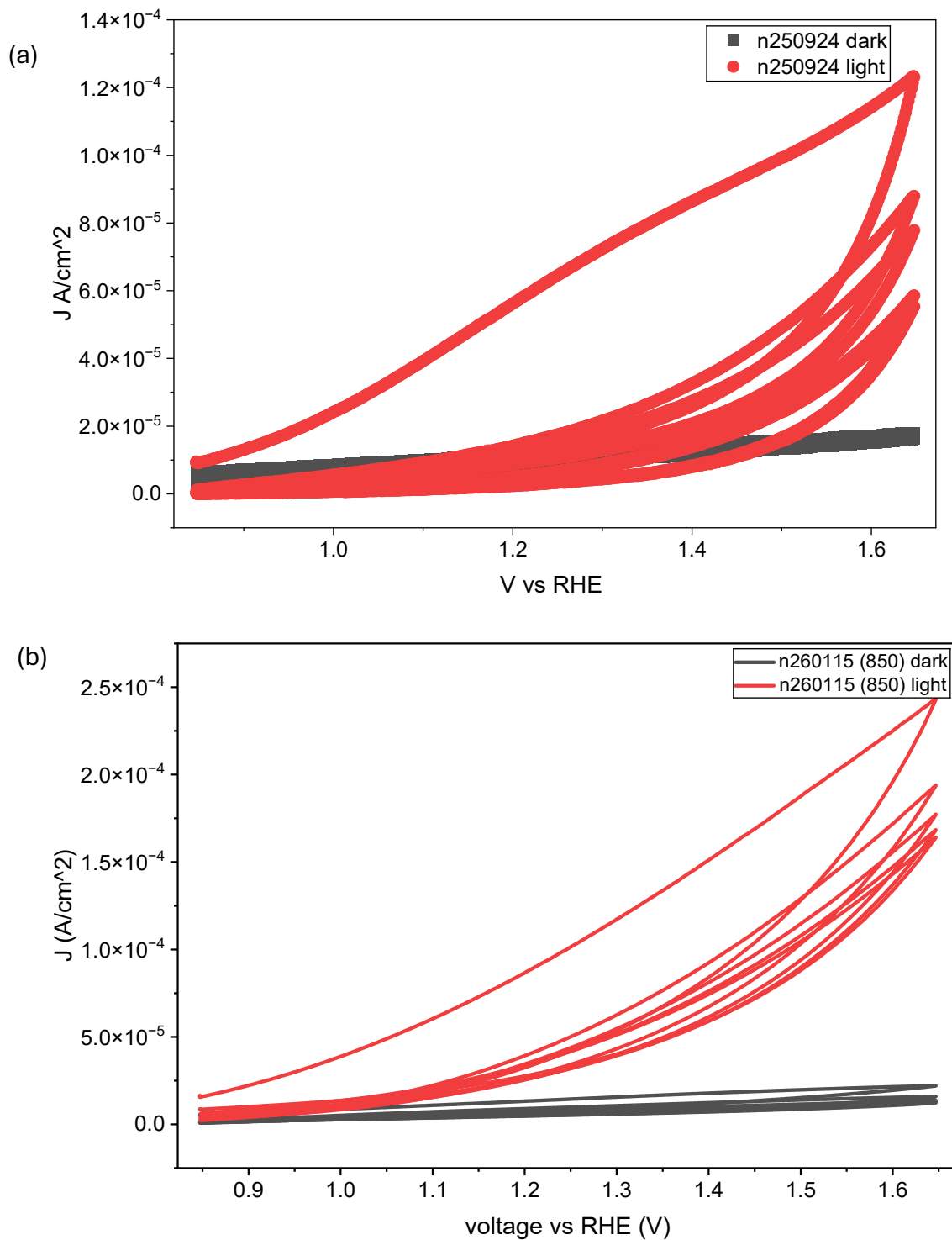
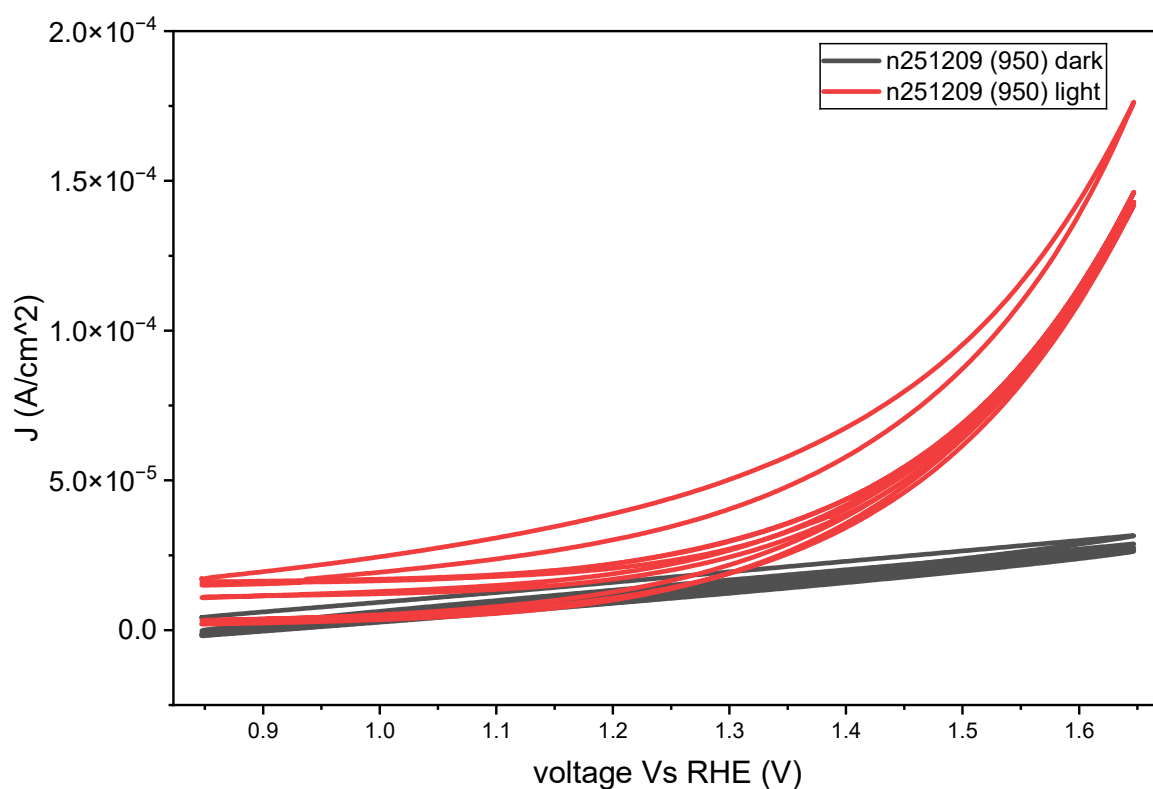


Figure 33 (A) The photoelectrochemical J-V characteristic curves of (a) undoped InGaN and (b) Ge-doped InGaN grown at 850 °C electrodes, fabricated at varying doping temperatures under both dark and illuminated conditions.

The For the Ge doped thin films grown at 950 °C (c) and 1000 °C (d) (Figure 33B), there is a notable improvement in the stability and reproducibility of the illuminated J–V curves, though there is a decrease in absolute current density, i.e., while the thin film grown at 950 °C shows a photocurrent of $2 \times 10^{-4} A$, the photocurrent is reduced to $5 \times 10^{-5} A$ for the thin film grown at 1000 °C. The closer alignment of repeated scans and decreased hysteresis suggest enhanced material uniformity, and less corrosion. This suggests that the growth at higher temperature results in a more compact and chemically stable film.



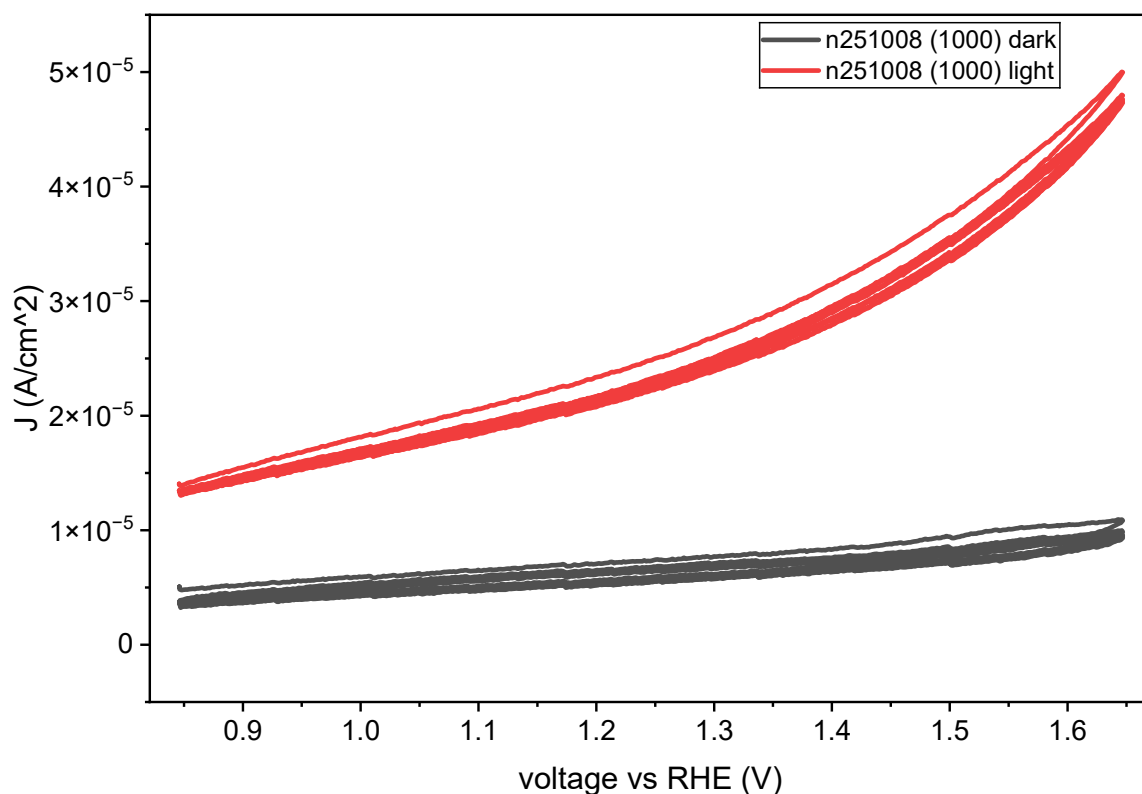


Figure 33 (B): The photoelectrochemical J-V characteristic curves of (c) Ge-doped InGaN grown at 950 °C and (d) Ge-doped InGaN grown at 1000 °C photoanodes, under both dark and illuminated conditions.

The most reliable photoelectrochemical behavior is demonstrated by the sample grown at 1000 °C (d), which is characterized by a consistent separation between dark and illuminated currents over the full potential range. The photocurrent magnitude is lower than that of the 850 °C or undoped sample, but its stability indicates that the measured current is primarily governed by intrinsic photogenerated carrier transport and likely not by photocorrosion. From a photoelectrochemical standpoint, such stability is of high importance for uninterrupted operation and serves as a more salient metric of material efficiency than elevated but erratic current densities.

The results overall highlight a clear photocurrent magnitude trade-off and electrochemical stability. Lower the growth temperature of the thin films and the Ge doping concentration yield higher currents. However, thin films suffer from instability. On the other hand, higher Ge doping achieved at higher growth temperatures especially 1000 °C, leading to better photoelectrochemical efficiency.

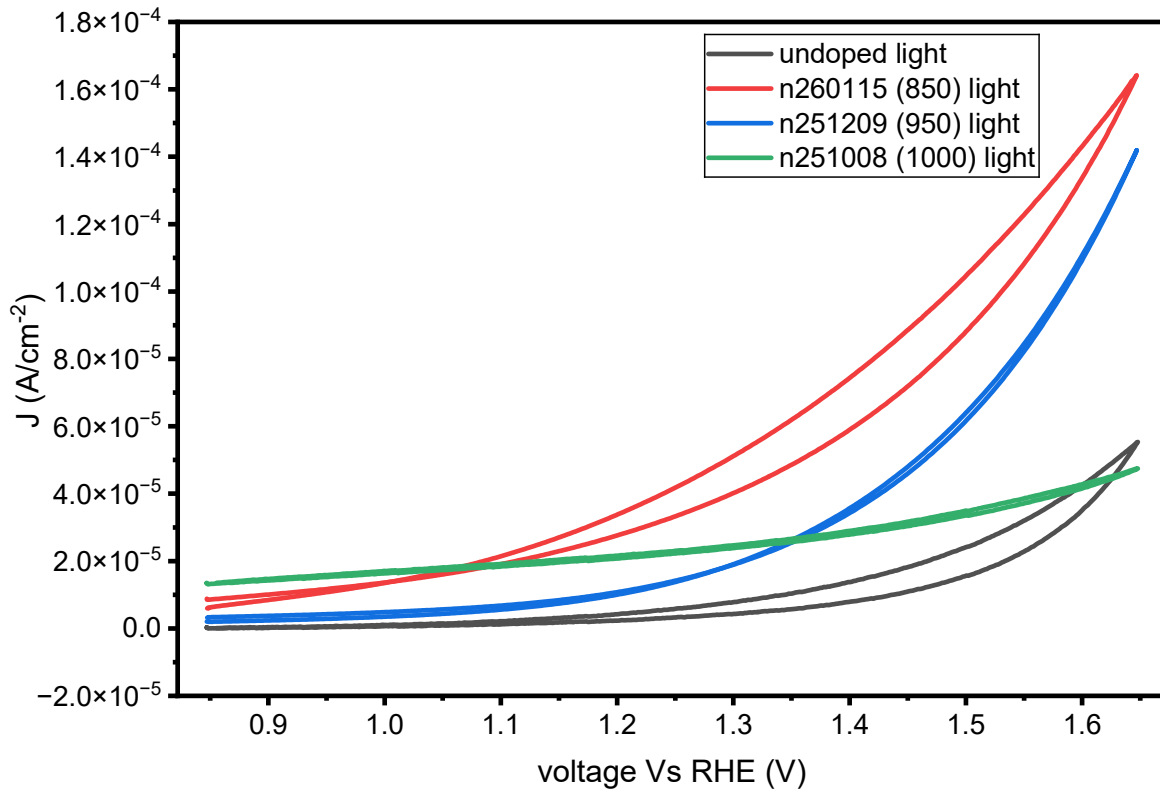


Fig 34: Comparison of the fifth cyclic voltammetry (CV) cycle of all illuminated samples measured, permitting direct analysis of their stabilized electrochemical response after repeated potential cycling.

The first few tests showed that the thin films were not necessarily stable showing different photocurrent each time the CV measurement was done. By the fifth cycle, however, all samples exhibited a notable reduction in current magnitude and a more consistent response as shown in Figure 34. This decline in photocurrent indicates that a substantial fraction of the initially high current originated from transient surface processes, which are suppressed upon repeated cycling.

The undoped sample and 850 °C-grown Ge-doped sample have a high photocurrent density but show a big hysteresis and small overlap between the cycles. Despite reduction in donor density of Ge-doped InGaN grown at 850 °C (see previously discussed Table 4) compared to undoped sample, a higher current density is still

maintained by the 850 °C Ge-doped sample than by the undoped electrode, suggesting that carrier density is enhanced by Ge incorporation at this temperature.

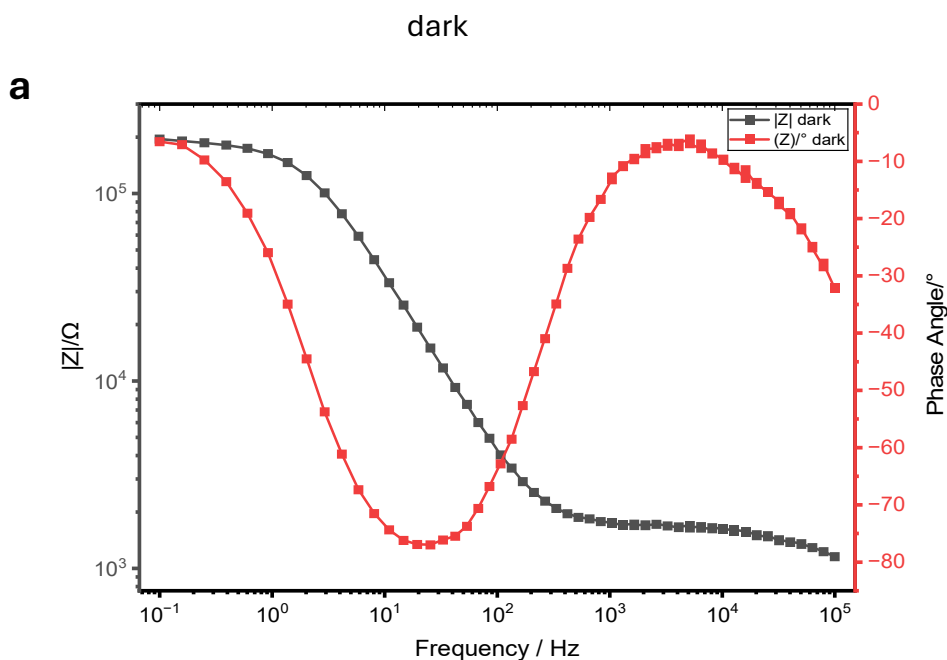
The Ge-doped grown samples at 950 °C and 1000 °C show opposite trends. While their initial CVs showed lower absolute photocurrent compared to the sample grown at 850 °C, their fifth-cycle CVs shows little changes, highlighting superior electrochemical stability. Specifically, Ge-doped thin film grown at 1000 °C maintains a steady, continuous rise in current density with applied potential and displays the least variation between initial and subsequent cycles. This suggests that the photocurrent is primarily driven by intrinsic photogenerated carrier transport, rather than by unstable surface-mediated contributions.

A comparison of all samples reveals that the fifth-cycle CV clearly shows a convergence toward stable behavior. Although the sample grown at 850 °C initially appears superior based on raw photocurrent, the reduction of current upon cycling highlights the importance of defect-driven processes in the initial CVs. The conclusions drawn from the earlier CV measurements are corroborated by the fifth-cycle CV analysis. Superior photoelectrode performance is not necessarily reflected by high initial photocurrents. The Ge-doped grown at 1000 °C reveals a stable and reproducible current over repeated cycling and thus is a representative of optimized doping in the (Ga,In)N thin films.

3.5.3 Electrochemical Impedance Spectroscopy (EIS)

(In,Ga)N film

The Bode impedance magnitude and phase angle plot under dark conditions and with an applied bias of 0.8 V vs RHE is shown in Fig 35 (a). The impedance magnitude $|Z|$ is high in the low-frequency area ($\sim 10^5 \Omega$), and then it decreases with increasing frequency, lowering to about $10^3 \Omega$ at high frequencies. This shows that, with an applied potential of 800 mV, charge transfer at low frequencies is mostly affected by interfacial charge transfer resistance, showing intrinsic electrochemical reaction kinetics, while the high-frequency behavior is mainly controlled by the series resistance of the film and contacts. The phase angle shows a clear minimum in the middle of the frequency range (approximately 10–100 Hz)⁵⁹. This indicates a significant capacitive element as angle reaches closer to 90° , which is contributed by the space-charge region and the trap-mediated charge storage.



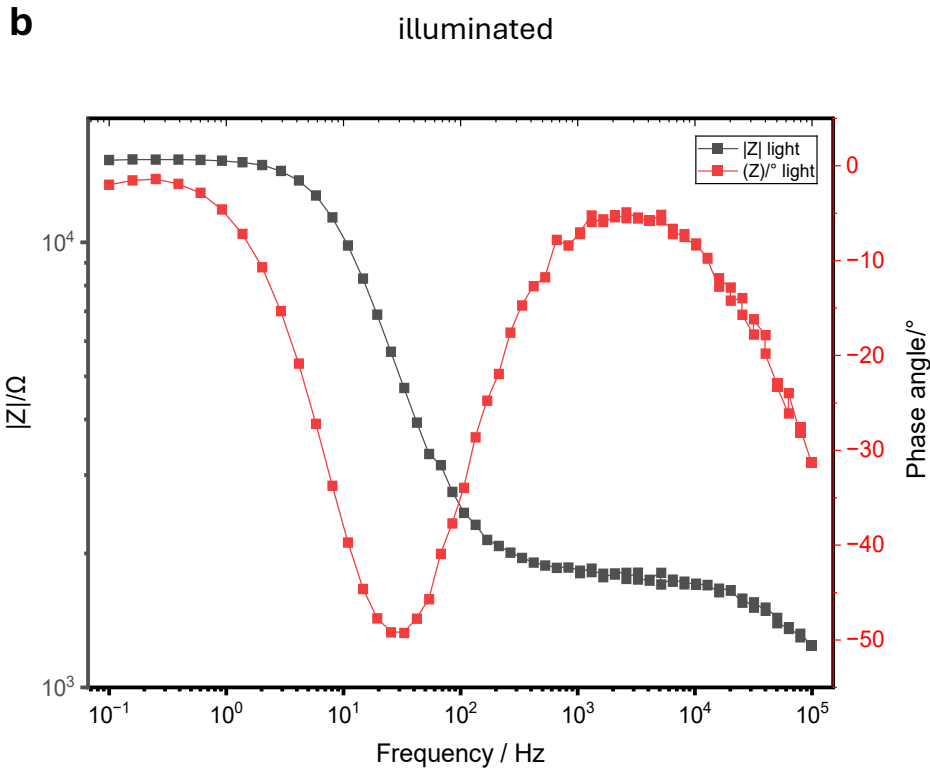


Fig 35 (a) shows the Bode impedance magnitude and phase angle plots of the c-InGaN sample obtained under dark and (b) illuminated conditions at an applied bias of 800 mV vs RHE.

A remarkable decrease in $|Z|$ is noticed across the entire frequency range when illuminated at a consistent bias voltage of 800 mV vs RHE as shown in Fig 35 (b). The most significant change is observed at low and intermediate frequencies. This decline is indicative of enhanced conductivity resulting from the presence of photogenerated carriers, which facilitate charge transport under conditions of forward bias. The phase angle minimum shifts toward higher frequencies under illumination because there is less charge transfer resistance due to more photogenerated carriers. According to the characteristic relaxation frequency ($f = 1/2\pi R_{ct}C$), faster interfacial charge transfer dynamics are caused by a decrease in R_{ct} . Furthermore, a reduced negative phase angle suggests a decrease in capacitive dominance and an enhancement in charge separation efficiency at the semiconductor–electrolyte interface.

Nyquist plot

The lack of illumination makes sure that the studied electrical response comes only from the transport of charge within the material and the surface processes, without the contribution of carriers made by light. The Nyquist spectra show one small semicircle represented as Process 1 at high frequencies showing small τ (time constant) representing bulk resistance, and a large semicircle which indicates a process termed as Process 2 at lower and intermediate frequencies showing behaviour of semiconductor/electrolyte interface⁵⁹. Process 2 is used to plot Mott-schottky data and further used to determine donor density and flat band potential. This interface is dominated by charge-transfer resistance. It is in parallel with a capacitive element. There is no Warburg-type linear tail at low frequencies, no diffusion in electrolyte necessary as water is always present.

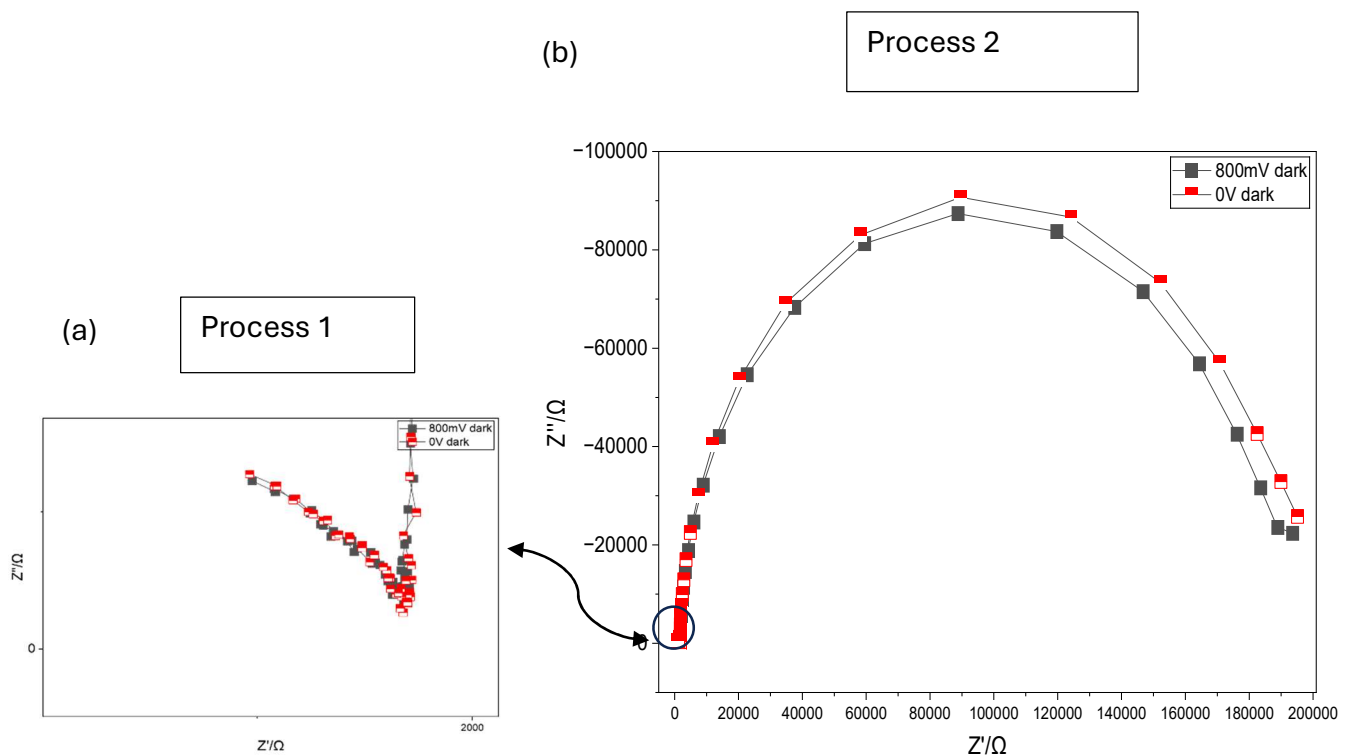


Figure 36 (a) process at high frequency (small τ) and (b) process at intermediate to low frequency (big τ) of undoped InGaN sample's Nyquist plots (Z'' vs. Z') under dark conditions at 0 V and 800 mV.

The semicircle diameter at 0 V is larger compared to 800 mV, which reflects the higher interfacial resistance present at lower bias voltages. This behavior is due to a wider

depletion layer and reduced electron availability in the absence of an external field to assist carrier transport. The reduced semicircle diameter at 800 mV suggests enhanced interfacial charge transfer and lower interfacial resistance compared to 0V, which is consistent with the narrowing of the depletion layer induced by the applied bias. The curve indicates non-ideal capacitive behavior, which is often linked to surface roughness, interface states, and chemical inhomogeneity in InGaN films.

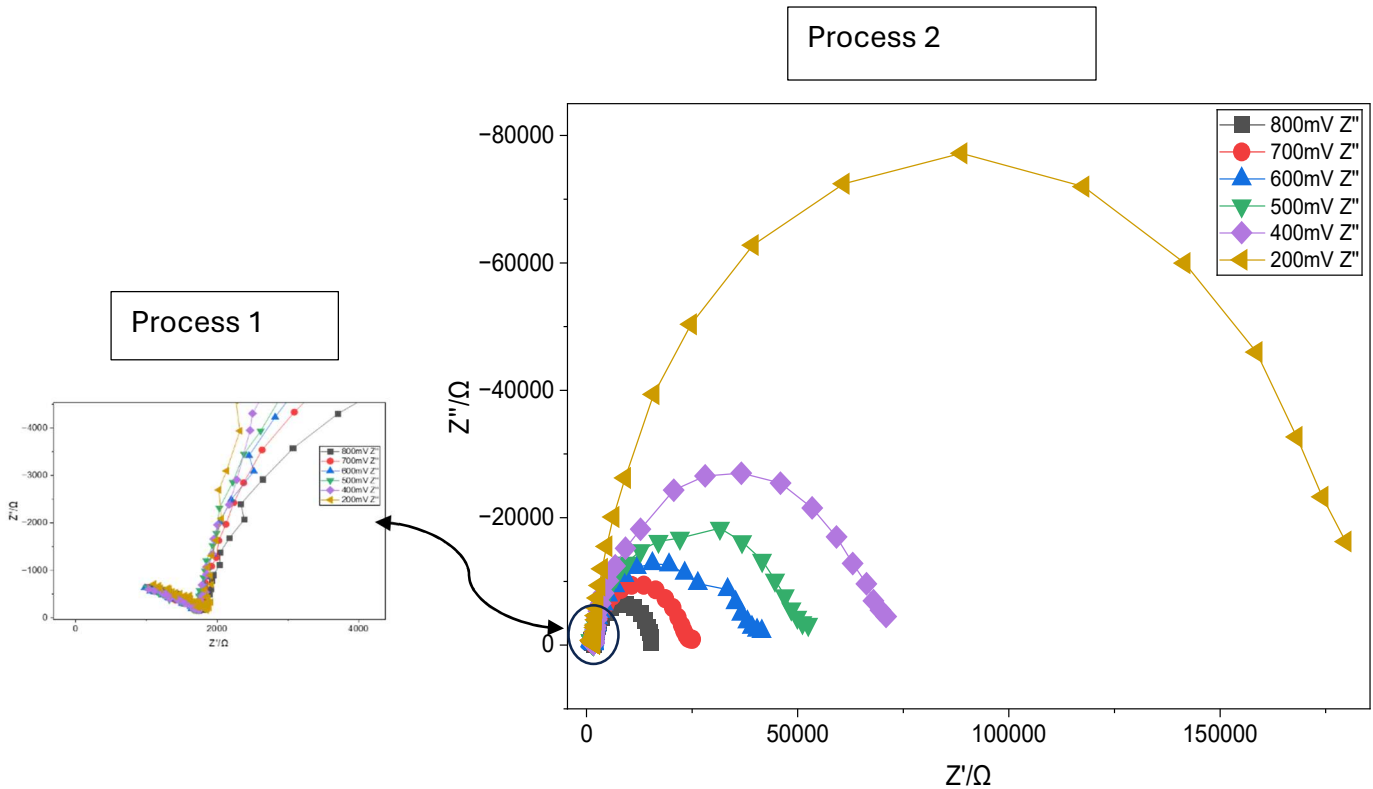


Figure 37: the Nyquist plot under UV illumination for varying applied bias voltages showing two distinct processes, (a) small semicircle (short timescale) (b) large semicircle (long timescale).

Fig 37(a) shows a small semicircle representing processes taking place at higher frequencies. The high-frequency region is related to fast processes at the interface, such as semiconductor space charge capacitance and series resistance effect⁶⁰. Fig 37 (b) shows a bigger semicircle, low and intermediate frequency region. At lower or intermediate frequencies, slower charge transfer and recombination phenomena are dominant. When exposed to UV light, the Nyquist plots of the impedance at higher applied biases (800–600 mV) display smaller and more depressed semicircular arcs in the low-impedance region than those at lower bias (200mV). The reduced diameter of

the semicircle shows a lower charge transfer resistance, which can be explained by the creation of photocarriers when stimulated by UV light.

There is a noticeable increase in the semicircle diameter with a decrease in applied bias from 500 mV to 200 mV, indicating a progressive increase in charge transfer resistance. Even though there is UV light, a lower applied bias limits how well photogenerated electron–hole pairs can be separated and transported as the band bending at the interface is reduced the sense that less is the band bending, less effective will be the charge separation. The substantial semicircle detected at 200 mV indicates that interfacial charge transfer persists as the prevailing process governing the impedance response within this bias regime.

The Nyquist spectra's evolution under UV illumination shows that undoped InGaN has strong bias-dependent photoelectrochemical behavior. The charge transfer resistance is reduced when the applied bias is increased under illumination. This facilitates more optimal utilization of photogenerated carriers and better interfacial charge transport⁶¹.

Equivalent circuit Model:

The equivalent circuit that best describes the impedance response of the undoped InGaN sample is made up of two $R||CPE$ circuit elements where R is the resistor connected parallel to the CPE stands for Constant Phase Element. This is a mathematical circuit element used in EIS to describe non-capacitive ideal behavior and both the circuits are connected in series ($R || CPE$) – ($R || CPE$)

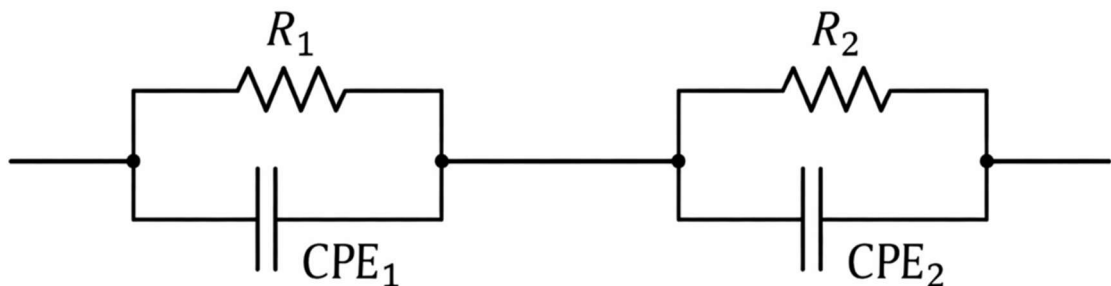


Fig 38: Equivalent circuit model used to describe the impedance response of InGaN samples.

The high-frequency (R || CPE) element is linked to contributions from the bulk or near-surface, as well as to effects related to contact.

The low-frequency (R || CPE) element corresponds to the space-charge region. It also corresponds to charge-transfer processes. These processes take place at the semiconductor electrolyte interface including space-charge region and electrochemical double layer in the electrolyte.⁶²

Mott-Schottky Analysis

Mott–Schottky analysis was used to study the properties of the InGaN thin films, incorporating the semiconductor type, the flat-band potential, and donor density. The capacitance determined for Mott–Schottky analysis was derived from the low-frequency semicircle of the fitted impedance spectra as shown in Table 3. The low frequency region corresponds to the predominant interfacial process within the equivalent circuit model under dark conditions and graphed as the inverse square of the space-charge capacitance ($1/C^2$) as a function of the applied potential.

Voltage vs RHE (V)	Resistance, R_2 (Ω)	CPE constant, $Q_2/(\Omega^{-1})$	α_2	$C_2(F)$ $(Q_2 R_2^{(1-\alpha_2)})^{1/\alpha_2}$	$1/C_2^2$
1.647	186115.63681	4.7522E-7	0.977	3.4187E-7	8.55616E12
1.547	188430.08207	4.63743E-7	0.985	3.69014E-7	7.3437E12
1.447	188313.27594	4.74301E-7	0.985	3.83807E-7	6.78852E12
1.347	188598.07903	4.98723E-7	0.984	3.95048E-7	6.40767E12
1.247	186997.60354	5.2737E-7	0.983	4.15331E-7	5.7971E12
1.047	185560.18653	5.75915E-7	0.987	4.79167E-7	4.35537E12
0.847	190209.27258	6.71205E-7	0.987	5.56912E-7	3.22424E12

Table 3 Impedance parameters of undoped InGaN sample calculated using RelaxIS software.

The constant phase element (CPE) is determined by Q and α . If $\alpha = 1$, the CPE will equal the capacitance and behaves as an ideal capacitor. If $\alpha < 1$, it behaves like a real capacitor.

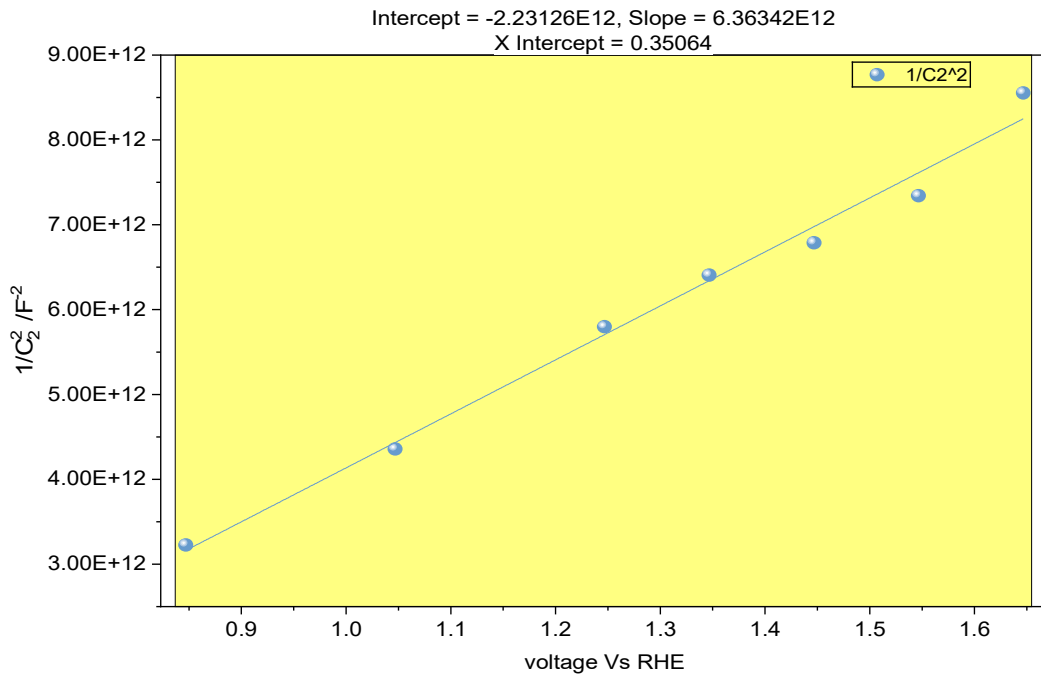


Fig 39: The Mott-Schottky plot for the undoped (In,Ga)N measured in an electrolyte with a pH of 11. The positive slope indicates n-type semiconducting behavior.

The Mott-Schottky relationship for n-type semiconductor is given as:

$$\frac{1}{C^2} = \frac{2}{\epsilon\epsilon_0 A^2 N_D} \left(E - E_{fb} - \frac{kT}{e} \right) \quad (36)$$

Flat band Potential

The flat-band potential E_{fb} obtained by extrapolating the linear region to the potential axis. It yielded a value of 0.35 V vs. RHE.

Donor Density

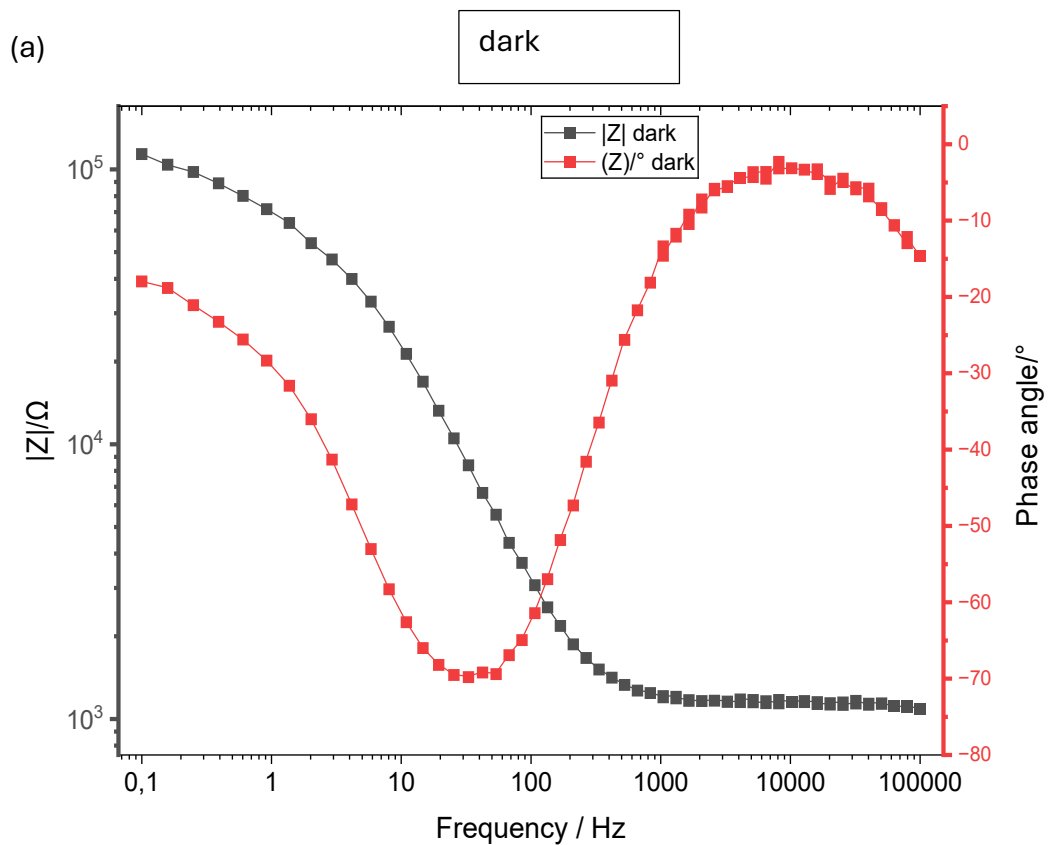
The donor density was calculated using the same relation:

$$N_D = \frac{2}{e\epsilon\epsilon_0 mA^2} \quad (37)$$

$$N_D = 2.57 \times 10^{19} \text{cm}^{-3} \quad (38)$$

Ge doped (In,Ga)N film grown at 850 °C

The Bode plot of Ge doped InGaN sample grown at 850 °C is shown in Fig. 40. Under dark conditions, there is a notable decrease in the low frequency $|Z|$ of the doped sample compared to the undoped sample, indicating decrease in the charge transfer resistance due to Ge incorporation. The impedance undergoes a gradual decline with increasing frequency, ultimately attaining a comparable high-frequency plateau ($\sim 10^3 \Omega$), thereby showing bulk and analogous series resistance. The phase angle minimum is still at about 50 Hz clearly observable, but it is shifted towards higher frequencies compared to the undoped sample. This suggests that the dielectric relaxation is faster and reduced.



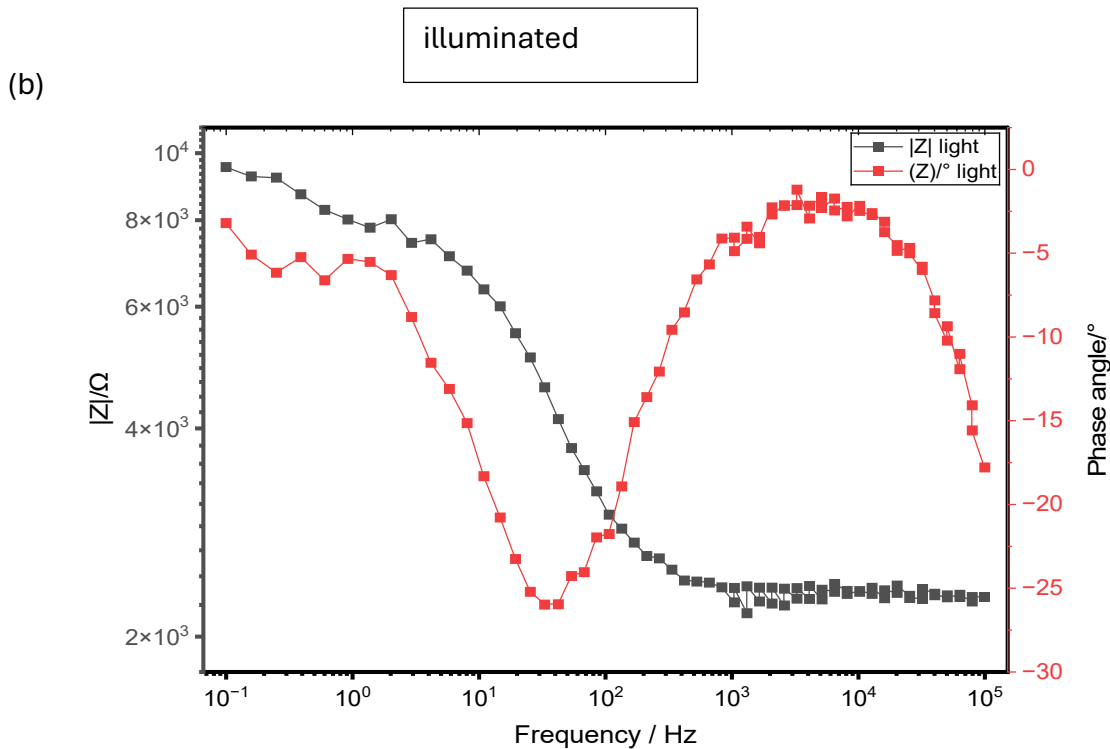


Figure 40: Bode plot of impedance response of Ge-doped InGaN grown at 850 °C under (a) dark and (b) illuminated condition at bias voltage of 800mV vs RHE.

Under illumination, $|Z|$ further decreases, especially in the low-frequency range. However, the impedance modulation between dark and light conditions is smaller than that of the undoped sample. This indicates that charge transport is increasingly dominated by doping-induced carriers rather than photo-generated ones. The results show that doping with germanium (Ge) at 850 °C effectively increases electrical conductivity while in the (In,Ga)N thin films maintaining a measurable photo-response.

Nyquist plot

The two distinct processes of the Ge-doped InGaN grown at 850 °C measured under dark conditions with an applied bias of 0 V and 800 mV is shown in Fig. 41. The Nyquist semicircle recorded at 800 mV, when compared to the 0 V condition, shows a reduced diameter. This indicates a decrease in interfacial resistance upon the application of bias. This is the normal change in the equilibrium due to bias, which results in a change of band bending and, thus, charge transfer at the interface, thereby enabling charge transfer across the Ge-doped InGaN/electrolyte interface in the absence of light.

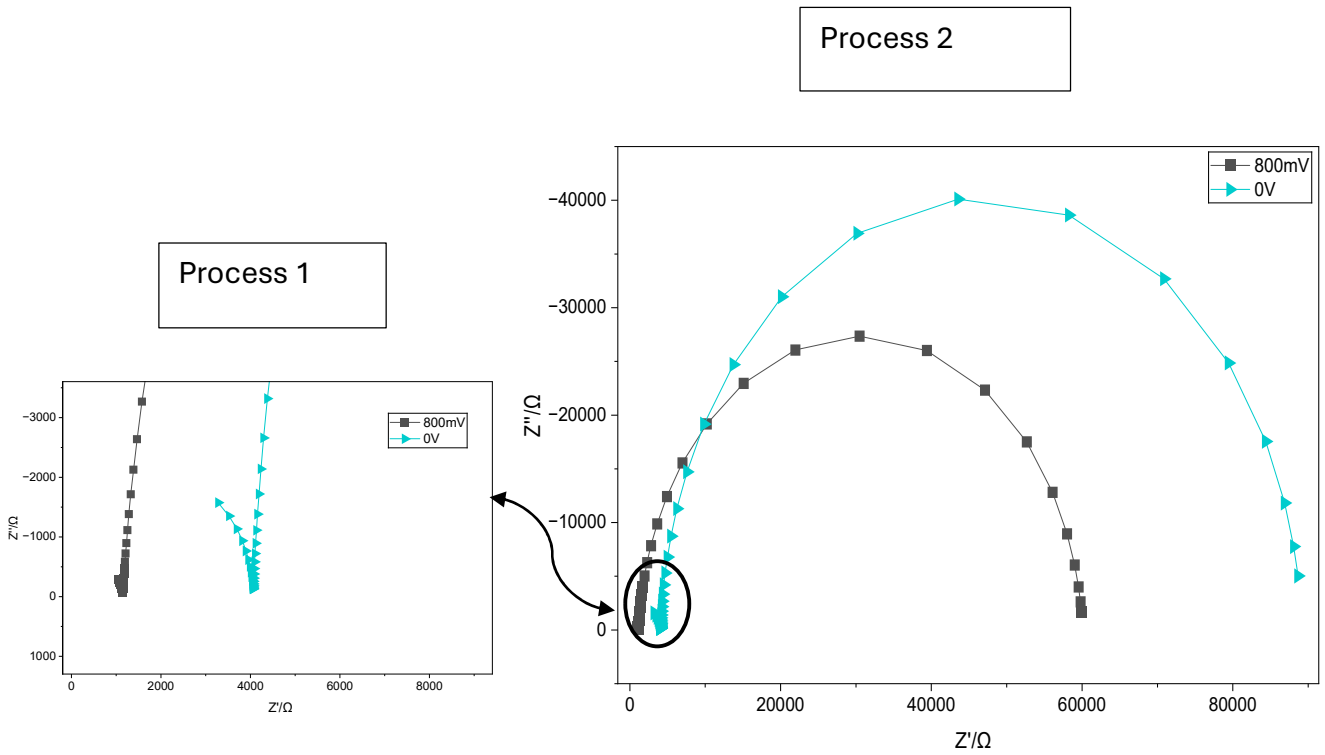


Figure 41: Nyquist plot of Ge-doped (In,Ga)N thin films grown at 850 °C under dark condition at 0V and 800mV.

The impedance measurements demonstrate the impact of Ge doping on the photo-induced charge transport and interfacial electrochemical response of InGaN thin films as shown in Fig. 42. The Ge-doped sample displays smaller semicircular arcs across all applied bias voltages when compared to undoped InGaN, revealing a substantial decrease in charge transfer resistance. This behavior is due to the incorporation of Ge donors in the (In,Ga)N, which increases the concentration of free electrons and improves electrical conductivity. Under UV illumination, the higher carrier density promotes the efficient transport of photogenerated electrons more effectively across the InGaN/electrode interface.

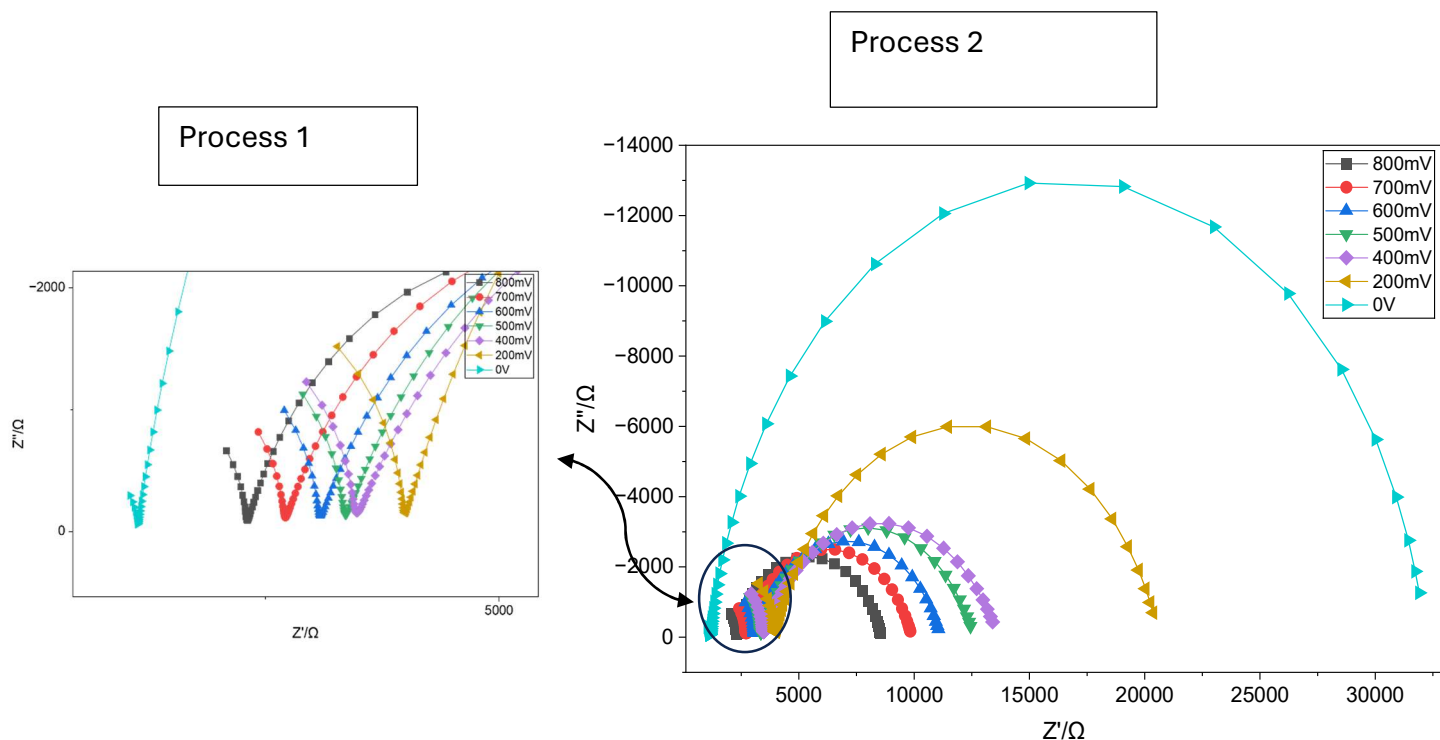


Figure 42: the Nyquist plot of the impedance of Ge-doped InGaN that was grown at 850 °C. The measured impedance was under UV illumination at applied bias voltages varying between 0 and 800 mV.

Mott-Schottky Analysis:

The Mott–Schottky plot of the Ge-doped InGaN sample, which was grown at 850 °C, is shown in the Figure 43. The values of capacitance have been extracted by using the constant phase element parameters i.e. Q and α of the equivalent circuit, which was fitted to the data as shown in Table 4. The capacitance measurements were taken under dark conditions.

Voltage vs RHE (V)	Resistance, R_2 (Ω)	CPE constant, $Q_2/(\Omega^{-1})$	α_2	$C_2(F)$ $(Q_2 R_2^{(1-\alpha_2)})^{1/\alpha_2}$	$1/C_2^2$
1.647	58976.11328	7.60003E-7	0.95215	3.74355E-7	7.13564E12
1.547	71113.29263	7.69375E-7	0.95312	3.84987E-7	6.74694E12
1.447	81421.72235	7.77163E-7	0.95491	3.99992E-7	6.25024E12
1.347	105478.33309	9.19951E-7	0.9445	4.0652E-7	6.05112E12

1.247	118855.89777	9.62899E-7	0.94105	4.04288E-7	6.11813E12
1.047	87867.49771	9.33068E-7	0.9646	5.60537E-7	3.18267E12
0.847	85224.19879	1.09245E-6	0.96333	6.47884E-7	2.38235E12

Table 4: shows the impedance parameters of Ge doped InGaN grown at 850 °C sample calculated using RelaxIS software.

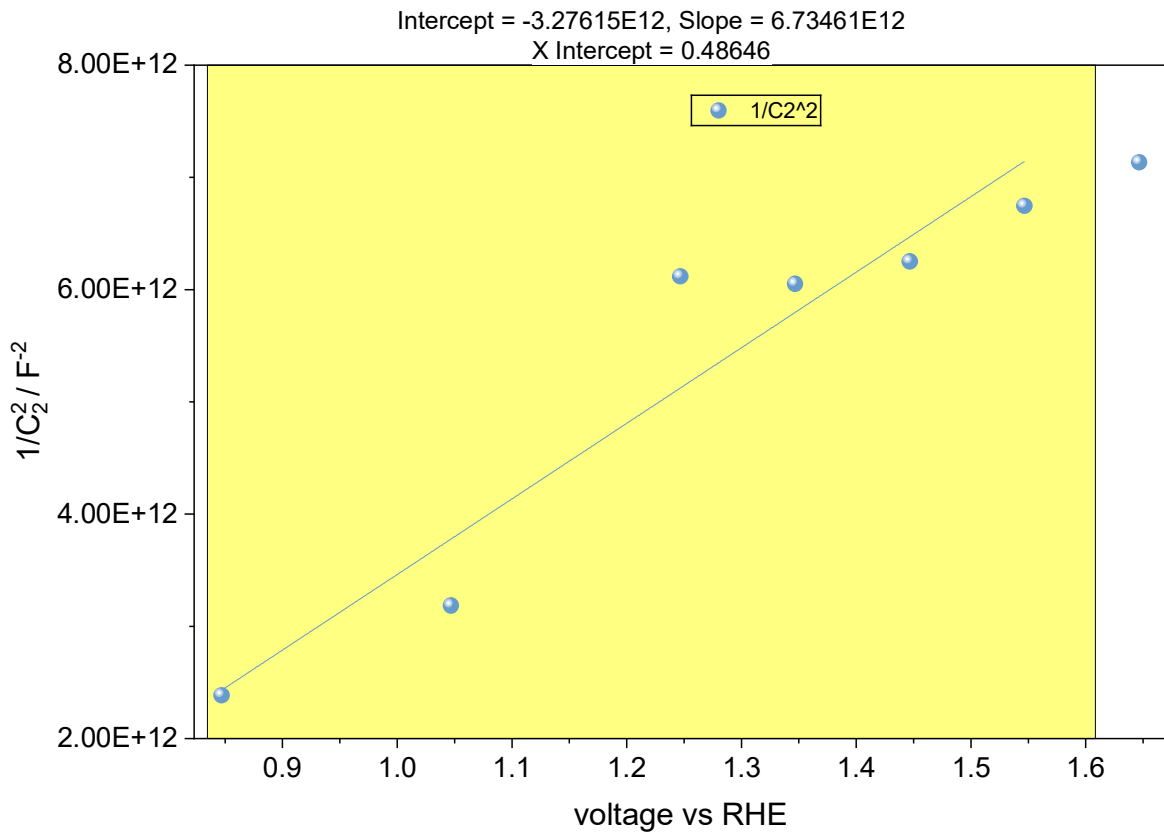


Figure 43: the Mott-Schottky plot of InGaN with doped Ge grown at 850 °C under dark condition.

The Mott–Schottky plot is shown in Figure 43. A linearity, although less evident as for the other examined cases, has been observed over the potential range, indicating a depletion layer formation at InGaN/electrolyte interface. The positive slope of the linear region confirms n-type conductivity, which is indicative of Ge acting as an active donor in the InGaN lattice. A comparison of the Mott–Schottky plot of the doped sample with that of the undoped sample exhibits successful inclusion of Ge during growth at 850 °C.

Flat band Potential

The flat band potential (V_{fb}) was determined from the x-intercept of the linear region of the Mott-Schottky plot that was observed under dark conditions. It yielded a value 0.48V.

Donor density

The donor density calculated like the undoped using the relation:

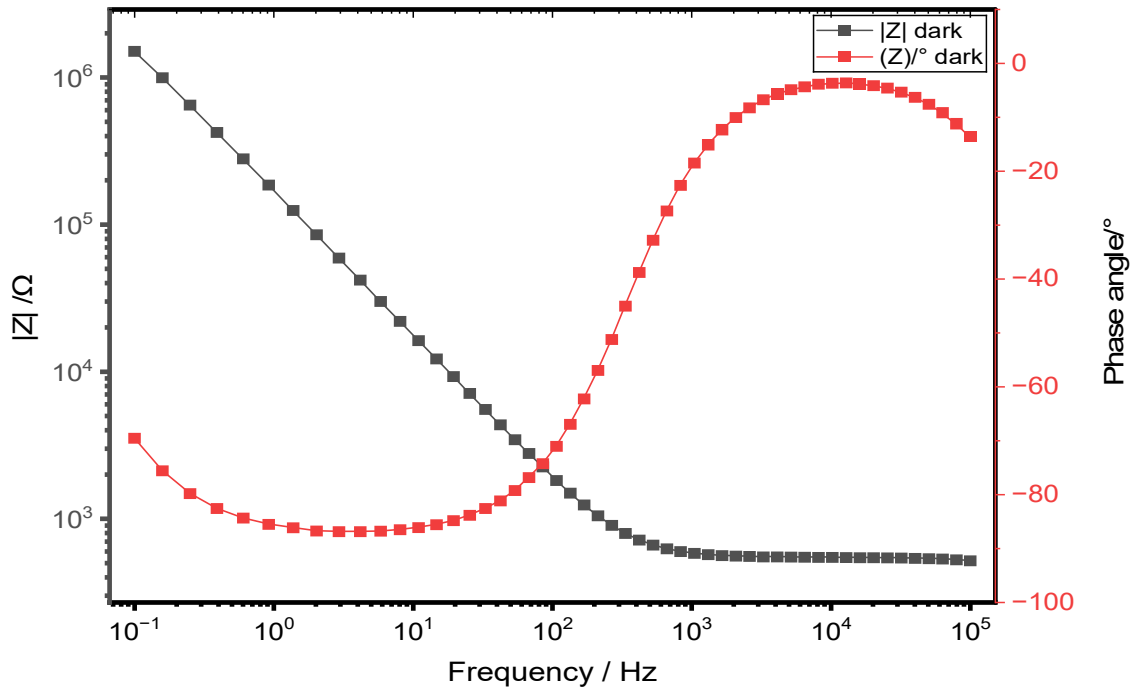
$$N_D = \frac{2}{e\epsilon_0 mA^2} \quad (39)$$

$$N_D = 2.5 \times 10^{19} cm^{-3} \quad (40)$$

Ge doped (In,Ga)N film grown at 950 °C

The Ge doped InGaN grown at 850 °C under dark condition exhibits impedance values at low frequencies (on the order of $\sim 10^6 \Omega$) as shown in Figure 44 (a), and a progressive decrease is seen with increase in frequency. This behavior signifies profound impediment to charge transfer at the semiconductor/electrolyte interface. The phase angle reaches values near -90° (slightly going beyond this value because of the sign convention and the non-ideal capacitive response), especially in the low-to-intermediate frequency range. An impedance response like this is typical for a mostly capacitive system, where the flow of current is mostly determined by the accumulation of charge within the space-charge region instead of by faradaic charge transfer. The wide-ranging phase ($\sim -90^\circ$) minimum detected in the low-frequency area indicates the double-layer capacitance is the dominant factor, and the charge transfer resistance is significant. Consequently, electron transfer is kinetically constrained. The high $|Z|$ and the fact that the capacitive behavior is almost ideal show that, when there's no illumination, the interface acts like a junction that blocks a lot and limits how carriers are transported.

a)



b)

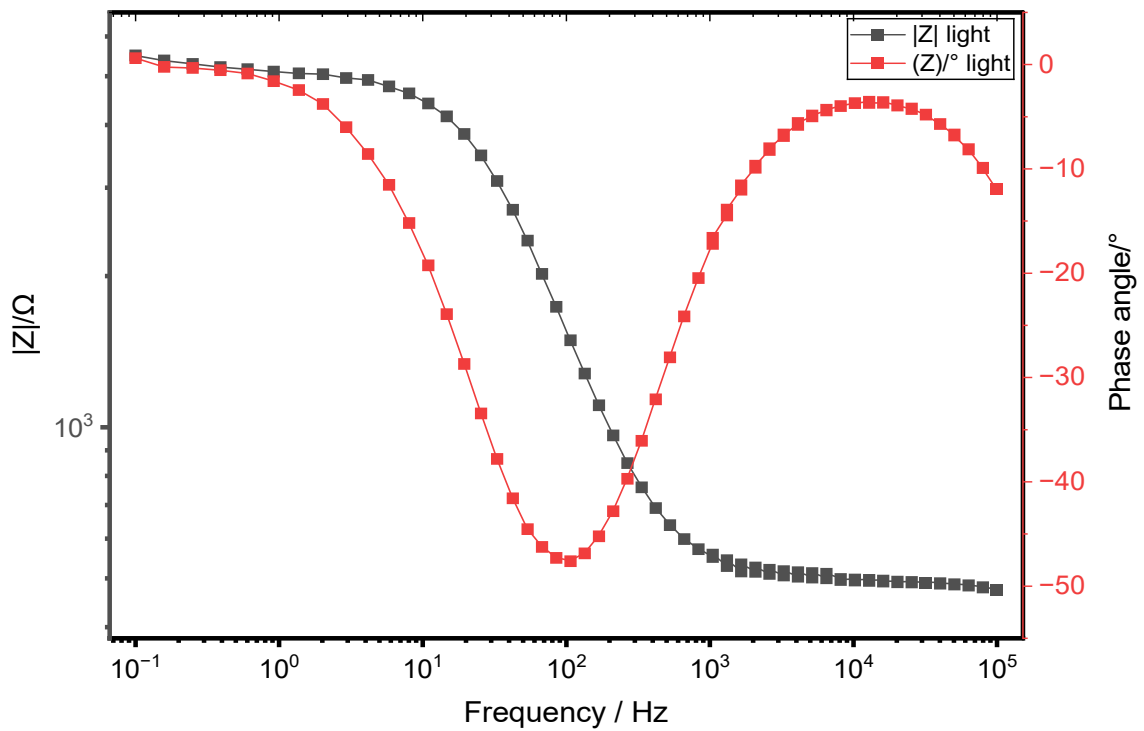


Figure 44: Impedance response of the Ge-doped InGaN sample grown at 950°C under (a) dark and (b) illuminated condition.

When exposed to light as shown in Fig. 44 (b), a significant reduction in the impedance is evident across the full frequency spectrum, especially at lower frequencies. This decrease in $|Z|$ demonstrates improved charge transport stemming from the production of photocarriers. At the same time, the phase angle is different from the almost perfect capacitive behavior seen in the dark. The minimum phase angle shifts and becomes less capacitive, showing an increased resistance. The phase feature is getting narrower and shifting to higher frequencies, which suggests that the characteristic relaxation time constant ($\tau = RC$) is getting smaller. This is similar to a decrease in charge-transfer resistance and/or a change in space-charge capacitance under illumination. This change in behavior, from mostly capacitive to a mix of capacitive and resistive, shows that the electrochemical activity of the 950 °C Ge-doped InGaN sample is strongly affected by light.

The significant difference between the dark and illuminated responses indicates that, in the absence of light, the interface is dominated by depletion and functions as a blocking capacitor. When exposed to light, photogenerated carriers decrease the depletion width and improve interfacial charge-transfer kinetics. The prevailing transport mechanism undergoes a transition from charge storage (capacitive) to photo-assisted charge transfer. The results indicate the retention of significant photoelectrochemical activity in the sample despite Ge doping at 950 °C. The absence of behavior as a fully metallic or degenerate conductor under dark conditions is also indicated.

Nyquist plot

As shown in Fig. 45, the semicircle obtained at +800 mV is considerably more pronounced than that at 0 V, suggesting an increase in R_{ct} at elevated anodic bias. This implies that interfacial electron transfer is increasingly limited under strong positive polarization. This behavior is different from all the other samples, which showed the opposite trend. The undoped and Ge-doped InGaN samples grown at 850 °C and 1000 °C show improved charge transfer kinetics under anodic bias, as indicated by R_{ct} decreasing at +800 mV compared to 0 V. This behavior aligns with conventional n-type semiconductor behavior, where anodic bias promotes favorable band bending for charge extraction.

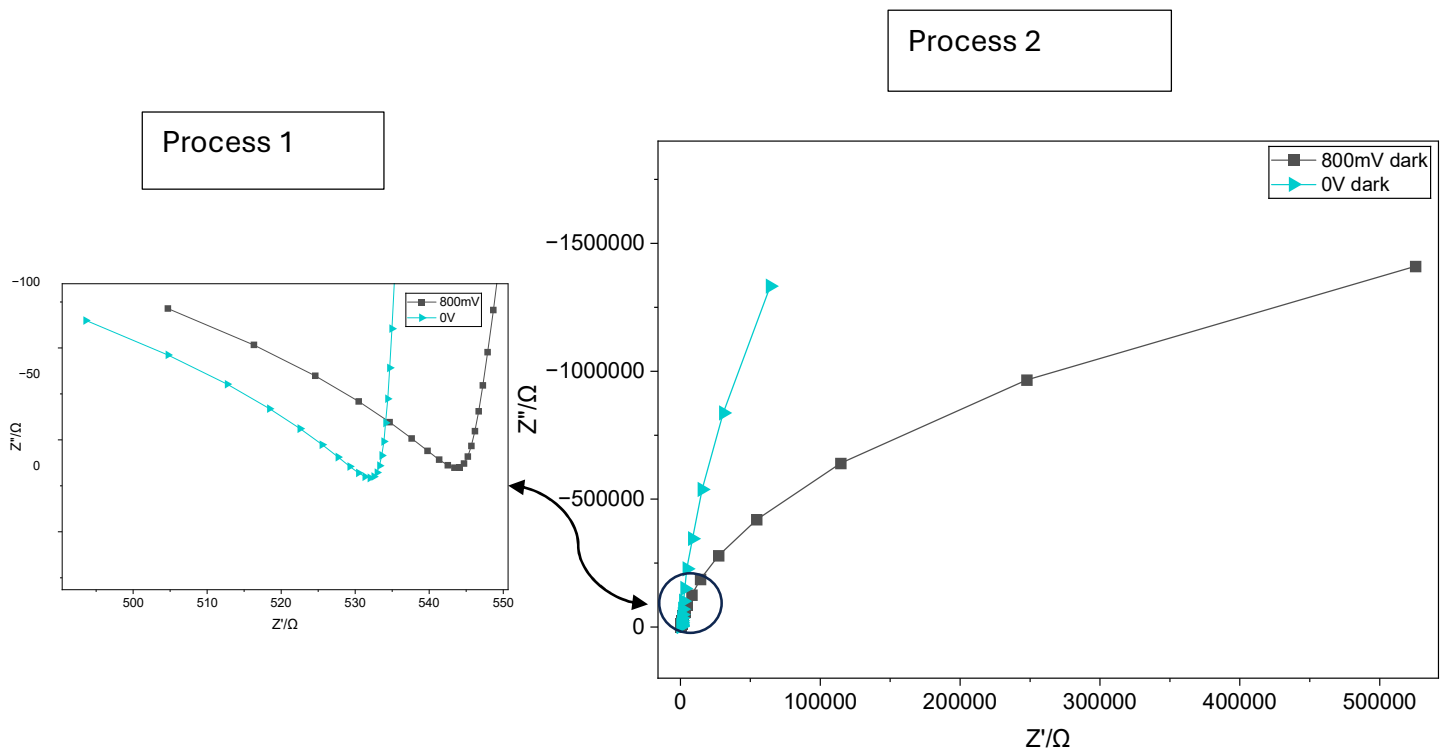


Fig 45: the Nyquist plot of Ge-doped InGaN sample grown at 950 °C measured under dark conditions.

Conversely, the Ge-doped 950 °C sample, though demonstrating a considerably higher donor concentration, exhibits enhanced R_{ct} at +800 mV. The elevated carrier density resulting from heavy Ge addition likely creates a high concentration of defect states and surface traps. These trap states increase surface recombination and induce

increased band bending within the space charge region under strong anodic bias, thereby reducing interfacial charge transfer.⁶³

The Nyquist plots of the Ge-doped InGaN sample grown at 950 °C shown in Fig. 46 under UV illumination exhibit a significant reduction in charge transfer resistance R_{ct} as the anodic bias increases. This behavior is in contrast to the dark measurements, where an increased R_{ct} was demonstrated at higher anodic bias. Under UV illumination, photogenerated carriers dominate the interfacial processes. A stronger electric field within the space charge region at higher potentials promotes efficient charge separation and suppresses recombination. Charge transfer resistance decreases systematically with an increasing bias, confirming typical n-type photoanode characteristics.

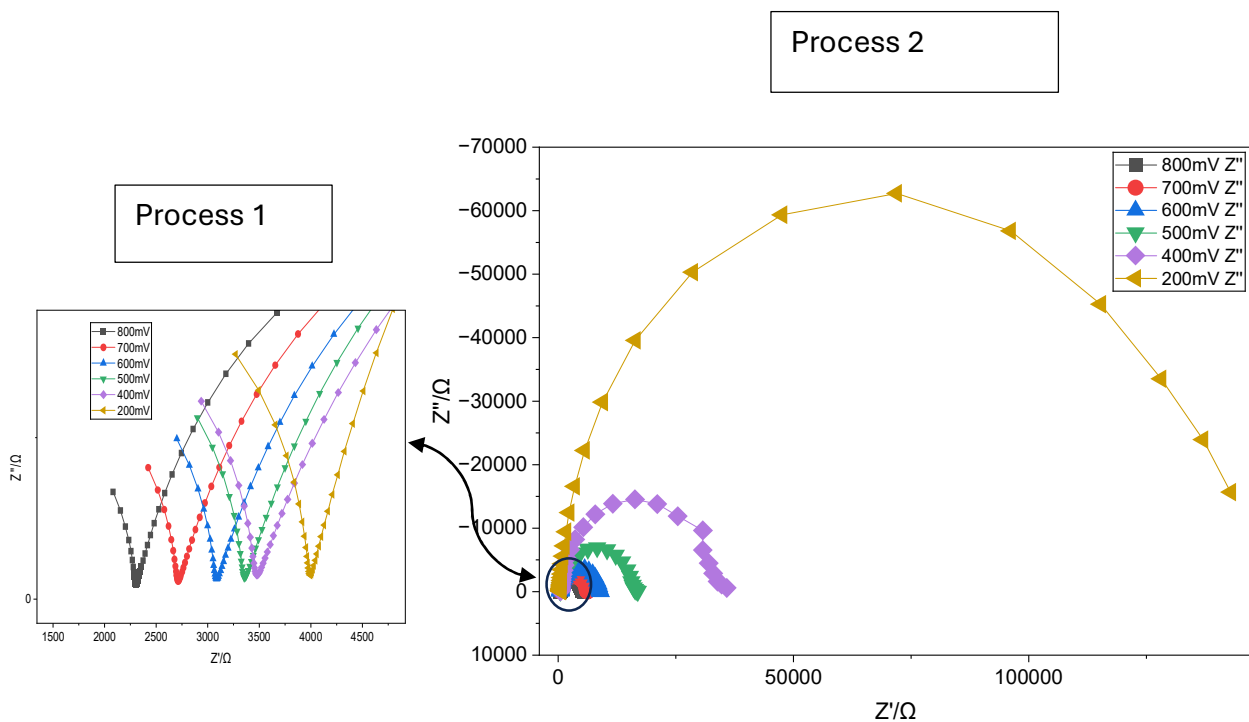


Fig 46: the Nyquist plot of Ge-doped InGaN sample grown at 950 °C measured under illumination.

Mott-Schottky Analysis

The Mott–Schottky plot of the Ge-doped InGaN sample, which was grown at 950 °C, is shown in the Figure 47. The values of capacitance have been extracted by using the constant phase element parameters i.e. Q and α of the equivalent circuit, which was fitted to the data as shown in Table 5. The capacitance measurements were taken under dark conditions.

Voltage vs RHE (V)	Resistance, R_2 (Ω)	CPE constant, $Q_2/(\Omega^{-1})$	α_2	$C_2(F)$ $(Q_2R_2^{(1-\alpha_2)})^{1/\alpha_2}$	$1/C_2^2$
1.647	186115.63681	4.7522E-7	0.977	3.4187E-7	8.55616E12
1.547	188430.08207	4.63743E-7	0.985	3.69014E-7	7.3437E12
1.447	188313.27594	4.74301E-7	0.985	3.83807E-7	6.78852E12
1.347	188598.07903	4.98723E-7	0.984	3.95048E-7	6.40767E12
1.247	186997.60354	5.2737E-7	0.983	4.15331E-7	5.7971E12
1.047	185560.18653	5.75915E-7	0.987	4.79167E-7	4.35537E12
0.847	190209.27258	6.71205E-7	0.987	5.56912E-7	3.22424E12

Table 5 Impedance parameters of Ge doped InGaN grown at 950 °C sample calculated using RelaxIS software.

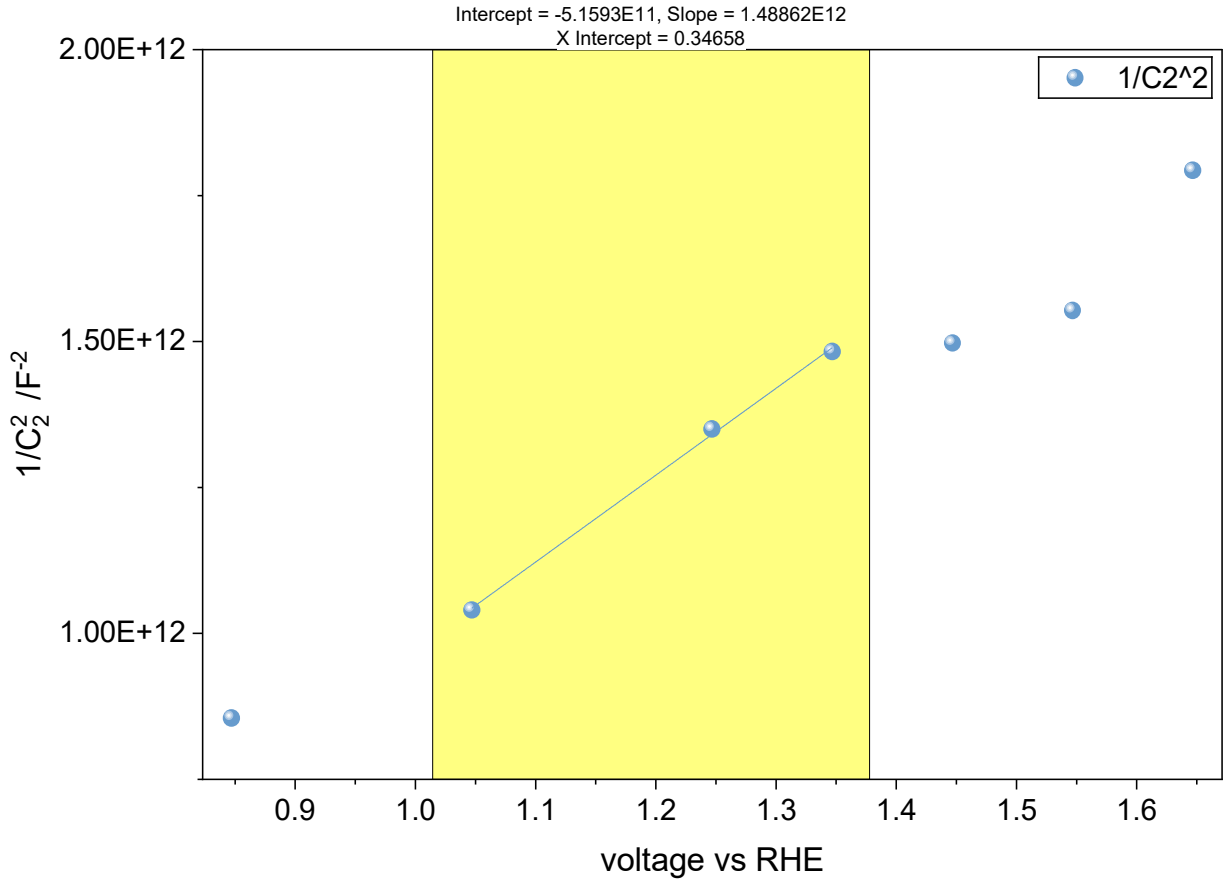


Figure 47: the Mott-Schottky plot of InGaN with doped Ge grown at 950 °C under dark condition.

Figure 47 shows the Mott-Schottky plot of Ge-doped InGaN grown at 950 °C displays an obvious upward trend within the linear fitting area, suggesting n-type semiconductor characteristics. The three data points have been chosen because of its linearity, if chosen the nonlinear points it will artificially pulled the line down and shifting the intercept. The observation of a distinct linear region between a range of approximately 1.2 and 1.4 V vs RHE indicates that the capacitance within this potential range is predominantly influenced by the space-charge region of the semiconductor compared to surface states or interfacial defects. The linearity in the plot suggests reliable estimation of the semiconductor parameters. A comparatively high donor concentration is suggested by the relatively small slope, which is consistent with effective Ge activation at 950 °C. A high donor concentration reduces the depletion width and enhances electrical conductivity which results in the improved photo-assisted charge-transfer behaviour in the Nyquist analysis (Fig. 45).

Flat band Potential

The flat band potential (E_{fb}) was determined from the x-intercept of the linear region of the Mott-Schottky plot that was observed under dark conditions. It yielded a value of 0.346 V vs. RHE.

Donor Density

The donor density for Ge-doped InGa_N grown at 950 °C follows calculated similar to the undoped using the relation:

$$N_D = \frac{2}{e\epsilon_0 mA^2} \quad (41)$$

$$N_D = 1.02 \times 10^{20} \text{ cm}^{-3} \quad (42)$$

Ge doped (In,Ga)N film grown at 1000 °C

The sample grown at 1000 °C shows the phase angle gradually changes from a high resistance at low frequencies to a state of minimum resistance at intermediate frequencies. This change is marked by a drop in the phase angle to values close to -60° as shown in Fig. 48 (a) under dark conditions. The relatively small phase angle at low frequencies indicates that the impedance is primarily dominated by resistive elements of Ge-doped InGa_N of thin films, which can be attributed to bulk resistance and possible contributions from grain boundaries within the Ge-doped InGa_N layer. As the frequency increases, the phase angle drops more and more, showing how capacitive effects like the depletion capacitance of space-charge region dominate at low frequencies. Space charge regions, depletion capacitance, and trap-assisted charge storage becoming more important.

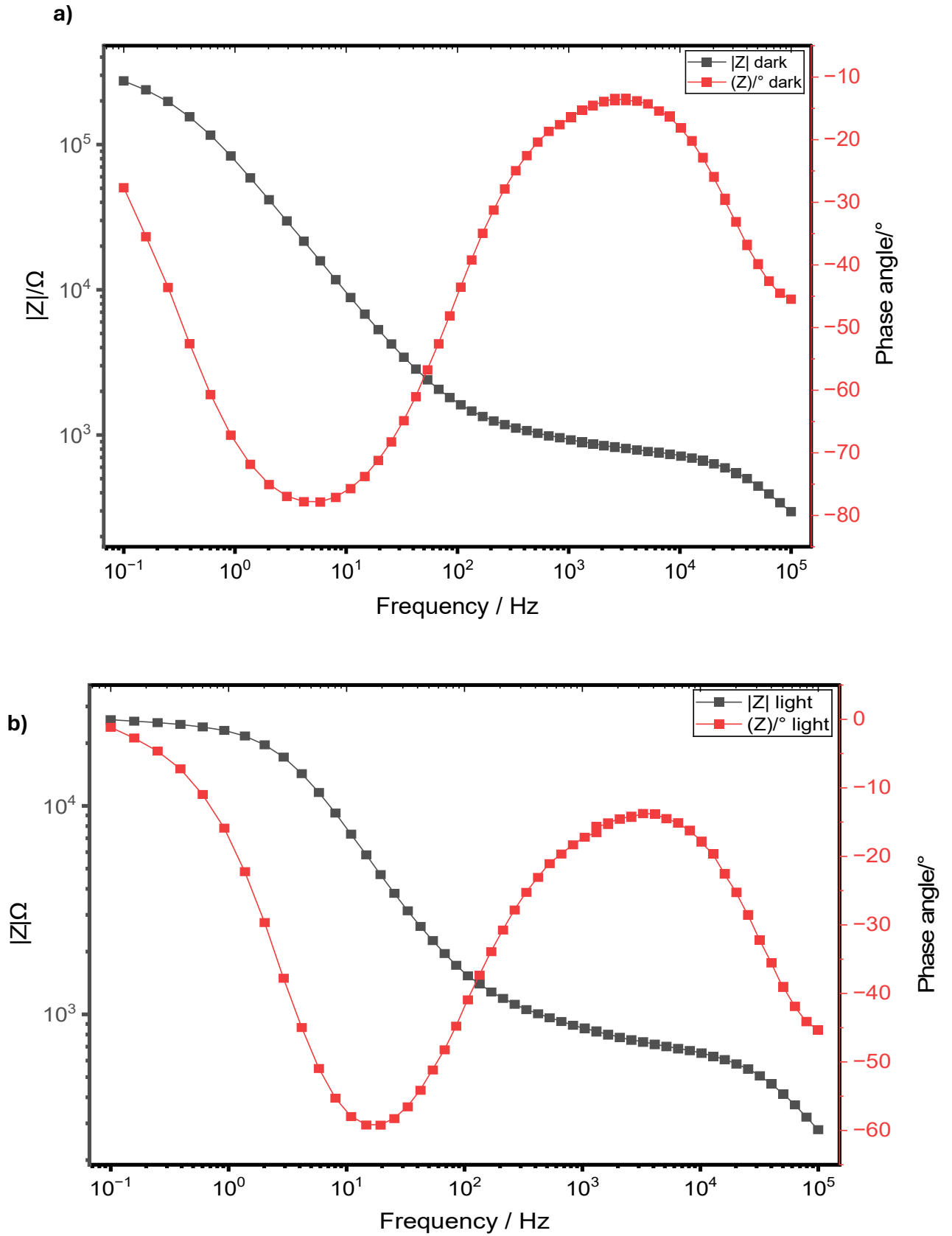


Fig 48: Bode plots of the Ge-doped c-InGaN sample grown at 1000 °C obtained under (a) dark and (b) illuminated conditions at an applied bias of 800 mV.

When exposed to light as shown in Fig 48 (b), a clear change in the impedance response is seen comparable to the other samples. The overall electrical resistance decreases across the whole frequency range, showing better conductivity as of more charge carriers are generated under illumination. The phase angle profile also shifts, with a change in the position of the minimum and a minor decrease in its intensity. The width of the depletion region is reduced by the photogenerated, thereby altering recombination dynamics and charge storage behavior.

Nyquist plot

The Nyquist plot of the impedance of the Ge-doped (In,Ga)N grown at 1000°C is shown in Fig. 49. The observation of a large semicircle under dark conditions indicates high charge transfer resistance and limited carrier transport across the interface. The high impedance values indicate that recombination processes are likely to be the dominant ones, and electrical conductivity is restricted.

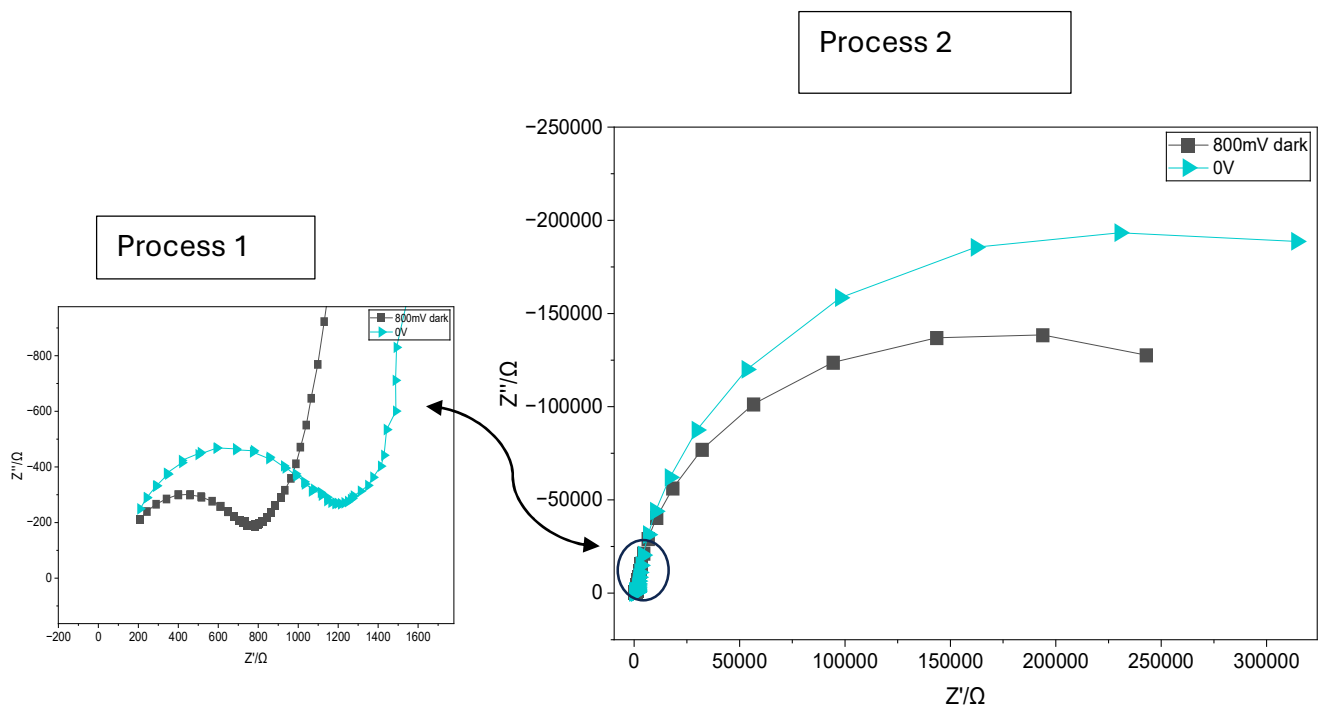


Fig 49: the Nyquist plot of Ge-doped InGaN sample grown at 1000 °C measured under dark conditions.

When exposed to light, substantial alterations in the impedance response become evident in the Nyquist plot as shown in Fig. 50. The semicircle diameter is visibly reduced in comparison to the dark condition, suggesting a significant decrease in charge transfer resistance at the semiconductor electrolyte interface. This decrease is due to the photogeneration of charge carriers when the material is exposed to light which reduce the charge transfer resistance and the width of depletion region. This increases conductivity and makes it easier for charges to move across the interface. As the carrier concentration rises, the likelihood of recombination through trap states is reduced, resulting in faster charge transfer kinetics. Consequently, lower impedance is exhibited by the system under illumination.

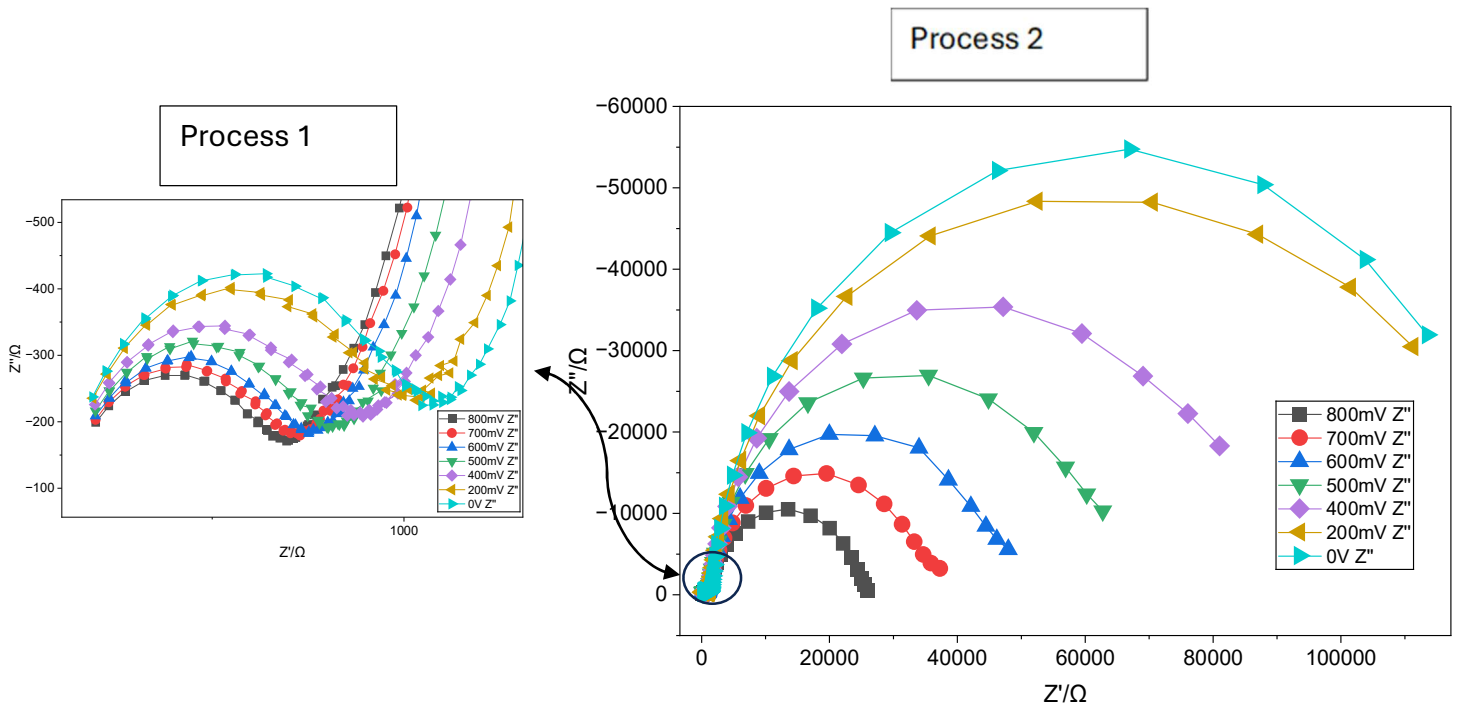


Figure 50: the Nyquist plot of Ge-doped InGaN sample grown at 1000 °C measured under illumination.

Additionally, the decrease in size of semicircles under applied bias (as seen in the various semicircles at different voltages) suggest that the interfacial charge transfer and depletion region properties are highly voltage dependent.

Mott-Schottky Analysis

The Mott–Schottky plot of the Ge-doped InGaN sample, which was grown at 1000 °C, is shown in the Figure 51. The values of capacitance have been extracted by using the constant phase element parameters i.e. Q and α of the equivalent circuit, which was fitted to the data as shown in Table 6. The capacitance measurements were taken under dark conditions.

Voltage vs RHE (V)	Resistance, R_2 (Ω)	CPE constant, $Q_2/(\Omega^{-1})$	α_2	$C_2(F)$ $(Q_2R_2^{(1-\alpha_2)})^{1/\alpha_2}$	$1/C_2^2$
1.647	330938.0684	2.41816E-6	0.90596	6.31636E-7	2.50649E12
1.547	344794.05208	2.29552E-6	0.91208	6.56551E-7	2.31987E12
1.447	370411.57158	2.22473E-6	0.91588	6.73114E-7	2.20711E12
1.347	419911.39968	2.32949E-6	0.91268	6.73505E-7	2.20454E12
1.247	460033.19046	2.11768E-6	0.93558	8.61293E-7	1.34803E12
1.047	423345.93023	2.03312E-6	0.94201	9.07404E-7	1.2145E12
0.847	422945.21203	2.09165E-6	0.95119	1.06918E-6	8.74779E11

Table 6: shows the impedance parameters of Ge doped InGaN grown at 1000 °C sample calculated using RelaxIS software

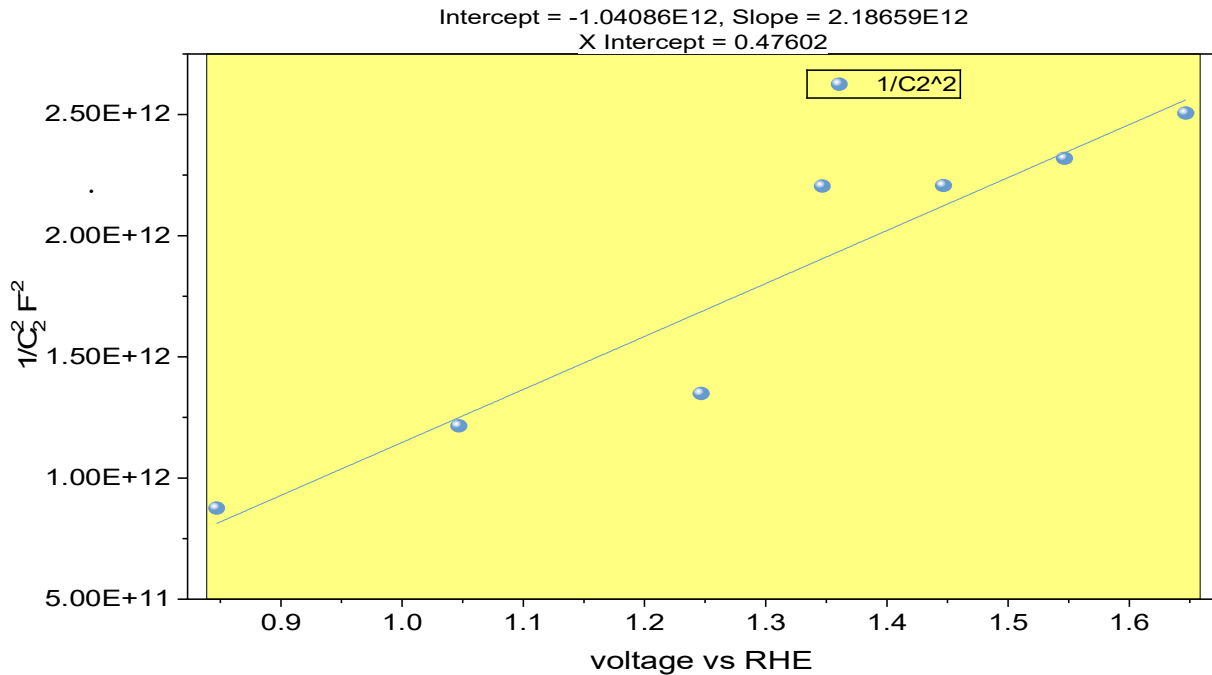


Figure 51: the Mott-Schottky plot of InGaN with doped Ge grown at 1000 °C under dark condition.

The linear relation observed indicates capacitance is primarily influenced by depletion layer capacitance and that the presence of surface states can be neglected

Flat Band Potential

The flat band potential (E_{fb}) was determined from the x-intercept of the linear region of the Mott-Schottky plot that was observed under dark conditions. It yielded a value of 0.47 V vs. RHE

Donor density

The donor density calculated using the relation:

$$N_D = \frac{2}{e\epsilon\epsilon_0 mA^2} \quad (43)$$

$$N_D = 7.7 \times 10^{19} cm^{-3} \approx 10^{20} cm^{-3} \quad (44)$$

3.5.4 Comparative EIS and Mott-Schottky Analysis of Undoped and Ge-doped InGaN

The parameters extracted from the electrochemical characterization are listed in table

Sample (°C)	$N_d (cm^{-3})$	Slope (m)	E_{fb} (V vs RHE)	Dark R_{ct} (800mV)	Light R_{ct} (800mV)
undoped	2.7×10^{19}	5.91×10^{12}	0.35	~190 k Ω	~15 k Ω
850	2.5×10^{19}	2.72×10^{13}	0.48	~60 k Ω	~7 k Ω
950	1.02×10^{20}	1.1×10^{12}	0.34	~500 k Ω	~5k Ω
1000	7.7×10^{19}	2.18×10^{12}	0.47	~ 250 k Ω	~20 k Ω

Table 7: A comparison of the electrochemical and electronic properties under dark and UV illumination conditions of the differently grown (Ga,In)N thin films at different temperatures.

The Nyquist plots obtained under dark conditions at 800mV demonstrate a discernible correlation between charge-transfer resistance (R_{ct}) and the temperature at which Ge is incorporated. The InGaN sample grown at 950 °C exhibited the largest semicircle diameter, showing the opposite trend of increasing impedance with increasing voltage, as previously discussed, suggesting the highest interfacial charge-transfer resistance. This suggests that strong depletion and limited carrier transport occur at the interface

when intentional doping exceeds a certain level. The 850 °C sample exhibits the lowest R_{ct} value under dark conditions. This shows that increasing the incorporation of Ge further increases the impedance compared to the sample without Ge doping.

Thus, the dark R_{ct} trend follows:

950 °C > 1000 °C > undoped > 850 °C.

Moderate Ge incorporation (850 °C) improves conductivity and reduces depletion resistance, but at high growth temperatures (950 °C and 1000 °C) can introduce interfacial disorder, increasing charge-transfer resistance.

The impedance behavior changes significantly under UV illumination at 800mV. The 1000 °C sample displays the largest semicircle diameter when illuminated, suggesting the highest R_{ct} among all the samples when compared under UV illumination. The undoped sample has slightly lower R_{ct} than the 1000 °C sample but higher than the samples grown at 850 °C and 950 °C. The undoped sample has a relatively moderate R_{ct} . The 950 °C sample has the smallest semicircle diameter, though it exhibits the highest impedance under dark conditions.

Therefore, the illuminated R_{ct} trend is as follows:

1000 °C > undoped > 950 °C > 850 °C.

The change in trend compared to dark conditions shows that distinct processes are affected by photoexcitation. The impedance under dark conditions is mostly affected by depletion width and intrinsic conductivity, while the impedance under illumination is influenced by recombination dynamics, trap-assisted processes depending on doping. Doping affects the width of depletion region and, thus, R_{ct} . The high R_{ct} value in the 1000 °C sample under light shows increased recombination, which may be due to a higher number of carriers interacting with defects at the interface.

Mott-Schottky Analysis comparison:

The Mott–Schottky plots of all the samples have positive slopes, which confirms n-type conductivity. The smallest slope is shown by the sample grown at 950 °C, suggesting highest donor density. The sample grown at 850 °C shows a steeper slope compared to the undoped sample, indicating a lower donor density. This suggests that

the dopant incorporation may be incomplete or that compensation effects are present at this growth temperature.

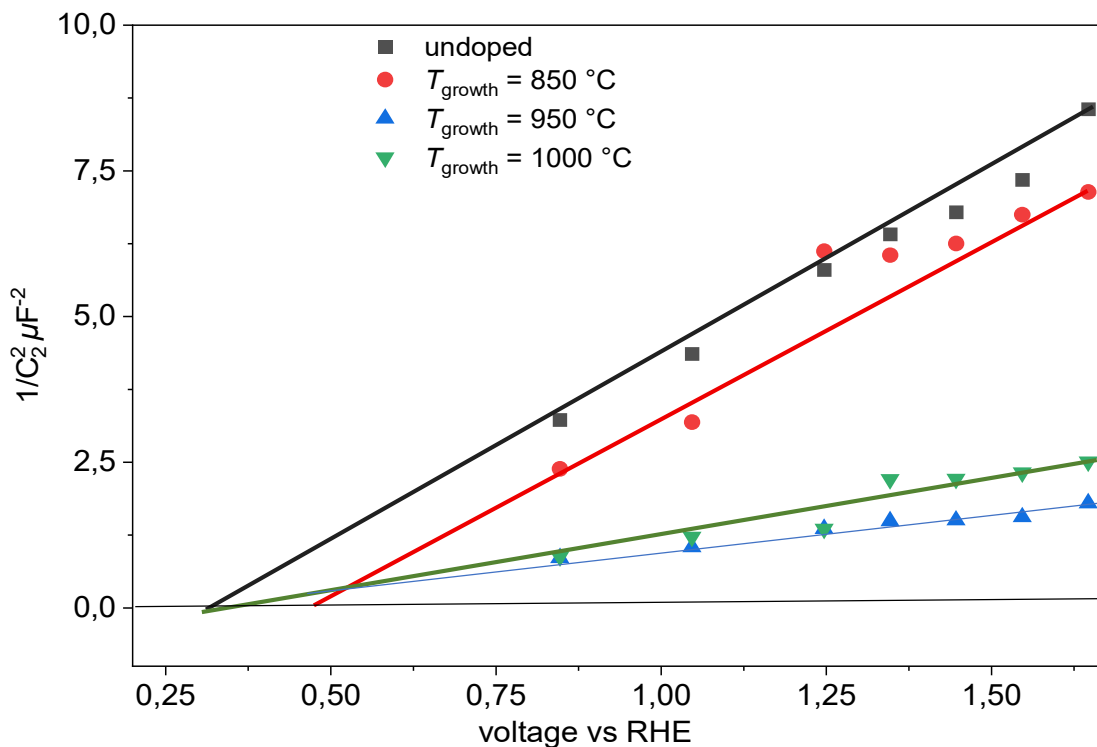


Fig 52: Comparison of Mott-Schottky plots touching intercept points of undoped and Ge doped InGaN grown at 850 °C, 950 °C and 1000 °C.

Mechanistic Interpretation

The results of the electrochemical study show that adding Ge affects both the total amount of carriers and how fast reactions happen at the interface, but not in a simple way. Under dark conditions, there is a reduction in depletion resistance compared to undoped InGaN, with 850 °C showing the most suitable interfacial transport. However, an increase in the growth temperature to 1000 °C partially reduces interfacial efficiency.

The behavior of the impedance is primarily influenced by recombination dynamics when exposed to light. The 950 °C sample, even though it has more donor density and a shifted flat band potential, shows more resistance to recombination, which leads to the highest R_{ct} under light. On the other hand, the 850 °C sample displays the lowest resistance in both dark and illuminated conditions, suggesting that the interfacial charge transfer is relatively stable. The results indicate that the electrochemical response of Ge-doped InGaN is determined by a

competition between electrical activation, defect formation, and photo-induced carrier recombination.

Conclusion

The photoelectrochemical characterization of (In,Ga)N with different doping concentration of Ge has been performed. The impact of Ge doping temperature on the structural and electrochemical properties of InGaN was the focus of this investigation, with a key focus on understanding charge-transfer dynamics at the semiconductor-electrolyte interface with and without illumination. Using a combination of electrochemical impedance spectroscopy (EIS) and Mott–Schottky analysis under dark and UV illumination conditions, we evaluated the relationship between growth temperature, Ge doping, and interfacial kinetics.

Mott–Schottky analysis verified n-type conductivity for all substrates. The donor density displayed a non-monotonic relationship with growth temperature. The sample grown at 950 °C had the highest donor density. On the other hand, the 850 °C sample exhibited a reduced donor density compared to those of the undoped sample, indicating inadequate dopant incorporation or potential compensation mechanisms. The electrical behavior at 1000 °C showed a deviation from the optimal trend seen at 950 °C probably due to inhomogeneous In concentration.

Electrochemical impedance spectroscopy allowed the evaluation of the charge-transfer resistance under dark and illuminated conditions. Under dark conditions, the sample grown at 950 °C and 1000 °C exhibited the highest charge transfer resistance at 800 mV, whereas the sample grown at 850 °C exhibited reduced charge transfer resistance revealing enhanced conductivity among all the samples. However, increasing the growth temperature to 950 °C or 1000 °C resulted in a higher charge transfer resistance than the undoped (Ga,In)N sample at 800 mV, suggesting the initiation of trap-assisted and defects recombination mechanisms.

The impedance response exhibited an inverse trend under UV illumination. The sample grown at 1000 °C demonstrated the highest charge-transfer resistance at 800mV (approximately 20 k Ω) compared to other samples, even though it had the highest donor density. This shows that heightened resistance in both circumstances dark and in light, validating that the high growth temperature produces inhomogeneities in the In content properties.

Overall, it has been demonstrated by the obtained results that optimal electrochemical performance is not necessarily yielded by maximizing donor density. On the other hand, an ideal equilibrium between carrier concentration, defect density, and interfacial quality dictates

charge-transfer effectiveness. The most stable and lowest charge-transfer resistance was observed to be produced by moderate Ge incorporation at 850 °C, whereas 950 °C was found to maximize donor activation but exhibit recombination-dominated behavior under illumination. The 1000 °C sample experienced deterioration at the interface probably due to inhomogeneous In content in the thin films.

In conclusion, the electronic and electrochemical properties of InGaN are tuned by the growth temperature of the thin films. The study emphasizes that achieving enhanced interfacial charge-transfer characteristics requires more precise doping than relying on reaching maximum doping concentrations. These results offer valuable perspective for enhancing the photoelectrochemical properties of Ge-doped InGaN for applications in photoelectrochemical and optoelectronic devices.

Future Perspective

The presented study on MBE-grown Ge-doped InGaN photoelectrodes also indicates some crucial points to be further investigated to optimize the material for photoelectrochemical water splitting applications.

An important area for future research is the systematic optimization of germanium (Ge) doping concentration. Although doping increases carrier density and improves electrical conductivity, incorporating too much of the dopant can introduce structural defects and create additional recombination sites, which can negatively impact charge transfer kinetics. A controlled study that correlates donor density, as determined by Mott–Schottky analysis, with charge transfer resistance, as determined by impedance spectroscopy, would enable the identification of an optimal doping regime that optimizes conductivity and minimizes interfacial kinetics. This optimization is crucial for maximizing band bending and facilitating efficient charge separation at the semiconductor-electrolyte interface.

Furthermore, the impedance analysis suggests that interfacial processes substantially impact the low-frequency response, indicating that surface states are crucial for achieving optimal performance. Therefore, future investigations should aim to reduce trap-assisted recombination through surface engineering strategies. The introduction of ultrathin protective layers or surface passivation treatments may help reduce defect-mediated charge trapping while ensuring efficient carrier transport. Additional methods that study surfaces can help us better understand the chemical and electronic structure of the interface and identify the origin of the observed limitations.

Finally, stability is a critical requirement for practical photoelectrochemical applications; extended tests under continuous illumination, along with characterization, will identify degradation pathways. Ensuring reliable operating conditions is vital for shifting InGaN-based photoelectrodes from basic research to practical hydrogen production technologies. In general, the results of this study provide a significant foundation for the effective design and improvement of InGaN photoelectrodes. Continued efforts in the following areas are needed to improve charge separation efficiency and interfacial reaction kinetics: doping control, surface modification, catalytic integration, and stability assessment. These efforts will advance the sustainable development of efficient and reliable systems for solar-driven hydrogen production.

References

1. *Statistical Review of World Energy 2025 | 74 Th Edition In Collaboration With.* www.energyinst.org/statistical-review.
2. Clarizia, L., Nadagouda, M. N. & Dionysiou, D. D. Recent advances and challenges of photoelectrochemical cells for hydrogen production. *Current Opinion in Green and Sustainable Chemistry* vol. 41 Preprint at <https://doi.org/10.1016/j.cogsc.2023.100825> (2023).
3. Singh, S. *et al.* Hydrogen: A sustainable fuel for future of the transport sector. *Renewable and Sustainable Energy Reviews* **51**, 623–633 (2015).
4. ObnovitelneZdrojeEnergie_Aj.
5. Shahazi, R. *et al.* Advancements in water splitting for sustainable energy generation: A review. *Characterization and Application of Nanomaterials* vol. 7 Preprint at <https://doi.org/10.24294/can.v7i1.5834> (2024).
6. Sobrino, F. H., Monroy, C. R. & Pérez, J. L. H. Critical analysis on hydrogen as an alternative to fossil fuels and biofuels for vehicles in Europe. *Renewable and Sustainable Energy Reviews* **14**, 772–780 (2010).
7. Nishioka, S., Osterloh, F. E., Wang, X., Mallouk, T. E. & Maeda, K. Photocatalytic water splitting. *Nature Reviews Methods Primers* **3**, (2023).
8. Ikram, A., Zulfeqar, M. & Satsangi, V. R. Role and prospects of green quantum dots in photoelectrochemical hydrogen generation: A review. *International Journal of Hydrogen Energy* vol. 47 11472–11491 Preprint at <https://doi.org/10.1016/j.ijhydene.2022.01.187> (2022).
9. Philipps, J. M. *et al.* Photoelectrochemical response of GaN, InGaN, and GaNP nanowire ensembles. *J. Appl. Phys.* **123**, (2018).
10. Takanabe, K. Photocatalytic Water Splitting: Quantitative Approaches toward Photocatalyst by Design. *ACS Catal.* **7**, 8006–8022 (2017).
11. Alley, O. J. *et al.* Best Practices in PEC Water Splitting: How to Reliably Measure Solar-to-Hydrogen Efficiency of Photoelectrodes. *Front. Energy Res.* **10**, (2022).

12. Shi, X., Cai, L., Ma, M., Zheng, X. & Park, J. H. General Characterization Methods for Photoelectrochemical Cells for Solar Water Splitting. *ChemSusChem* vol. 8 3192–3203 Preprint at <https://doi.org/10.1002/cssc.201500075> (2015).
13. Xiao, Y. *et al.* Interface engineering for photoelectrochemical oxygen evolution reaction. *Chemical Society Reviews* vol. 54 1268–1317 Preprint at <https://doi.org/10.1039/d4cs00309h> (2024).
14. Singh, Jai. *Optical Properties of Materials and Their Applications*. (John Wiley & Sons, 2020).
15. Griffiths, I. *et al.* Distinguishing cubic and hexagonal phases within InGaN/GaN microstructures using electron energy loss spectroscopy. *J. Microsc.* **262**, 167–170 (2016).
16. Marschall, R. Semiconductor composites: Strategies for enhancing charge carrier separation to improve photocatalytic activity. *Adv. Funct. Mater.* **24**, 2421–2440 (2014).
17. Yoshida, S. Growth of cubic III-nitride semiconductors for electronics and optoelectronics application. *Physica E Low. Dimens. Syst. Nanostruct.* **7**, 907–914 (2000).
18. Nam, K. M. *et al.* New crystal structure: Synthesis and characterization of hexagonal wurtzite MnO. *J. Am. Chem. Soc.* **134**, 8392–8395 (2012).
19. Philipps, J. M. *et al.* Photoelectrochemical response of GaN, InGaN, and GaNP nanowire ensembles. *J. Appl. Phys.* **123**, (2018).
20. As, D. J. Cubic group-III nitride-based nanostructures-basics and applications in optoelectronics. *Microelectronics J.* **40**, 204–209 (2009).
21. Zhou, C. *et al.* Review—The Current and Emerging Applications of the III-Nitrides. *ECS Journal of Solid State Science and Technology* **6**, Q149–Q156 (2017).
22. *Electrochemical Impedance Spectroscopy and Its Applications*.
23. Lazanas, A. C. & Prodromidis, M. I. Electrochemical Impedance Spectroscopy—A Tutorial. *ACS Measurement Science Au* vol. 3 162–193 Preprint at <https://doi.org/10.1021/acsmeasuresciau.2c00070> (2023).
24. Cano, E., Lafuente, D. & Bastidas, D. M. Use of EIS for the evaluation of the protective properties of coatings for metallic cultural heritage: A review. *Journal of Solid State*

- Electrochemistry* vol. 14 381–391 Preprint at <https://doi.org/10.1007/s10008-009-0902-6> (2010).
25. Mhaskar, C. M., Roy Chaudhuri, S. & Roy Chaudhuri, A. Chloride Ion Vacancy-Mediated Multilevel Bipolar Resistive Switching in Lead-Free All-Inorganic Halide Perovskite Thin Films. *ACS Appl. Mater. Interfaces* **17**, 55054–55064 (2025).
 26. Boukamp, B. A. *A NONLINEAR LEAST SQUARES FIT PROCEDURE FOR ANALYSIS OF IMMITTANCE DATA OF ELECTROCHEMICAL SYSTEMS*.
 27. Zhang, L., Peng, H., Ning, Z., Mu, Z. & Sun, C. Comparative research on RC equivalent circuit models for lithium-ion batteries of electric vehicles. *Applied Sciences (Switzerland)* **7**, (2017).
 28. Magar, H. S., Hassan, R. Y. A. & Mulchandani, A. Electrochemical impedance spectroscopy (Eis): Principles, construction, and biosensing applications. *Sensors* vol. 21 Preprint at <https://doi.org/10.3390/s21196578> (2021).
 29. Huang, J., Li, Z., Liaw, B. Y. & Zhang, J. Graphical analysis of electrochemical impedance spectroscopy data in Bode and Nyquist representations. *J. Power Sources* **309**, 82–98 (2016).
 30. Chen, S. *2-Practical Electrochemical Cells*. (2007).
 31. *Potential and Current Distribution in Electrochemical Cells: Interpretation of the Half-Cell Voltage Measurements as a Function of Reference-Electrode Location*.
 32. Klahr, B., Gimenez, S., Fabregat-Santiago, F., Bisquert, J. & Hamann, T. W. Photoelectrochemical and impedance spectroscopic investigation of water oxidation with ‘co-Pi’-coated hematite electrodes. *J. Am. Chem. Soc.* **134**, 16693–16700 (2012).
 33. Bisquert, J. Theory of the impedance of electron diffusion and recombination in a thin layer. *Journal of Physical Chemistry B* **106**, 325–333 (2002).
 34. Díez-García, M. I. & Gómez, R. Investigating Water Splitting with CaFe₂O₄ Photocathodes by Electrochemical Impedance Spectroscopy. *ACS Appl. Mater. Interfaces* **8**, 21387–21397 (2016).
 35. Georgakilas, V., Perman, J. A., Tucek, J. & Zboril, R. Broad Family of Carbon Nanoallotropes: Classification, Chemistry, and Applications of Fullerenes, Carbon Dots,

- Nanotubes, Graphene, Nanodiamonds, and Combined Superstructures. *Chemical Reviews* vol. 115 4744–4822 Preprint at <https://doi.org/10.1021/cr500304f> (2015).
36. Sluyters-Rehbach, M. *INTERNATIONAL UNION OF PURE AND APPLIED CHEMISTRY PHYSICAL CHEMISTRY DIVISION COMMISSION ON ELECTROCHEMISTRY* IMPEDANCES OF ELECTROCHEMICAL SYSTEMS: TERMINOLOGY, NOMENCLATURE AND REPRESENTATION PART I: CELLS WITH METAL ELECTRODES AND LIQUID SOLUTIONS (IUPAC Recommendations 1994) Prepared for Publication By. Pure & Appl. Chem* vol. 66 (1994).
 37. *Electrochemical Impedance Spectroscopy and Its Applications*.
 38. Bondarenko, A. S. & Ragoisha, G. A. Variable Mott-Schottky plots acquisition by potentiodynamic electrochemical impedance spectroscopy. *Journal of Solid State Electrochemistry* **9**, 845–849 (2005).
 39. Lockyer, N. P. *et al.* Secondary ion mass spectrometry. *Nature Reviews Methods Primers* **4**, (2024).
 40. Hoppe, P. *et al.* Nanosims studies of small presolar SiC grains: New insights into supernova nucleosynthesis, chemistry, and dust formation. *Astrophysical Journal* **719**, 1370–1384 (2010).
 41. Belu, A. M., Graham, D. J. & Castner, D. G. Time-of-flight secondary ion mass spectrometry: Techniques and applications for the characterization of biomaterial surfaces. *Biomaterials* vol. 24 3635–3653 Preprint at [https://doi.org/10.1016/S0142-9612\(03\)00159-5](https://doi.org/10.1016/S0142-9612(03)00159-5) (2003).
 42. Mayer, M. T. Photovoltage at semiconductor–electrolyte junctions. *Current Opinion in Electrochemistry* vol. 2 104–110 Preprint at <https://doi.org/10.1016/j.coelec.2017.03.006> (2017).
 43. Dotan, H. *et al.* Decoupled hydrogen and oxygen evolution by a two-step electrochemical–chemical cycle for efficient overall water splitting. *Nat. Energy* **4**, 786–795 (2019).
 44. Klahr, B., Gimenez, S., Fabregat-Santiago, F., Hamann, T. & Bisquert, J. Water oxidation at hematite photoelectrodes: The role of surface states. *J. Am. Chem. Soc.* **134**, 4294–4302 (2012).

45. Hisatomi, T. *et al.* La₅Ti₂Cu_{1-x}Ag_xS₅O₇ photocathodes operating at positive potentials during photoelectrochemical hydrogen evolution under irradiation of up to 710 nm. *Energy Environ. Sci.* **8**, 3354–3362 (2015).
46. Sandford, C. *et al.* A synthetic chemist's guide to electroanalytical tools for studying reaction mechanisms. *Chem. Sci.* **10**, 6404–6422 (2019).
47. Bard, A. J. . & Faulkner, L. R. . *Electrochemical Methods : Fundamentals and Applications*. (John Wiley & Sons, Inc., 2001).
48. Ahnood, A., Chambers, A., Gelmi, A., Yong, K. T. & Kavehei, O. Semiconducting electrodes for neural interfacing: a review. *Chemical Society Reviews* vol. 52 1491–1518 Preprint at <https://doi.org/10.1039/d2cs00830k> (2023).
49. Yang, W., Prabhakar, R. R., Tan, J., Tilley, S. D. & Moon, J. Strategies for enhancing the photocurrent, photovoltage, and stability of photoelectrodes for photoelectrochemical water splitting. *Chemical Society Reviews* vol. 48 4979–5015 Preprint at <https://doi.org/10.1039/c8cs00997j> (2019).
50. Iandolo, B., Wickman, B., Zorić, I. & Hellman, A. The rise of hematite: origin and strategies to reduce the high onset potential for the oxygen evolution reaction. *J. Mater. Chem. A Mater.* **3**, 16896–16912 (2015).
51. Iqbal, A., Yuan, S., Wang, Z. & Bevan, K. H. Impact of Bulk Trapping Phenomena on the Maximum Attainable Photovoltage of Semiconductor-Liquid Interfaces. *Journal of Physical Chemistry C* **122**, 23878–23889 (2018).
52. Morlock, S., Subramanian, S. K., Zouni, A. & Lisdat, F. Closing the green gap of photosystem I with synthetic fluorophores for enhanced photocurrent generation in photobiocathodes. *Chem. Sci.* **14**, 1696–1708 (2023).
53. Hitchcock, A. P. Analysis of X-ray images and spectra (aXis2000): A toolkit for the analysis of X-ray spectromicroscopy data. *J. Electron Spectros. Relat. Phenomena* **266**, 147360 (2023).
54. Zhou, W., Apkarian, R. P., Lin Wang, Z. & Joy, D. *Fundamentals of Scanning Electron Microscopy*.
55. Newbury, D. E. & Ritchie, N. W. M. Performing elemental microanalysis with high accuracy and high precision by scanning electron microscopy/silicon drift detector energy-dispersive

- X-ray spectrometry (SEM/SDD-EDS). *Journal of Materials Science* vol. 50 493–518 Preprint at <https://doi.org/10.1007/s10853-014-8685-2> (2014).
56. Takanabe, K. Photocatalytic Water Splitting: Quantitative Approaches toward Photocatalyst by Design. *ACS Catal.* **7**, 8006–8022 (2017).
 57. Tilley, S. D. Recent Advances and Emerging Trends in Photo-Electrochemical Solar Energy Conversion. *Advanced Energy Materials* vol. 9 Preprint at <https://doi.org/10.1002/aenm.201802877> (2019).
 58. Arthur, J. R. *Molecular Beam Epitaxy*. www.elsevier.com/locate/susc.
 59. Cho, A. Y. *Advances in Molecular Beam Epitaxy (MBE)*. *Journal of Crystal Growth* vol. 111 (1991).
 60. Ding, C., Shi, J., Wang, Z. & Li, C. Photoelectrocatalytic Water Splitting: Significance of Cocatalysts, Electrolyte, and Interfaces. *ACS Catal.* **7**, 675–688 (2017).
 61. Pajkossy, T. & Jurczakowski, R. Electrochemical impedance spectroscopy in interfacial studies. *Current Opinion in Electrochemistry* vol. 1 53–58 Preprint at <https://doi.org/10.1016/j.coelec.2017.01.006> (2017).
 62. Adachi, M. *et al.* Comparison of electrochemical impedance spectroscopy between illumination and dark conditions. *Chem. Lett.* **40**, 890–892 (2011).
 63. Uergen Ahn, J. H., Homas Dison, T. E., Homas E Dgar, T. F. & Edgar, ----Thomas F. *A NOTE ON STABILITY ANALYSIS USING BODE PLOTS*. (2001).
 64. Vines, L., Monakhov, E. & Kuznetsov, A. Defects in semiconductors. *Journal of Applied Physics* vol. 132 Preprint at <https://doi.org/10.1063/5.0127714> (2022).
 65. Adán-Más, A., Silva, T. M., Guerlou-Demourgues, L. & Montemor, M. F. Application of the Mott-Schottky model to select potentials for EIS studies on electrodes for electrochemical charge storage. *Electrochim. Acta* **289**, 47–55 (2018).